Application of Computer-based Methods to Analyze NAD$^+$-dependent Enzymes

Dissertation

zur Erlangung des
Doktorgrades der Naturwissenschaften (Dr. rer. nat.)

der

Naturwissenschaftlichen Fakultät I - Biowissenschaften -

der Martin-Luther-Universität
Halle-Wittenberg,

vorgelegt

von Herrn Michael Scharfe

geb. am 10.08.1981 in Halle (Saale)

Dipl.-Bioinform. Michael Scharfe
Abteilung Medizinische Chemie
Bereich Pharmazeutische Chemie und Klinische Pharmazie
Insititut für Pharmazie
Martin-Luther-Universität Halle-Wittenberg

Dissertation,
der Naturwissenschaftlichen Fakultät I
der Martin-Luther-Universität Halle-Wittenberg
vorgelegt am 23.04.2015,
verteidigt am 27.07.2015.

1. Gutachter: Prof. Dr. Wolfgang Sippl
2. Gutachter: Prof. Dr. Ivo Große
3. Gutachter: Prof. Dr. Gerhard Wolber

Abstract

During the last decade, a growing number of regulatory processes were linked to the activity NAD^+ dependent transferases, including gene transcription, DNA repair, energy metabolism and bacterial pathogenesis. A variety of NAD^+ consuming enzymes have been suggested as attractive drug targets for human diseases, e.g. caused by bacterial infections or metabolic disorders. Despite intensive research in the field of poly-ADP-ribose polymerases and Sirtuins, there are still substantial gaps in our knowledge regarding other members of NAD^+ dependent transferases. Three less characterized enzymes, namely CDT, Sirt4 and Sirt5, were computationally analyzed in this work, in order to gain further insights into their structural properties and to predict small-molecule inhibitors of their enzymatic activity.

The conformational space of CDT and Sirt5 was analyzed by means of enhanced sampling techniques and a significant flexibility was observed for critical components forming the NAD^+ and substrate binding sites. Representative conformation were extracted from the simulation trajectories and incorporated into the design process of protein-ligand binding models. Conserved and likely important waters were found by crystal structure comparison and confirmed by applying the three-dimensional reference interaction site model theory. Knowledge and models gained from these computationally studies were incorporated into several structure-based virtual screening campaigns, which lead to the identification of 11 novel inhibitors of CDT and more than 10 compounds which were able to inhibit Sirt5 activity in in-vitro assays.

Due to a lack of a Sirt4 crystal structures, a homology model was developed for this enzyme and putative substrates were suggested by means of docking methods. In order to proceed with the biochemical characterization of this novel target protein, a large-scale virtual screening was carried out and a number of diverse compounds was predicted as putative Sirt4 inhibitors.

Kurzfassung

NAD$^+$-abhängige Transferasen sind an einer Vielzahl regulatorischer Prozesse, wie zum Beispiel Genregulation, DNA Reparatur und Energiestoffwechsel, beteiligt. Einige bakterielle Transferasen besitzen pathogene Eigenschaften, indem sie strukturelle und funktionell bedeutsame Proteine des Wirtsorganismus angreifen. NAD$^+$-abhängige Enzyme sind therapeutisch relevant und stellen interessante Targets für die Wirkstoffforschung dar.

Forschungsschwerpunkte lagen in den letzten Jahren bei Poly-ADP-ribose Polymerasen sowie Sirtuinen, wohingegen andere Vertreter dieser Proteinfamilie noch weitestgehend unerforscht sind. Die hier vorliegende Arbeit beschäftigt sich mit drei ausgewählten NAD$^+$-abhängigen Transferasen, welche aus struktureller und biochemischer Sicht noch nicht ausreichend charakterisiert sind. Das bakterielle Toxin CDT, sowie die humanen Sirtuine Sirt4 und Sirt5 wurden mittels computergestützter Methoden genauer untersucht, um Modelle bezüglich struktureller Eigenschaften sowie Protein-Ligand Wechselwirkungen abzuleiten.

Mögliche Konformationen von CDT und Sirt5 wurden mittels Molekül-dynamik-Simulationen näher untersucht, wobei eine signifikante strukturelle Variabilität innerhalb der NAD$^+$- und Substratbindungstaschen festgestellt wurde. Weiterhin wurden konservierte Wassermoleküle, welche bedeutsam für die Proteinstuktur und Protein-Ligand-Wechselwirkungen sind, anhand von Stukturvergleichen und Anwendung aktueller, theoretischer Ansätze gefunden. Die gewonnenen Erkenntnisse und Modelle waren hilfreich, um konsistente Bindungshypothesen aufzustellen und wurden in verschiedenen virtuellen Screenings berücksichtigt. Im Rahmen der durchgeführten computergestützten Experimente wurden verschiedene neuartige Hemmstoffe vorgeschlagen, wobei für 11 Verbindungen eine Hemmung von CDT, sowie für mehr als 10 Verbindung eine Hemmung von Sirt5 anhand anschließender in-vitro Tests gezeigt werden konnte.

Da für Sirt4 zum Zeitpunkt der Arbeit keine Kristallstruktur existierte, wurde ein Homologiemodell ausgehend von verwandten Proteinstrukturen entwickelt. Mögliche Substrate wurden mittels molekularem Docking hinsichtlich Kompatibilität überprüft und eine Reihe diverser Verbindungen wurde durch strukturbasiertes virtuellen Screening als Hemmstoffe vorgeschlagen.

Contents

CHAPTER 1

Introduction

1.1 Posttranslational Modifications of Proteins

A posttranslational modification (PTM) denominates a covalent addition of a certain chemical group to a protein amino acid residue. Such a modification changes the chemical environment of the affected residue, which can have a direct or indirect influence on the protein function[1]. The addition and removal of PTMs is dynamically regulated by competing enzymes and provides a fundamental way how cells regulate processes such as gene transcription and protein activity. Several hundreds posttranslational modifications are known, including acylation, glycosylation, methylation and phosphorylation[2]. This work focusses on two specific PTMs, namely ADP-ribosylation and protein lysine acylation.

1.1.1 ADP-ribosylation

ADP-ribosylation is the reversible addition of one or more ADP-ribose (ADPR) moieties to a target protein residue (see Figure 1.1). Donor of ADPR is usually nicotinamide adenine dinucleotide (NAD^+) and acceptors are nucleophilic groups such as the side chains of lysine, cysteine, asparagine, arginine and glutamate. ADPR itself can also serve as an acceptor for further ribosylation steps leading to poly-ADP-ribosylation reactions[3].
Both reactions cause notable structural as well as chemical changes at the affected ADP-ribosylation sites. Already a mono ADP-ribosylation leads to a remarkable increase in the size of the affected amino acid and introduces two additional negative charges, which can lead to activation or inactivation of the target protein activity. ADP-ribosylation was found to be involved in a wide range of biochemical processes including DNA repair, transcriptional regulation, energy metabolism, cell differentiation and apoptosis[4].
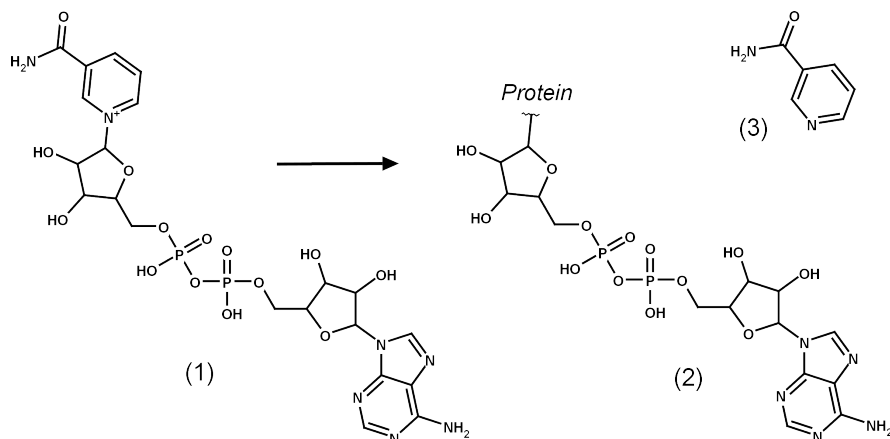
Figure 1.1: General reaction scheme of mono-ADP-ribosylation. NAD$^+$ (1) serves as donor for an ADPR moiety (2) that is covalently linked to a nucleophilic amino acid residue of a target protein. Nicotinamide (3) is released as a by-product of the catalytic reaction.

1.1.2 Protein Lysine Acylation

Due to the positive charged side chain, lysine residues are potent targets for a number of PTMs including the addition of e.g. acetyl, succinyl or methyl groups. Such modifications change the charge distribution on this residue which can have significant structural and functional effects on the related protein[3]. This work focusses on four types of lysine acylation in particular acetylation, malonylation, succinylation and glutarylation (see Figure 1.2).
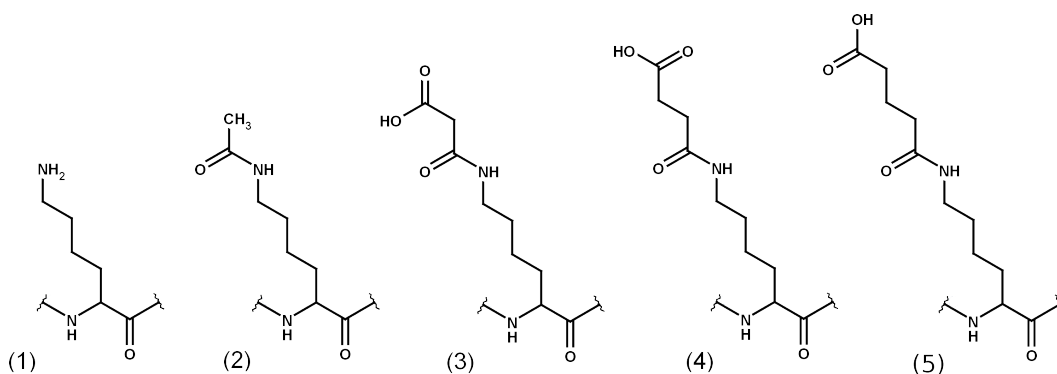
Figure 1.2: Examples of posttranslational modifications of lysine (1) residues: Acetylation (2); Malonylation (3); Succinylation (4); Glutarylation (5).

1.1.2.1 Protein Lysine Acetylation

Acetylations of protein lysine residues appear in nearly all organisms ranging from bacteria to eukaryotes[5]. The addition of acetyl groups can be regulated through

nonenzymatic ways or by certain enzymes called lysine acetyltransferases (KAT)[6]. In opposite, lysine deacetylases (KDAC) are a class of enzymes that remove the acetyl group from a modified lysine and transfer it to a specific acceptor molecule.

Dynamic acetylation and deacetylation serves as a general regulatory mechanism for a wide range of proteins including histones and metabolic enzymes[7]. For example, the function of many enzymes involved in metabolic pathways such as glycolysis, tricarboxylic acid and urea cycle were found to be connected to their acetylation state[8].

1.1.2.2 Protein Lysine Malonylation, Succinylation and Glutarylation

Recent studies uncovered malonylation, succinylation and glutarylation as further modifications of the lysine side chain[9,10]. They are evolutionary conserved and occur in diverse cellular pathways, but protein targets were found to be enriched in metabolic pathways[11,12]. Distinct from acetylation, these three acidic PTMs introduce a negative charge on the positively charged ε-amino group of lysine (see Figure 1.2). Their addition seems to be regulated on nonenzymatic ways, but their removal is catalyzed by certain KDACs of the Sirtuin family.

1.1.3 Nonenzymatic Acylation

Proteins can be acylated through nonenzymatic ways as a consequence of high acyl-CoA concentrations[13]. Especially mitochondria produce a high concentration of primary metabolites such as acetyl-CoA, succinyl-CoA and Glutaryl-CoA which are donors of their respective acyl group. Furthermore, the alkaline pH caused by high hydroxide concentration inside the mitochondrial matrix are adequate for nonenzymatic acylation reactions[6].

A change of acyl-CoA concentration inside cells (e.g. caused by fasting) can lead to hyperacylation of certain proteins which trigger the cellular adaptation (response) to the occuring event. Thus, lysine acylation reactions are linked to metabolic sensing due to their dependence on the metabolic intermediates acetyl-CoA, malonyl-CoA, succinyl-CoA and glutaryl-CoA[6].

1.1.4 NAD^+ -dependent Transferases

The addition and removal of PTMs, is usually catalyzed by a dedicated family of enzymes (KATs and KDACs). Some of these regulators consume NAD^+, by breaking the glycosidic bond at the adenosine diphosphoribosyl-nicotinamide linkage (see Figure 1.1). Nicotinamide (NAM) is released as a by-product of the reaction and the ADPR moiety acts as donor or acceptor for posttranslational modifications.

NAD^+ -dependent enzymes provide a direct link between the metabolic state of the cell* and adaptive signaling processes[14]. During situations of energy stress (e.g. low glucose levels), the cellular NAD^+ level increases and triggers the activity of

---

* Due to their dependence on NAD^+ concentration.

NAD$^+$ consuming enzymes such as mono-ADP-ribosyltransferases (ADPRTs), poly-ADP-ribose polymerases (PARPs) and Sirtuins (Sirts).

While ADPRTs catalyze the transfer of a single ADPR moiety (see Figure 1.1), PARPs transfer multiple ADPR moieties from NAD$^+$ molecules to their target residue[3]. In contrast, Sirtuins catalyze the transfer of specific acyl groups from a modified lysine residue to the ADPR moiety of NAD$^+$. This leads to O-acyl-ADP-ribose (OAADPR), a putative signaling molecule for downstream mechanisms[15].

A general overview of ADPRTs, PARPs and Sirts can be found in Table 1.1. This work focusses on bacterial ADPRTs as well as two specific Sirtuins which will be introduced in the following sections.

Enzymes	Catalyzed reaction	Target residues	Biological roles
ADPRTs	Mono-ADP-ribosylation	Arg, Asn, Diphthamide, Cys, Glu, Asp	General signaling processes in many biochemical pathways
PARPs	Poly-ADP-ribosylation	*Same as ADPRTs*	DNA repair, transcriptional regulation, energy metabolism, apoptosis
Sirtuins	Lysine deacylation	Acylated Lys	Transcriptional regulation, energy metabolism

Table 1.1: Overview of three types of NAD$^+$-dependent transferases.

1.2 Bacterial Toxins

Pathogenic bacteria target their host organisms by secreting virulence factors such as toxins. A large family of microbial toxins catalyze protein ADP-ribosylation by consuming NAD$^+$, an abundant cofactor inside the affected host cell[16]. Targets are usually key regulators of protein synthesis, signal transduction or cytoskeletal functions, that is why infections by bacterial toxins can cause critical deregulation and eventually cell death[17].

Bacterial ADPRTs are involved in widely known diseases such as cholera and diphteria, thus they affect the health of several million people per year. They are well studied and traditionally categorized into four families, as described in the following sections.

1.2.1 Classification of Bacterial ADPRTs

The molecular structure of bacterial ADPRTs typically consists of an enzymatic domain (A-domain) and a transport component (B-domain) responsible for the translocation into the target cell. Based on the specific domain organization and the nature of the target protein, they can be divided into the AB binary (C2-like), single A-domain (C3-like), AB$_5$ (CT-like) and AB multidomain (DT-like) toxins[18].

1.2.1.1 AB Binary Toxins

Binary toxins consist of a catalytic A-domain and a cell-binding B-domain which are expressed and secreted separately. B-domains bind as heptamer to specific receptors on the host cell surface and form the *docking site* for the A-domain. After binding to the heptamer, the A-domain is translocated into the host cell by endocytosis[19].
All AB binary toxins ribosylate Arg177 of globular G-actin, thereby inhibiting the polymerisation of actin to filaments (F-actin). This can lead to the collapse of the cytoskeleton, cell rounding and eventually cell death[20]. Moreover, actin depolymerisation produces microtubule-based membrane protrusions, which increases the adherence of further toxin-producing bacteria[21].
AB binary toxins are mainly secreted by *Clostridium* species, for example *Clostridium difficile* toxin (CDT), *Clostridium perfringens* Iota-toxin and *Clostridium botulinum* C2-Toxin.

1.2.1.2 Single A-Domain Toxins

Some ADPRTs consist only of a catalytic A-domain, thus lacking a translocation domain to enter the host cells. Examples are the C3 exoenzymes of *Clostridium botulinum* (C3-bot), *Clostridium limosum* (C3-lim) and *Staphylococcus aureus* (C3-stau).
These toxins ribosylate an asparagine residue of small GTPases* from the RHO-family, which prevents the binding of GTP and leads to an inhibition of several downstream processes[22]. However, most effects were studied in *in-vitro* systems, that is why the exact role of C3-like toxins in bacterial pathogenesis is still unclear.

1.2.1.3 AB$_5$ Toxins

One class of bacterial ADPRTs consists of an A-domain which is noncovalently bound to a pentamer of B-domains. Well known examples are the ADP-ribosylating toxins of *Vibrio cholerae* (CT) and *Bordetella pertussis* (PT)[23].
AB$_5$ toxins modify small regulatory G-proteins† which lock them in the GTP-bound state. This leads to a stimulation of the host adenylyl cyclase and results in an increased secretion of ions and water. Therefore, typical signs for cholera infections are diarrhea and vomiting of clear fluid.

1.2.1.4 AB Multidomain Toxins

Some of the most potent and lethal toxins consist of multiple domains, including receptor binding, transmembrane targeting and catalytic subunits. They ribosylate a diphthamide‡ residue of elongation factor 2 (EF2), which inhibits the association with other proteins that are part of the translational machinery[24]. Subsequently, the

---

* Guanosintriphosphat (GTP) binding proteins
† Guanine nucleotide-binding proteins
‡ Posttranslationally modified histidine

protein synthesis of the host cell is inhibited which leads to fundamental physiological changes up to cell death.

Examples of AB multidomain toxins are ADPRTs from *Corynebacterium diphtheriae* (DT), *Pseudomonas aeruginosa* (Exo-A) and *Vibrio cholerae* (Cholix-A). An overview of selected members from each toxin class can be found in Table 1.2. However, due to recently discovered atypical toxins, this traditional scheme will be continuously extended[25].

Toxin	Organism	Group	Substrate	Effects on Host Cell
CDT	*Clostridium difficile*	AB binary	Arg177 of G-actin	Inhibition of actin polymerisation
Iota	*Clostridium perfringens*	AB binary	Arg177 of G-actin	Inhibition of actin polymerisation
C3-bot	*Clostridium botulinum*	Single A-domain	Asn41 of Rho A-C	Disaggregation of actin cytoskeleton
C3-stau	*Staphylococcus aureus*	Single A-domain	Asn41 of Rho A-C and E	Disaggregation of actin cytoskeleton
CT	*Vibrio cholerae*	AB_5	Arg187 of $G\alpha_S$	Uncontrolled up-regulation of adenylate cyclase
PT	*Bordetella pertussis*	AB_5	Cys352 of $G\alpha_S$	Uncoupling of G-proteins from receptors
DT	*Corynebacterium diphtheriae*	AB multidomain	Diphthamide715 of EF-2	Inhibition of protein synthesis
Cholix-A	*Vibrio cholerae*	AB multidomain	Diphthamide715 of EF-2	Inhibition of protein synthesis

Table 1.2: Overview of selected bacterial toxins, their target substrate and physiological effects on the infected host cell. Table adapted from the review of Holbourn et al.[18].

1.2.2 Catalytic Mechanisms of Bacterial ADPRTs

ADP-ribosyltransferases catalyze the cleavage of NAD^+ and the subsequent transfer of the ADPR moeity to a specific amino acid residue of a target protein[3]. They bind NAD^+ in such a manner, that the N-glycosidic bond is strained and well positioned for hydrolysis. The anomeric carbon is subjected to a nucleophilic attack and NAD^+ is cleaved into nicotinamide and ADPR. The ADPR moeity is covalently linked to a nucleophilic sidechain of the target residue* and nicotinamide is released as by-product of the enzymatic reaction (see Figure 1.3).

∗ For example arginine, asparagine, diphthamide or cysteine.
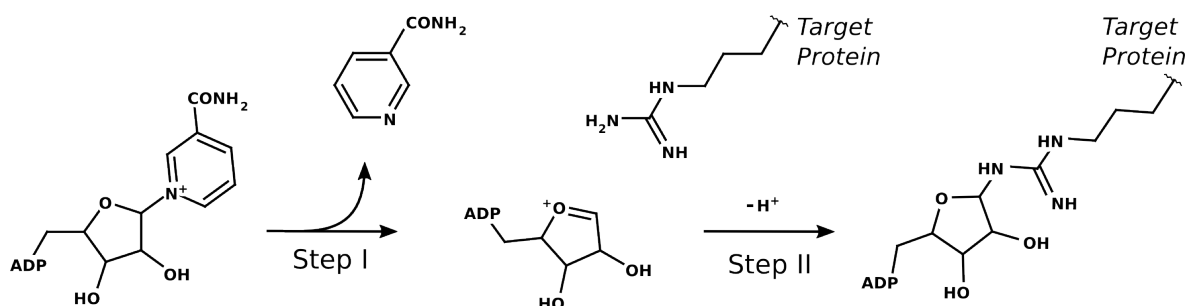
Figure 1.3: A proposed (S_N1 like) mechanism of the mono-ADP-ribosylation reaction catalyzed by bacterial ADPRTs. Step I: NAD^+ cleavage leads to nicotinamide release and an oxocarbenium cation intermediate; Step II: A nucleophilic attack of the intermediate (e.g. by the guanidino group of arginine) leads to the ADP-ribosylated product.

In principle, the nucleophilic attack can occur in two different ways:

S_N1: After NAD^+ cleavage, an isolated oxocarbenium intermediate is formed and stabilized by electrostatic interactions with toxin residues. Subsequently, the electrophile carbon of the intermediate is subjected to a nucleophilic attack by the target residue.

S_N2: The nucleophilic target residue attacks the exposed anomeric carbon of NAD^+ and a pentacoordinate oxocarbenium intermediate is formed and stabilized. Thereupon, the N-glycosidic bond is cleaved and the ADPR moeity is transferred to the target residue.

Due to structural and physicochemical differences between the four ADPRT classes, both mechanisms might be possible. However, S_N1-like reactions were favoured for Diphtheria and Iota toxin[26,27], whereas S_N2 was suggested for C3-bot and Pertussis toxin[28,29].
Proved by mutational studies, an invariant glutamate residue is essential for the ADP-ribosylation activity of bacterial ADPRTs[30]. Depending on the certain toxin, it might stabilize the oxocarbenium intermediate and/or contribute to NAD^+ hydrolysis and transfer of the ADPR moiety to the target substrate.

1.2.3 From Bacterial ADPRTs to Human PARPs

Eukaryotic organisms produce two classes of ADPRTs: Extracellular membrane-associated ADPRTs (Ecto-ARTs) and poly-ADP-ribose polymerases (PARPs).
While Ecto-ARTs are important for cell adhesion, cell communication, metabolism and the immune system[31], PARPs promote survival in response to DNA damage[32].
PARPS, Ecto-ARTs and bacterial ADPRTs exhibit only low sequence identity, but they share common structural and functional features at their NAD^+ binding sites[33].

Sequence alignments of their catalytical domains* revealed a number of conserved residues that coincide with key structural elements important for cofactor binding and catalysis. These structural motifs will be further described in Section 2.2, and the relationship between PARPs and ADPRTs will be used for virtual screening experiments in order to find common inhibitors (Section 2.9).

1.2.4 Therapeutic Potential of ADPRT Inhibitors

ADP-ribosylating enzymes play an important role in bacterial pathogenesis, by affecting key regulatory and structural proteins of infected host cells[17]. Antibiotics are the preferred treatment for bacterial infections, but increasing resistance rates trigger the need for alternative drug approaches[34]. One alternative strategy is the inhibition of toxic ADPRTs, to rescue the function of their human target proteins. Hence, they are attractive drug targets for treating diseases caused by bacterial infections.
Beside their therapeutic potential, ADRPTs are interesting enzymes to study cellular systems, such as the cytoskeleton or small GTPases[22]. In this context, specific inhibitors of actin-modifying toxins as well as CT- or C3-like ADPRTs are valuable tools for cell biologists. In summary, small molecules specifically designed to inhibit bacterial toxins have a great potential for pharmacology as well as cell biology.

1.2.5 Toxin Inhibitors

Although ADPRTs are interesting targets for treating bacterial infections, only a few inhibitors were reported until now[34]. In contrast, a considerable number of inhibitors were discovered for PARP enzymes and some of them are already subjected to clinical trials[35].
Due to the structural similarity between ADPRTs and PARPs, libraries of PARP inhibitors are valuable resources to find inhibitors of ADP-ribosylating toxins. Furthermore, crystal structures of PARP-inhibitor complexes can be used to guide virtual screening experiments and support the development of ADPRT-inhibitor binding models. An analog concept was recently proven for the bacterial toxins Cholix-A and Exo-A, whereat a number of inhibitors were discovered by *in-vitro* screenings of PARP inhibitor libraries. As shown by published crystal structures, common inhibitors such as NAP†, PJ34 and V30 (see Figure 1.4), share a common binding mode by mimicking the interactions usually observed for the nicotinamide moiety of NAD^+ [36].

---

*   See Appendix Section A.4.
†   4-amino-1,8-napthalamid
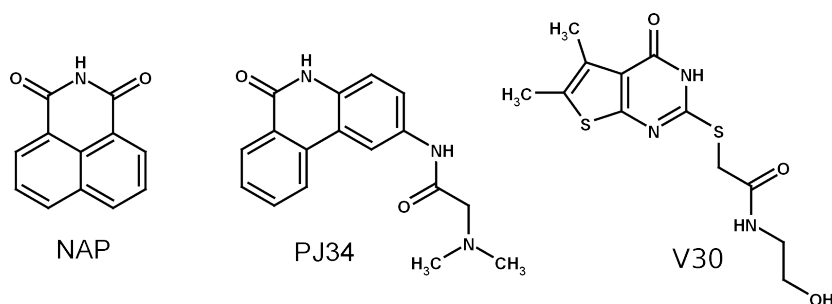
Figure 1.4: Non-specific inhibitors of human PARPs and bacterial ADPRTs from *Vibrio cholerae* (Cholix-A) and *Pseudomonas aeruginosa* (Exo-A)

1.3 Human Sirtuins

Sirtuins are a family of regulatory enzymes conserved in bacteria, archaea, yeast, viruses and mammals. Traditionally, they are described as NAD^+-dependent deacetylases removing acetyl groups from protein lysine residues of their respective target proteins[37]. However, recent studies uncovered additional roles of some Sirtuins which remove alternative lysine modifications such as propionyl, myristoyl, malonyl and succinyl groups[9,12,38].

The requirement of NAD^+ sets Sirtuins apart from other lysine deacetylase and links them to NAD^+ dependent enzymes such as ADPRTs and PARPs. Sirtuins modify diverse substrates including histones and non-histone proteins which are involved in transcriptional control, metabolic response and adoptosis[39,40]. In human, there are seven Sirtuin isoforms (Sirt1-7) showing specific subcellular localization, target substrates and biochemical functions.

1.3.1 Nuclear and Cytoplasmic Sirtuins

Sirt1, Sirt6 and Sirt7 are mainly located in the nucleus and involved in functions such as transcription control, DNA repair and metabolic response[41]. Sirt1 targets a wide range of substrates including histones and non-histone proteins. It was shown that Sirt1-dependent histone deacetlyation facilitate the formation of heterochromatin which results in gene silencing[42].

Sirt6 has been reported as deacetylase of histones and DNA-polymerase, thereby having a regulatory role in gene transcription and DNA repair[43]. Recent studies demonstrated an efficient removal of long fatty acid chains (such as myristoyl) and suggested a role in the regulation of protein secretion[38].

Sirt7 is located in nucleolus and has only weak deacetylase activity. Putative substrates are histones, p53 and the RNA polymerase I transcriptional machinery, thus Sirt7 activity is linked to cell proliferation and gene transcription[44].

While most Sirtuins can shuttle to cytoplasma, Sirt2 is the main cytoplasmic Sirtuin involved in cell-cycle regulation, cellular differentiation and oxidative stress response.

Various Sirt2 targets are confirmed, such as α-tubulin, FOXO proteins and p300. Their regulation might be relevant for microtubule stabilization and neurodegenerative processes such as Alzheimers and Parkinsons disease[40,45].

1.3.2 Mitochondrial Sirtuins

Sirt3-5 are predominantly located in the mitochondria, the central organelle for energy production and metabolism in human cells. They act as important metabolic sensors by deacylating key metabolic enzymes in response to nutrial conditions[46,47].
Sirt3 is the main deacetylase in mitochondria, targeting several enzymes involved in fatty acid metabolism and gluconeogenesis. Thereby, Sirt3 induces the metabolic switch from glucose to lipids and amino acids metabolism during low nutrient conditions[48,49].
Sirt4 inhibits glutamate dehydrogenase (GDH) and subsequently represses insulin secretion[50]. Very recently, the enzyme was reported as efficient lipoamidase that inhibits the activity of the pyruvate dehydrogenase complex (PDH) and thereby regulates cellular metabolism[51]. In Chapter 4, a protein model of Sirt4 as well as binding modes of putative substrates and inhibitors from virtual screening will be described.
Sirt5 shows efficient demalonylase, desuccinylase and deglutarylase activity in *in-vitro* as well as *in-vivo* experiments[12,52]. By deacylating and activating carbamoyl phosphate synthetase 1 (CPS1)*, Sirt5 plays an important role in detoxification of ammonia when amino acids are used as energy source†[53]. In Chapter 3, the molecular structure of Sirt5 as well as binding modes of substrates and inhibitors will be discussed in detail.

1.3.3 Biological Roles of Sirtuins

The broad subcellular distribution, the requirement of NAD^+ and the deacylation chemistry place Sirtuins at the center of various pathways. They play a key role in the metabolic regulation in response to nutritional stress like dietary or calorie restriction (CR)[54]. During CR, Sirtuin expression and activity is increased possibly by the higher levels of cellular NAD^+. The CR-induced switch from glucose to amino acid catabolism produces ammonia which needs to be converted to urea. Therefore, an increased activity of Sirt5 is necessary to accelerate the urea cycle via activation of the rate-limiting enzyme CPS1[47].
Further biological roles are confirmed, including adipogenesis, gene silencing and DNA repair mainly mediated by the nuclear Sirtuins. The deacetlyation of histones and transcription factors and thereby regulation of gene transcription provide an interesting link between the metabolic state of the cell and epigenetic adaption[55]. A short overview of the seven human Sirtuins and their main functions can be found in Table 1.3.

∗   CPS1 is a critical enzyme in the first step of the urea cycle.
†   For example during caloric restriction.

Sirtuin	Localization	Activity	Selected Substrates	Biological Functions
Sirt1	Nucleus, Cytoplasma	Deacetylation	Histones, p53, FOXO proteins, ACS1, PGC-1α, p300, NFκB	Cell survival, metabolism, stress response
Sirt2	Cytoplasma, Nucleus	Deacetylation	α-tubulin, histones, p53, p300, PAR3, FOXO proteins	Cell-cycle regulation, stress response
Sirt3	Mitochondria, Nucleus, Cytoplasma	Deacetylation	FOXO proteins, GDH, ACS2, IDH2, p53, histones	Energy metabolism, adoptosis, stress response
Sirt4	Mitochondria	Delipoylation	PDH, GDH	Regulation of insulin levels and glutamine metabolism
Sirt5	Mitochondria	Desuccinylation, Deglutarylation	CPS1, UOX, SOD1	Activation of urea cycle
Sirt6	Nucleus	Deacetylation, Deacylation	Histones, NBS1	Glucose/ lipid homeostasis, genomic stability
Sirt7	Nucleolus	*unknown*	Histones, RNA Pol-I, p53	Chromatin regulation

Table 1.3: An overview of subcellular localization, enzymatic activity, selected substrates and biological functions of the seven human Sirtuins.

1.3.4 Catalytic Mechanisms of Sirtuins

Although ADP ribosylation activity was described for several Sirtuins, protein lysine deacylation is the most relevant reaction catalyzed by these enzymes[56]. During deacylation, an acyl group is removed from a modified lysine residue by cleaving the nicotinamide-ribose bond of NAD^+ and transferring the acyl group to the 2' hydroxyl of ADPR[57]. The catalytic reaction results in the release of nicotinamide (NAM), O-acyl-ADPR (OAADPR) and the deacylated protein lysine residue. OAADPR might be a messenger molecule for further downstream processes and NAM can compete with subsequent deacylation reactions by permitting reformation of NAD^+ (base-exchange reaction)[58,59]. The proposed ADPR-peptidyl imidate mechanism is unique among any other known enzymes and requires a number of invariant residues as well as water molecules inside the binding cleft of Sirtuins.

1.3.4.1 The ADPR-peptidyl Imidate Mechanism

Initially, NAD^+ binds in an extended conformation where the NAM moiety of NAD^+ is positioned nearby the substrate lysine binding channel*. The binding of the acylated substrate protein induces a conformational change of the Sirtuin binding cleft which forces NAD^+ into a strained conformation, cabable of undergoing nucleophilic attacks[60].

---

* See Section 3.2 for details on the Sirtuin structure.

Distinct processes can lead to the cleavage of NAM and the formation of an ADPR-peptidyl imidate intermediate:

S_N1: The NAM moiety of NAD^+ is dissociated and an oxocarbenium ion intermediate is attacked by the carbonyl oxygen of the substrate lysine acyl group.

S_N2: The carbonyl oxygen of the lysine acyl group might attack the anomeric carbon of the NR moiety which results in a bonding between NAD^+ and the nucleophile. The NA moeity of NAD^+ is subsequently cleaved from the intermediate.

However, the exact mechanism is still an open question and possibly distinct Sirtuins might proceed through different transition states[57].

After nucleophilic attack of NAD^+, the ADPR-peptidyl imidate intermediate is formed (see Figure 1.5, step I). The imidate can reverse to the reactants by a base-exchange reaction or react forward via 2'-OH attack on the imidate to complete deacylation. In the latter case, the NR 2'-OH is deprotonated (activated) by a conserved histidine residue and attacks the imidate at the carbonyl carbon to form a 1',2'-cyclic intermediate (see Figure 1.5, step II). The bicyclic intermediate is subsequently eliminated to an oxonium species (see Figure 1.5, step III) and hydrolyzed to a mixture of 2'-OAADPR and 3'-OAADPR (see Figure 1.5, step IV).
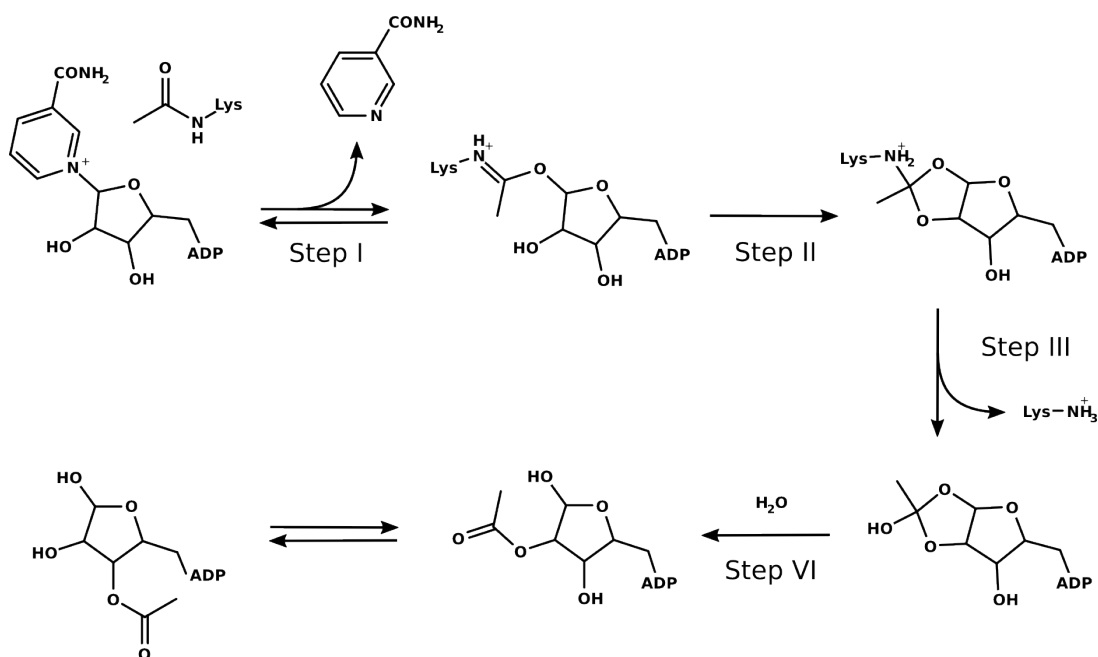

Figure 1.5: General mechanism of Sirtuin-catalyzed protein lysine deacetylation. Step I: NAD^+ cleavage and formation of ADPR-peptidyl imidate intermediate; Step II: Formation of a bicyclic intermediate; Step III: Formation of an oxonium intermediate; Step IV: Hydrolysation to a mixture of 2'-OAADPR and 3'-OAADPR.

1.3.4.2 The Base-Exchange Reaction

The first step of the Sirtuin catalytic mechanism shows a reversible cleavage of the nicotinamide-ribose bond of NAD^+ (see Figure 1.5, step I). After the generation of the imidate intermediate, the deacetylation reaction compete with the reformation of NAD^+ by a base-exchange mechanism. Nicotinamide, which is a better nucleophile than the acetyl oxygen, can attack the anomeric carbon of the imidate in order to restore a NAD^+ molecule[61].

However, kinetic studies confirmed that the steady-state deacetylation rates are usually higher than steady-state base-exchange rates. Therefore, the imidate intermediate serves a checkpoint for deacetylation or base-exchange, depending on the current NAM concentration[15].

1.3.5 Therapeutic Potential of Sirtuin Inhibitors

Sirtuins are involved in important physiological processes such as gene transcription, cancer protection, inflammation and energy metabolism. Their activity mimics the positive effects of caloric restriction, which has a number of benefits for the affected organism[40,54]. Thus, modulation of Sirtuins might have beneficial effects on various human diseases such as metabolic disorders, neurodegeneration and cancer[62].

Sirtuin activators might be promising due to their potential to mimic CR-related effects, but also Sirtuin inhibitors are of interest, e.g. for supporting cancer therapy[63,64]. However, a number of Sirtuin modulators have been reported in the last decade, which can be classified according their chemical scaffold or pharmacophore. A short overview of some established compounds will be provided in the following sections.

1.3.6 Peptidic and Pseudopeptidic Inhibitors

Peptides based on Sirtuin substrates, containing a thioacylated instead of an acylated lysine, are potent Sirtuin inhibitors. They attack NAD^+ like the substrate, but form a stable inhibitor-ADP-ribose conjugate, thus stalling the catalytic imidate intermediate[65,66]. Further peptidic inhibitors were reported recently[67], including several CPS1 derived inhibitors which will be discussed in Section 3.6.2.

1.3.7 Small Molecule Inhibitors of Sirtuins

1.3.7.1 Nicotinamide and NAD^+ Derivatives

The activity of all Sirtuins can be inhibited by NAM as a consequence of the base-exchange reaction (see Section 1.3.4.2). However, the therapeutic use of NAM is limited, because the compound inhibits various NAD^+-dependent enzymes and is directly involved in many metabolic pathways. The related compound 2-Anilinobenzamide (see Figure 1.6 (A)) also inhibits Sirt1 and shows a moderate selectity over Sirt2 and Sirt3[68]. The non-hydrolysable Carba-NAD^+ is another inhibitor of many NAD^+-dependent enzymes, by competing with NAD^+ but not permitting a cleavage of the NAM moiety[69].

1.3.7.2 β-Naphthol Derivatives

Sirtinol (see Figure 1.6 (B)) was one of the first discovered Sirtuin inhibitors and contains a 2-hydroxyl-1-naphthol moiety that is crucial for activity[70]. Salermide (see Figure 1.6 (C)) is structurally related to Sirtinol, but shows a higher potency on Sirt1 and Sirt2[71]. Cambinol (see Figure 1.6 (D)) is another substrate competitive inhibitor of Sirt1-2 and Sirt5 and showed antitumor effects in studies on mouse models[72].

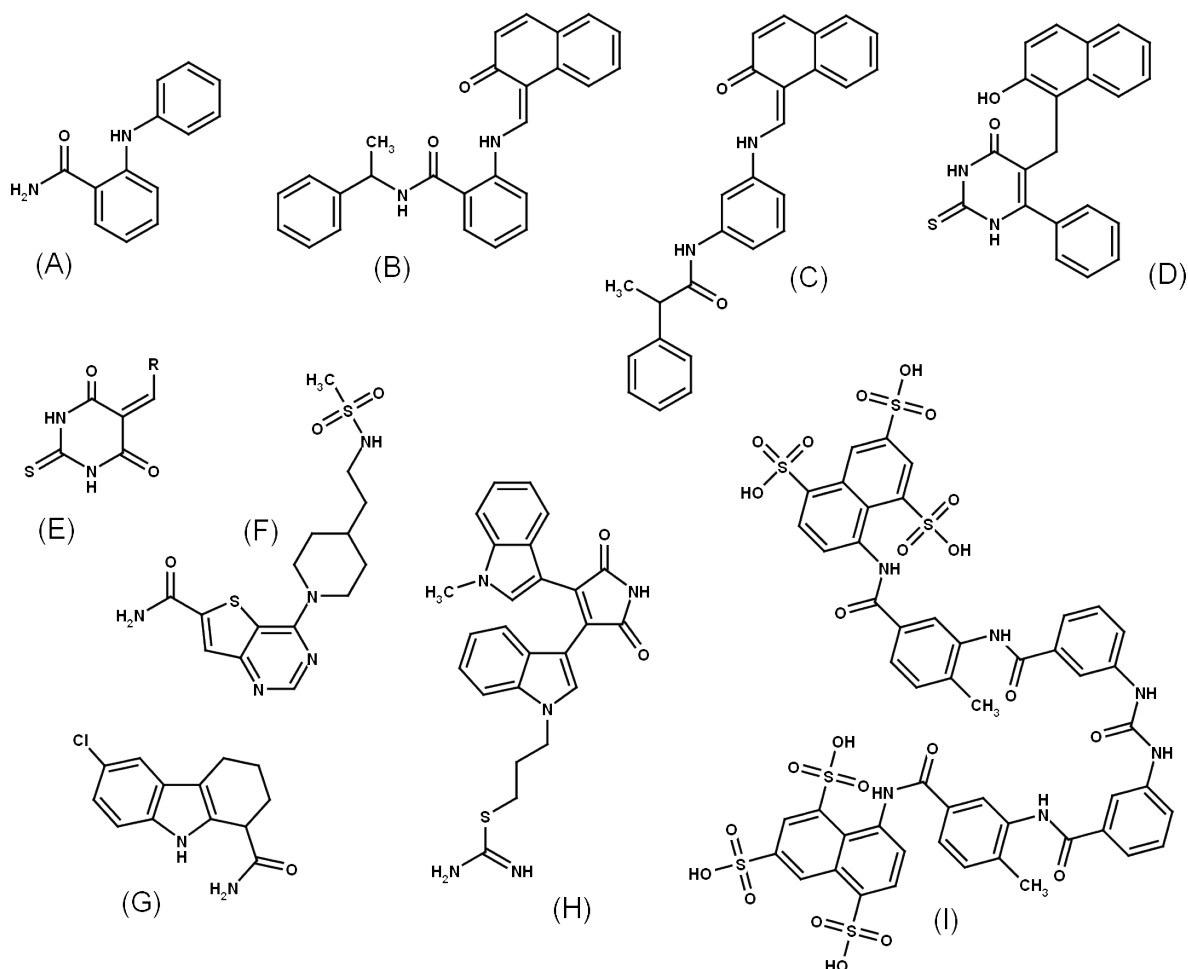**Figure 1.6:** Established Sirtuin inhibitors: (A) 2-Anilinobenzamide; (B) Sirtinol; (C) Salermide; (D) Cambinol; (E) Thiobarbiturates; (F) ELT-31; (G) EX-527; (H) Ro-31-8220; (I) Suramin.

1.3.7.3 Indoles

Several indoles were found to be potent and selective inhibitors of Sirt1 in *in-vitro* as well as *in-vivo* experiments[73]. The most promising derivative EX-527* (see Figure

---

∗ Selisistat

1.6 (G)), showed mixed-type inhibition against substrate and cofactor by blocking the nicotinamide binding site of NAD^+ [74]. The therapeutic potential of this compound is currently analyzed in clinical trials for neurodegenerative diseases. The bisindolyl-maleimide Ro-31-8220 (see Figure 1.6 (H)), was discovered as a potent inhibitor of Sirt1-3 without effecting Sirt5 activity[75].

1.3.7.4 Barbiturates and Thiobarbiturates

Compounds containing a barbiturate or thiobarbiturate scaffold (see Figure 1.6 (E)) were initially discovered as Sirt2 inhibitors by a virtual screening approach[76]. They are structurally related to Cambinol and inhibit all types of Sirtuins tested so far[77]. This class of compounds will be further discussed in Section 2.7 and 3.7.

1.3.7.5 ELT Inhibitors

A number of thienopyrimidine derivatives (see Figure 1.6 (F)) were identified as potent inhibitors of Sirt1-3[78]. Since some of these compounds were co-crystallized with Sirt3, they are valueable scaffolds for structure-based research on Sirtuins.

1.3.7.6 Inhibitors Containing other Scaffolds

Suramin (see Figure 1.6 (I)) is an approved drug for the treatment of sleeping sickness and showed antiviral and anticancer activities[79]. The compound inhibits several Sirtuins, but also other proteins such as G-proteins, reverse transcriptase and topoisomerase[80]. Table 1.4 gives an overview of all described compounds and their activity data on several Sirtuin isoforms.

Inhibitor	Sirt1 IC_{50} [µM]	Sirt2 IC_{50} [µM]	Sirt3 IC_{50} [µM]	Sirt5 IC_{50} [µM]
NAM	25.0-100.0	1.2-100.0	30.0	46.6
Sirtinol	37.0-131.0	38.0-57.7	24% at 50µM	48.9-100.0
Salermide	40.3-42.8	25.0	n.d.	n.d.
Cambinol	40.7-57.9	40.7-59.0	n.i.	42.5
EX-527	0.1-1.3	19.6-48.5	49.0	n.i.
Suramin	0.3-2.8	1.1-20.0	n.i.	22.0-46.6
Ro-31-8220	3.5-25.0	0.8-1.1	3.7	n.i.
ELT-31	0.004	0.001	0.007	n.d.

Table 1.4: Overview of established Sirtuin inhibitors. The inhibition values were derived from the cited literature as well as Pubchem entries.

1.4 Aims of this Thesis

The growing number of cellular pathways linked to the activity of NAD^+-dependent enzymes, leads to a demand for novel, potent and selective inhibitors. Such compounds are necessary to characterize the chemical and biological nature of these proteins and to proof their therapeutical relevance. It seems likely, that many NAD^+ consumers are attractive drug targets for a variety of human diseases such as bacterial infections, neurodegeneration or metabolic disorders.

However, despite intensive efforts to identify novel lead compounds, there are still substantial gaps in our knowledge regarding structural properties of these targets. Furthermore, for some NAD^+ consumers such as bacterial toxins and Sirtuins, only a few inhibitors are reported and almost nothing is known about their mode of action.

This work focussed on three NAD^+-dependent enzymes which were not well studied until now: The ADP-ribosylating toxin CDT, the human Sirt4 as well as human Sirt5. In order to characterize these putative drug targets, a combination of molecular modeling, virtual screening and classical *in-vitro* screening was carried out with the goal to find novel inhibitor candidates.

Available crystal structures were analyzed in detail to develop reliable models of proteins and protein-ligand complexes. Therby, important aspects such as conformational flexibility and pocket solvation were considered. Knowledge gained from the generated models was integrated into virtual screening campaigns and selected virtual hits were experimentally tested by our colleagues at University Freiburg[*].

This thesis summarizes the results of this work within the following three chapters:

- Chapter 2 describes computational studies on CDT, including docking and virtual screening experiments.

- Chapter 3 focuses on the structure analysis of Sirt5, the development of protein-ligand binding models and several virtual screening rounds to discover Sirt5-specific inhibitors.

- Chapter 4 covers the modeling of a Sirt4 protein structure and the prediction of putative substrates as well as inhibitors.

---

[*] Dr. Benjamin Maurer, group Prof. Manfred Jung, University Freiburg, Germany

CHAPTER 2

Molecular Modeling Studies on *Clostridium Difficile* Binary Toxin

2.1 Introduction

The gram-positive bacterium *Clostridium difficile* produces a number of virulence factors which are critical for human and animal health. Infections are associated with diseases such as antibiotic-associated diarrhea and pseudomembranous colitis and cause thousands of hospital deaths per year[81].

The pathogenicity of *Clostridium difficile* has been linked to the production of three specific enzymes: Two large exotoxins, Toxin-A and Toxin-B, which catalyze the monoglycosylation of Rho GTPases, and the binary ADP-ribosyltransferase CDT which targets G-actin. ADP-ribosylation of G-actin inhibits the polymerization to filamentous F-actin and leads to the collapse of the cytoskeleton of the infected host cell[82]. Furthermore, it was shown that actin depolymerisation by CDT produces microtubule-based membrane protrusions which increase bacterial adherence[21]. While the exact pathogenic role of all three toxins is still discussed, CDT positive strains have become increasingly prevalent in the last decade[83].

Bacterial infections are usually treated with antibiotics, but their usage promotes the gut colonization process of *Clostridium difficile*[84]. Furthermore, increased antibiotic resistance rates were observed during the last decades, that is why alternative therapeutics have to be developed[34].

A direct inhibition of CDT catalyzed ADP-ribosylation would be a promising strategy, but there are no such compounds reported so far. However, a few inhibitors were published for the related toxins Cholix-A and Exo-A and several crystal structures provided insights into their mode of binding[36]. In combination with the recently resolved structure of CDTa, this data provides an appropriate starting point for structure-based virtual screening (SBVS) campaigns.

However, a characterization of structural aspects such as conformational flexibility and pocket solvation is essential for the success of any SBVS approach[85,86]. Therefore, the molecular structure of CDTa was analyzed in detail and gained insights were incorporated into the development of protein-ligand models as well as several virtual screening protocols.

2.2 The Molecular Structure of CDT

The structure of CDT is composed of a transport component (CDTb) and an enzymatic component (CDTa) that catalyzes the ADP-ribosylation of monomeric actin[81]. Recently resolved crystal structures of CDTa showing an N-terminal domain (residues 1-215) and a C-terminal domain (residue 224-420) which are linked by a short loop (see Figure 2.1)[87]. The N-domain interacts with the translocation component CDTb to enter the host cell via endocytosis[88]. The C-Domain of CDTa includes the catalytic site and consists of several key motifs important for NAD$^+$ binding and transfer of the ADPR moiety to the target residue*.
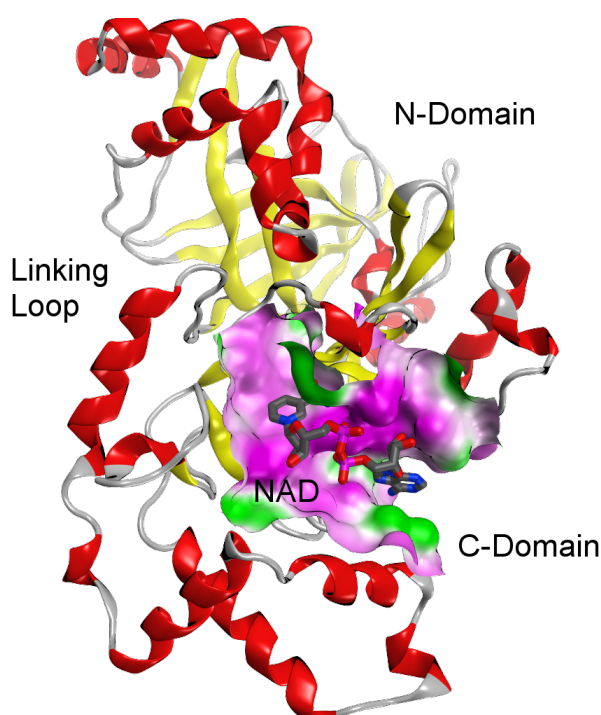
Figure 2.1: Ribbon representation of catalytic domain CDTa. The NAD$^+$ binding pocket is colored according hydrophobic (green) and hydrophilic (pink) regions.

2.2.1 Active Site of CDTa

The NAD$^+$ binding pocket of CDTa is situated in a deeply buried cleft within the C-Domain and shows a typical fold of ADP-ribosylating toxins[87]. Despite a low sequence identity among ADPRTs and PARPs, the following structural feature are highly conserved in many structures of both enzyme families[18]:

---

* Arg177 of human G-actin.

Arom-H/R motif: An aromatic residue followed by an arginine[*], both of which are essential for binding NAD^+ in an optimal conformation for nucleophilic attack. The side chain of Arg302[†] forms a hydrogen bond with the phosphate oxygen of NAD^+ , and the backbone of Arg303 coordinates the nicotinamide moiety by hydrogen bonding with the amide group.

STS motif: The Ser-Thr-Ser pattern is involved in NAD^+ binding and is critical for the catalytic process. The first serine (Ser345) interacts with the nicotinamide ribose of NAD^+ and orients the catalytic glutamate (Glu387) for nucleophilic attack. Thr346 stabilizes the NAD^+ pocket by hydrogen bonding with other residues and Ser347 interacts with the substrate recognition loop (ARTT-loop, see Section 2.3.3).

PN loop: A flexible loop that forms the active site and is involved in NAD^+ binding. Arg359 is essential for catalytic activity by forcing NAD^+ into an optimal conformation. The aromatic side chain of Phe356 interacts by π-stacking with the nicotinamide ring of NAD^+.

Q/E-x-E motif: This motif is located on the conformationally flexible ARTT-loop and contains the invariant catalytic Glu387. This glutamate is essential for ADP-ribosylating activity by binding to the 2'-OH of the nicotinamide ribose and thereby forcing NAD^+ into an optimal conformation for hydrolysis. An upstream glutamate (Glu385) promotes the transfer of ADPR moiety to the target residue of the substrate[89].

Figure 2.2 shows the location of all four motifs and Figure 2.3 illustrates the interactions between CDTa residues and NAD^+. Interestingly, most of these conserved residues contribute to nicotinamide and pyrophosphate binding and none of them interacts with the adenosine part of NAD^+.

---

[*]   Or histidine in DT-like toxins and PARPs.
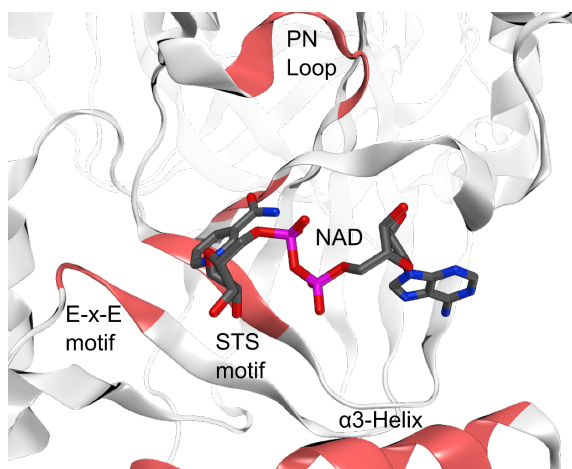[†]   CDTa numbering is used in this chapter.

Figure 2.2: Ribbon representation of CDTa pocket. Regions conserved among ADPRTs are highlighted in red.
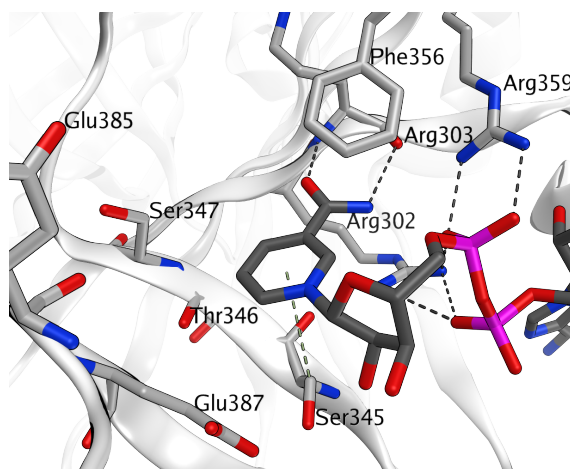
Figure 2.3: Interactions between NAD$^+$ and CDTa residues. Hydrogen bonds are drawn as dashed lines.

2.2.2 Structural Conservation and Characteristics of CDTa

Despite the common structural features described in Section 2.2.1, a number of differences between individual toxins exist: The STS motif of C2- and C3-toxins is replaced by a Y-X$_{10}$-Y motif in the case of DT-like ADPRTs*, at which the two tyrosine residues interact with the nicotinamide moiety of NAD$^+$.

The PN-loop and an additional helix (α3-helix, see Figure 2.2) seems to be typical for C2- and C3-like toxins and contributes to a relative compact binding site. CT- and DT-like toxins show a loop at the same position which is important for substrate recognition. Interestingly, the upstream glutamate of the E-x-E motif seems to be specific for Arg-modifying ADPRTs, because this residue is replaced by a glutamine in the case of Asp-specific toxins or even missing in other toxins. Furthermore, a tyrosine residue (Tyr382) three positions upstream from the E-x-E motif is only present in actin and Rho GTPase modifying toxins. It seems likely that both residues are involved in the recognition and ribosylation of subtype specific substrates. However, targeting such characteristic features is a promising strategy to end up with toxin specific inhibitors. All described motifs and their degree of conservation are summarized in Table 2.1.

∗   See sequence alignments in Appendix Section A.4.

Motif	Pattern	CDTa res.	Conservation	Function
α3 motif	Y-X_7-IN-X_2-L(R/I)	253-266	C2-like, C3-like	Active site formation
Arom-H/R	(Y/F)(H/R)	301-302	All toxins	Active site formation; Binding of NAD^+
STS motif	*Arom.-Hydrophob.-*ST(S/Q)	345-347	C2-like, C3-like, CT-like	Stabilization of NAD^+ pocket and NAD^+ binding
PN loop	(A/G)-X-R-X-I	357-361	C2-like, C3-like	Active site formation; Binding of NAD^+
Q/E-x-E motif	(Q/E)-X-E	385-387	C2-like, C3-like, CT-like	Substrate recognition; Catalytic mechanisms

Table 2.1: Conserved structural motifs found at the catalytical domain of bacterial toxins.

2.3 Conformational Analysis of CDTa

Proteins are dynamic molecules which change their conformations over time and upon binding with other molecules. To predict accurate protein-ligand models, a detailed analysis of structural flexibility is quite important. Such informations can be obtained from NMR spectroscopy, or alternatively predicted by *in-silico* methods such as Molecular Dynamics (MD) simulations[90]. However, a significant variability was already described for other ADPRTs[91], that is why the conformational space of CDTa was analyzed in detail during this work.

2.3.1 Conformations of NAD^+ Bound to Various Enzymes

NAD^+ consists of several functional groups connected by more than ten rotatable bonds - thus, there are numerous ways, how NAD^+ can interact at protein binding sites. The explicit protein-bound conformation of NAD^+ depends on the active site characteristic and is usually conserved within a protein family but distinct among other types of enzymes[92].

While such differences were already described for redox and nonredox enzymes[93], a comparison between individual NAD^+ dependent transferases is still missing. To fill this gap, a number of NAD^+ conformations were extracted from representative members of each toxin family* and compared with conformations obtained from other NAD^+ dependent transferases as well as oxidoreductases.

The similarity was assessed by a rigid alignment of all NAD^+ conformations and a hierarchical clustering of their pairwise root-mean-square deviation (RMSD) values†. The obtained cluster indices, as well as the RMSD values to the reference conformation

---

∗ See section 1.2.1.
† Protocols see Appendix Section A.5.

(NAD^+ bound to CDT) are shown in Table 2.2. As indicated by low RMSD values, NAD^+ binds in a highly similar shape to all bacterial ADPRTs. This characteristic *ring-like* conformation is stabilized by an intramolecular bond between the carboxamide group and one of the phosphate oxygens (see Figure 2.4A).

(A)

(B)

Enzyme	Class	RMSD to CDT-NAD$^+$	Cluster Index
CDT	AB binary toxin	0.00 Å	1
Iota	AB binary toxin	0.44 Å	1
C3-bot	A-domain toxin	1.12 Å	2
C3-stau	A-domain toxin	1.24 Å	2
CTA	AB$_5$ toxin	1.35 Å	2
Cholix-A	AB multidomain	1.36 Å	3
DT	AB multidomain	1.81 Å	3
Sirt1	Sirtuin	3.03 Å	4
Sirt3	Sirtuin	3.78 Å	4
Sirt5	Sirtuin	2.23 Å	5
ADPRAC	ADPR-cyclase	3.38 Å	6
HLADH	Dehydrogenase	3.74 Å	7
NADK	NAD-Kinase	4.35 Å	8

Table 2.2: Similarity between NAD^+ conformations as bound to various enzymes. RMSD clusters were obtained from three individual runs of the hierarchical cluster algorithm.
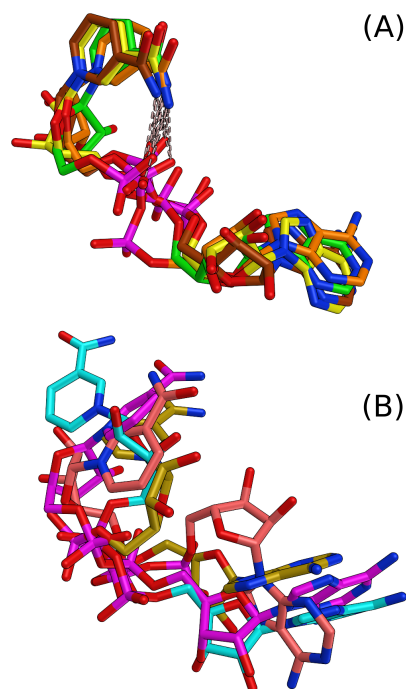
Figure 2.4: A: CDT (green), C3-bot (yellow), CTA (brown), Cholix-A (orange); **B:** Sirt5 (purple), ADPRAC (pink), HLADH (blue), NADK (gold)

This conformation is strongly connected to conserved structural features such as the invariant Arom-H/R motif and the STS motif (see Section 2.2.1 and Figure 2.3). They are involved in NAD^+ binding and force the nicotinamide mononucleotide moiety in a strained conformation that orients the glycosidic bond for subsequent nucleophilic attack.

Interestingly, the degree of conformational similarity (RMSD value and cluster index) seems to be connected to the classification scheme of bacterial ADPRTs[*]: Cluster-1 includes only AB-binary toxins, Cluster-2 includes single-A and AB$_5$ toxins and Cluster-3 exclusively AB multidomain toxins. Thus, a decreased protein homology caused by amino acid substitutions (e.g. STS motif to Y-X$_{10}$-Y motif), directly affects the binding conformation of NAD^+.

∗   See Section 1.2.1.

However, while NAD^+ binds very similar to all analyzed ADPRTs, other NAD^+-dependent enzymes prefer totally different conformations (see Figure 2.4B). Interestingly, although some of these proteins share a common Rossmann fold domain[94], they clearly prefer distinct conformations of NAD^+ and none of them showed the characteristic intramolecular bond observed for bacterial ADPRTs.

In summary, the preferred conformation of NAD^+ depends on structural and physico-chemical properties of the individual binding pocket and is linked to the type of reaction that is catalyzed by this enzyme. Therefore, the development of specific toxin inhibitors is possible, although they share the same cofactor as other NAD^+-dependent enzymes such as Sirtuins, PARPs and oxidoreductases.

2.3.2 Conformational Flexibility of CDTa

Different (pH-dependent) protein conformations were already observed from X-ray studies on CDTa[87]. However, only a few crystal structures were published until now, that is why an *in-silico* analysis of conformational flexibility was carried out during this work. A 70 nanoseconds MD simulation was carried out for the unbound structure of CDTa (*MD-apo*) as well as the NAD^+ bound complex (*MD-holo*)*.

Atomic motions are usually quantified by temperature factors (B-factors), whereas analogous information can be calculated from a trajectory produced by MD simulations[95]. Both values can be directly compared by normalizing them to zero mean and unit variance[96], that is why such an analysis was carried out for both CDTa structures and the corresponding MD simulation output†. Figure 2.5 shows such a comparison, by plotting the experimental B-factors of CDTa and their corresponding simulation values in the same B-factor profile. It can be easily seen, that the experimentally and computationally determined quantifiers are in good agreement, thus the simulation results can be assumed as accurate enough to analyse them in detail.

As indicated in Figure 2.5, the N-domain of CDTa consists of several flexible regions, whereas the catalytic domain seems to be more stable. Only two areas showed a significant high flexibility inside the C-Domain: The first peak (residues 270 to 280) corresponds to a solvent exposed loop distant from the active site and the second peak (residues 380 to 390) shows the well known flexibility of the ARTT loop‡.

Most of the other pocket residues were conformationally stable, including the α3-helix, the STS-motif and the PN-loop (especially in the NAD^+ bound state of CDTa). To analyze different CDTa conformations in detail, a hierarchical clustering was done for the *MD-apo* trajectory§ and three cluster representatives were compared with crystal structure of CDTa. As shown in Figure 2.6, the pocket models obtained from the unbound simulation of CDTa were highly similar to the crystal structures in NAD^+-bound state. Especially amino acids which are involved in nicotinamide mononucleotide

---

*   Protocols see Appendix Section A.6.1.
†   Protocols see Appendix Section A.6.2.
‡   Further discussed in Section 2.3.3.
§   Protocols see Appendix Section A.6.3.

binding were conformationally stable, that is why this region seems to be adequate for the structure-based design of toxin inhibitors. Interestingly, this part of the NAD^+ pocket is structurally conserved, not only in the whole toxin family but also in serveral PARP and Ecto-ART structures[33].
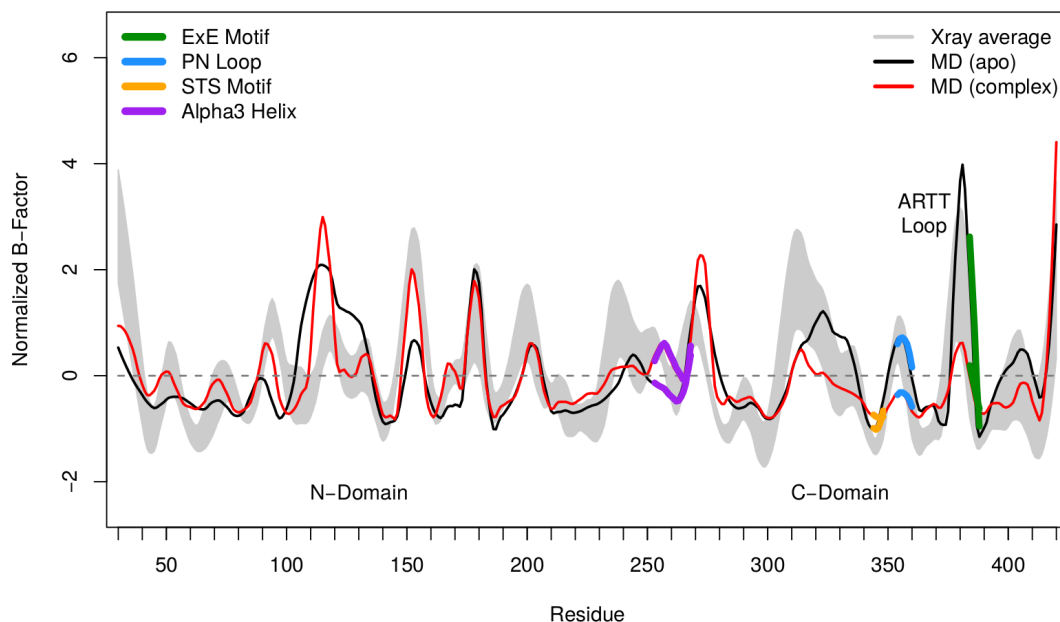

Figure 2.5: Averaged B-factors from all available crystal structures (gray) are compared with computationally determined values obtained from the unbound simulation of CDTa (*MD-apo*, black) and the NAD^+ bound complex (*MD-holo*, red). All B-factors are normalized to zero mean, thus values below zero indicate an above-average stability and values higher than zero are a sign of structural flexibility.

2.3.3 ARTT Loop Flexibility

The ADP-ribosylating turn-turn loop (ARTT loop, residues 377 to 387) is a highly dynamic region, involved in substrate recognition and ADP-ribosylation mechanisms[97,98]. As can be seen in Figure 2.5, the loop is stabilized upon NAD^+ binding, which might be necessary for substrate interactions, nucleophilic attack of NAD^+ and the subsequent transfer of the ADPR moeity. A critical role was suggested for both glutamate residues of the E-x-E motif (Glu385 and Glu387) and an upstream tyrosine residue (Tyr382). Therefore, these residues were further analyzed in respect to putative side chain conformations - either in absence of or with bound NAD^+.

During the ligand-free simulation of CDTa, Tyr382 and Glu385 adopt many different conformations, either pointing outwards or flipping inside the NAD^+ pocket of CDT (see Figure 2.7). In contrast, Glu387 was much more stable and stayed at nearly the same position as observed in all crystal structures. However, it can not be guaranteed that all relevant conformations were sampled by the conventional MD simulation approach, but it was pointed out that several ARTT loop conformations need to be incorporated
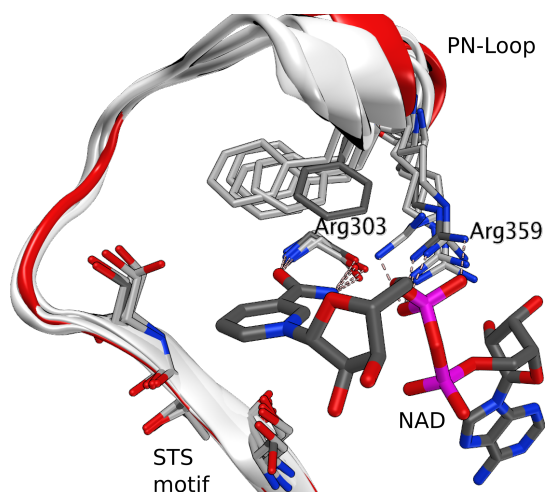
in the development of CDT-ligand binding models.

Figure 2.6: Only minor differences were observed for the superimposed structures of CDTa with bound NAD$^+$ (red) and three representative snapshots obtained from a clustering of the MD-apo trajectory (grey).

Figure 2.7: ARTT-loop conformation observed for the superimposed structures of CDTa with bound NAD$^+$ (red) and three representative snapshots obtained from a clustering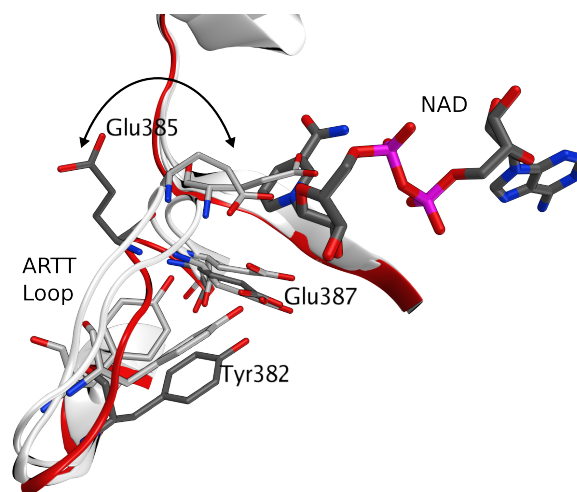 of the MD-apo trajectory (grey). Glu385 flipped inside the NAD$^+$ pocket and occupied the binding pocket of nicotinamide.

2.4 Water Molecules in the NAD$^+$ Pocket

Water contributes to protein structure and is frequently involved in binding processes as well as catalytic mechanisms[99]. Knowledge on water locations inside binding pockets is crucial to generate reliable protein-ligand models and might help to improve binding affinity. Due to the lack of such information for CDT and bacterial ADPRTs in general, several toxin structures were inspected for common co-crystallized waters.

Important waters are usually conserved within distinct structures of the same protein and also among several structures of homologous proteins[99]. In order to detect such waters for bacterial ADPRTs, CDTa was superimposed with three related C2-like and C3-like toxins, namely Iota-toxin, C3-stau and C3-bot*. The position of co-crystallized waters were compared and four water molecules (*W1-W4*) were consistently found within the NAD$^+$ pocket of all four toxins:

- *W1* interacts with the backbone atoms of Arg303 and is displaced by the carboxamide moiety of NAD$^+$ (see Figure 2.8).

∗ Protocols see Appendix Section A.7.

- *W2* is located inside a hydrophilic region nearby the catalytic centre and possibly interacts with the proximal side chains of Ser345, Tyr382 and Glu387 as well as the hydroxyl groups of NAD^+. Thus, it can be assumed that *W2* is directly involved into ADP-ribosylation mechanisms.

- *W3* is a structural water and stabilizes the NAD^+ binding site by forming hydrogen bonds with Arg302, Asn342. Phe343, Ser345 and one of the phosphate oxygens of NAD^+. Interestingly, it is the only water which was consistently found in many structures of different ADPRTs, including AB-multidomain toxins.

- *W4* might be relevant for NAD^+ binding by forming hydrogen bonds to phosphate oxygens of NAD^+ as well as the sidechain of Asn262.

The importance of each conserved water was further analyzed by calculating interaction potentials of hydrophilic and hydrophobic groups using the GRID approach*[100]. As can be seen from the interaction potential maps shown in Figure 2.8, the NAD^+ pocket of CDTa shows a number of hydrophilic regions and one large hydrophobic area occupied by the nicotinamide moiety of NAD^+. All four waters (*W1-W4*) are located inside hydrophilic regions, thus the results obtained from the GRID analysis are in good agreement with the findings from the crystal structure comparison. Table 2.3 gives an overview of interactions, stability and putative functions of all conserved water molecules.

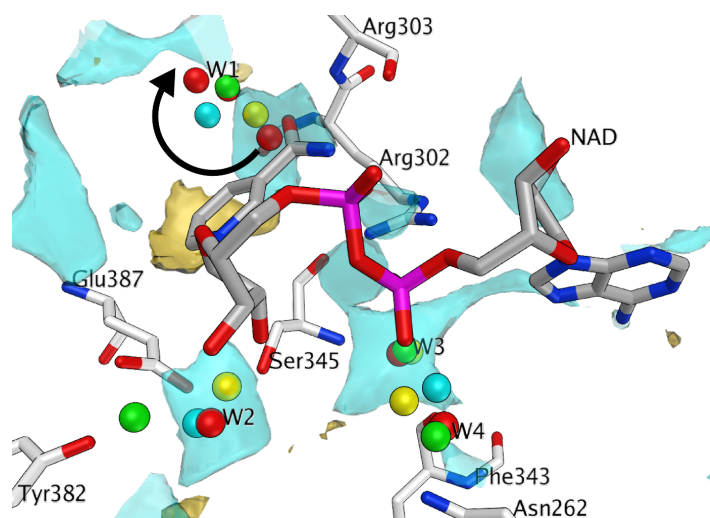**Figure 2.8:** Conserved waters inside the NAD^+ binding sites of CDT (red waters), Iota-toxin (green waters), C3-stau (yellow waters) and C3-bot (blue waters). The interaction potential for hydrophilic and hydrophobic GRID probes are shown as blue and beige surface maps. For both probes, default energy levels were used (OH2: -5.5 kcal/mol; DRY: -2.5 kcal/mol)

---

* Protocols see Appendix Section A.7.

ID	Interacting residues	B-factor	Putative role	Conservation
W1	Arg303	1.26 (4.18)	Structure, NAD^+ binding	AB-binary and single-A toxins
W2	Ser345, Tyr382, Glu387, NAD^+	2.89 (1.43)	Involved in catalysis	AB-binary, single-A and AB_5 toxins
W3	Arg302, Asn342, Phe343, Ser345, NAD^+	0.35 (1.04)	Pocket stabilization, NAD^+ binding	All toxins
W4	Asn262, NAD^+	1.12 (3.65)	NAD^+ binding	AB-binary and single-A toxins

Table 2.3: Conserved waters and their interaction with CDT and NAD^+. The normalized B-factors were averaged over all apo protein structures and NAD^+ bound complexes separately (in brackets).

2.5 Implications for Docking and Virtual Screening

Structure-based virtual screening methods are highly sensitive concerning minimal changes of the protein model, thus the choice of a certain conformation is critical for the success of the molecular docking experiment [101].

As described in Section 2.3.2, the structure of CDTa is relatively stable, especially at the nicotinamide mononucleotide binding site of NAD^+. As long as a small ligand binds inside this conserved pocket, only a few protein conformations need to be included in the docking protocol. However, large ligands or even ligands with novel scaffolds can be affected by the remarkable flexibility observed for the ARTT loop. Therefore, multiple (and different) CDTa conformations need to be included for the docking of large and diverse virtual screening libraries.

Due to their conservation, all four water molecules described in Section 2.4 should be considered in docking or pose refinement protocols. Especially water *W3* should be treated as part of the binding pocket and water *W1* can be used as attractive target for being displaced by polar ligand groups.

Dependent on the specific molecular modeling or virtual screening goal, multiple CDTa conformations and different solvation states should be applied. Furthermore, docking poses nearby conformational variable regions (e.g. the ARTT loop) and/or predicted water locations must be proven carefully.

2.6 Binding Models for NAD^+ Derivatives

Antibody-based assays using etheno-NAD^+ (eNAD$^+$) or 8-pyrrolyl-NAD^+ (pNAD$^+$, see Figure 2.9) were developed to detect ADP-ribosylation of actin catalyzed by CDT [102]. It was shown that both NAD^+ analogs are cofactors of CDT, but their affinity was significantly lower as compared to native NAD^+.
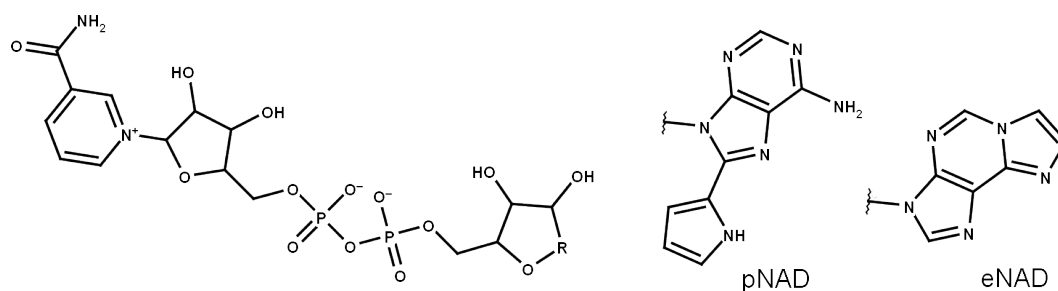
Figure 2.9: Structures of etheno-NAD$^+$ (eNAD$^+$) and 8-pyrrol-NAD$^+$ (pNAD$^+$).

To support these findings by molecular binding models, both analogs were docked to the active site of CDTa*. Due to the structural similarity of NAD$^+$, eNAD$^+$ and pNAD$^+$ as well as their high degree of freedom, docking constraints that were derived from the CDTa-NAD$^+$ complex were applied. Selected docking results were subjected to short MD simulations runs in order to refine the models and to proof the binding stability. The final models obtained from the MD refinement showed an analog pose for eNAD$^+$ and pNAD$^+$ as compared to native binding mode of NAD$^+$. As can be seen from Figures 2.3, 2.10 and 2.11, the interactions between CDTa residues and the nicotinamide mononucleotide moiety was nearly identical for all three cofactors. However, due to the lack of a primary amine group, eNAD$^+$ can not form a second hydrogen bond to Asn342 as it is the case for NAD$^+$ and pNAD$^+$ (compare Figure 2.10 and Figure 2.11).

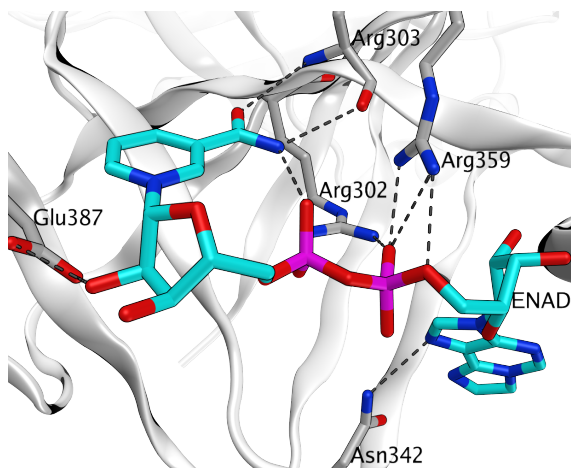**Figure 2.10:** Putative binding mode of etheno-NAD$^+$ (eNAD$^+$) inside CDTa binding pocket. Hydrogen bonds are shown as dashed lines.
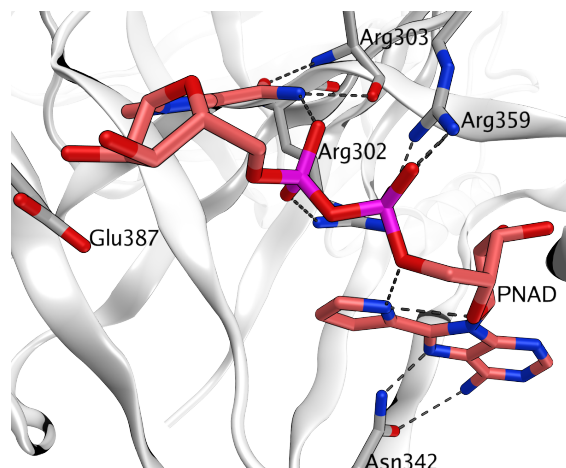

Figure 2.11: Putative binding mode of 8-pyrrol-NAD$^+$ (pNAD$^+$) inside CDTa binding pocket. Hydrogen bonds are shown as dashed lines.

The pyrrole group of pNAD$^+$ formed an intramolecular hydrogen bond to one of

---

∗   Protocols see Appendix Section A.8.1.

adenosine ribose oxygens. This interaction introduce an additional rigidity and might affect the binding conformation of the whole molecule.

To quantify the affinities of NAD^+, $eNAD^+$ and $pNAD^+$ as cofactors of CDTa, binding free energies were approximated from the MD trajectories using the MM-PBSA approach[103]*. As shown in Table 2.4, the obtained interaction energies clearly indicated a favourable affinity for all three cofactors. Consistent with the docking models, the binding energy of $eNAD^+$ was slightly lower than for NAD^+, mainly due to a drop of electrostatic interaction energy. The most favourable affinity was calculated for $pNAD^+$ which resulted from a superior van der Waals interaction energy and a low solvation penalty score.

It can be assumed that the difference in turnover rates observed during *in-vitro* assay tests are not necessarily caused by different cofactor affinities. The speed of the catalytic reaction might be also affected by a slightly different binding conformation (see Figures 2.3, 2.10 and 2.11) which has an influence on the efficiency of the nucleophilic attack.

Cofactor	EEL [kcal/mol]	VDW [kcal/mol]	SOLV [kcal/mol]	TOTAL [kcal/mol]
NAD^+	-227.9 ± 13.2	-54.7 ± 5.3	222.04 ± 10.2	-60.51 ± 6.2
$eNAD^+$	-180.40 ± 14.94	-61.68 ± 4.30	193.98 ± 2.46	-48.10 ± 6.03
$pNAD^+$	-230.57 ± 11.49	-62.13 ± 4.87	209.56 ± 7.95	-83.15 ± 6.05

Table 2.4: Mean and standard deviation of binding energies approximated by the MM-PBSA approach. The total binding energy (TOTAL) is composed of an electrostatic interaction term (EEL), a van der Waals interaction term (VDW) and a solvation free energy term (SOLV).

2.7 Binding Models for Thiobarbiturate Derivatives

Since ADPRTs and Sirtuins share the same cofactor, an *in-house* library of Sirtuin inhibitors was experimentally screened for CDT activity†. Thereby, three compounds containing a thiobarbiturate scaffold were able to inhibit CDT in the µM range of concentration (*ThiBe5-7*, see Figure 2.12 and Table 2.5).

Since thiobarbiturates have been found to inhibit several members of the Sirtuin family‡, it can be assumed that they bind to the common NAD^+ binding site. To get an idea of their putative binding mode, *ThiBe5-7* were docked to an ensemble of different CDTa conformations and several results were proofed for stability by a short MD simulation run§. Interestingly, the Z-isomer of *ThiBe5* and *ThiBe7* was clearly favoured according

---

∗ Protocols see Appendix Section A.8.1.

† Carried out by Dr. Benjamin Maurer, group Prof. Jung, University Freiburg.

‡ See Appendix Table B.3 and the article of Maurer et al.[77].

§ Protocols see Appendix Section A.8.2.

to docking scores, and furthermore, all solutions found for the E-isomer were not stable over the MD simulations[*].

The most stable model of *ThiBe5* showed the thiobarbiturate ring deeply buried inside the NAD^+ pocket of CDT (see Figure 2.13). The amide function formed stable hydrogen bonds with the side chain of Arg303 as well as the backbone of Val351 and displace the loosely bound water *W1*[†], which would lead to a benefit for ligand affinity.

The benzylidene subsituent occupied the NMN binding pocket of CDTa, where it is involved into face-to-face or face-to-edge interactions with the aromatic side chain of Phe356 (see Figure 2.13).
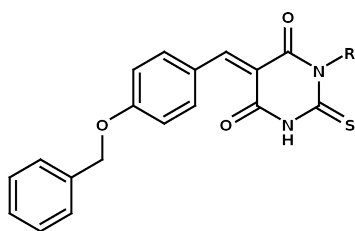

Figure 2.12: Common scaffold of thiobarbiturate inhibitors of CDT.

Name	R	IC_{50} / Inhibition
ThiBe5	Ethyl	56 µM
ThiBe6	H	70% at 150 µM
ThiBe7	Methyl	55 µM

Table 2.5: Inhibition data for thiobarbiturates as determined in the NAD^+ quantification assay.
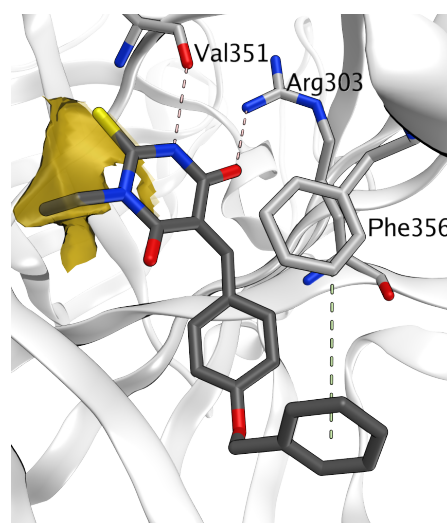
Figure 2.13: Binding model for CDTa and ThiBe5. The interaction potential map for methyl probes is shown as beige surface and hydrogen bonds are highlighted by dashed lines.

As can be seen from the experimental data shown in Table 2.5, a single N-alkylation of the thiobarbiturate ring is tolerated and no significant difference in CDT inhibition was observed for methylated and ethylated derivatives. According to the modeling results, the alkyl groups might bind in an hydrophobic area between the nicotinamide binding pocket and the catalytic glutamate. This model was underlined by an appropriate interaction potential for methyl group probed at this location (see Figure 2.13).

Based on these results, several modification of the compound scaffold are promising: Besides alternative substituents at the thiobarbiturate nitrogen, an adenosine mimicking moeity coupled on the benzylidene group of the *ThiBe* scaffold seems to be adequate to increase the binding affinity. However, according to the docking results, a second

---

[*] See Tables and Plots in Appendix Section A.8.2

[†] See Section 2.4.

N-alkylation of the thiobarbiturate ring seems to be inadequate and might lead to inactive compounds.

2.8 Binding Models for Pyrrolidinedione Derivatives

Besides thiobarbiturate derivatives, compound possessing a pyrrolidinedione moeity were found as novel inhibitors of CDT[102]. Inhibition values were determined for six derivatives (*Pyro1-6*, see Figure 2.14 and Table 2.6), but a clear structure-activity relationship could not be formulated from this data. To support the characterization of pyrrolidinediones as a novel class of CDT inhibitors, binding models were developed during this work.
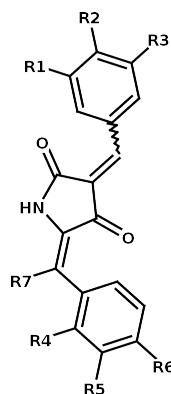

ID	R_1	R_2	R_3	R_4	R_5	R_6	R_7	IC_{50} [µM]
Pyro1	H	NO_2	H	Cl	Cl	H	H	3.1 ± 2.1
Pyro2	H	NO_2	H	Cl	H	H	H	27.5 ± 5.9
Pyro3	H	NO_2	H	H	H	H	H	58.7 ± 5.7
Pyro4	CF_3	H	CF_3	H	H	H	H	12.2 ± 2.8
Pyro5	Br	OH	Br	H	H	NO_2	Br	14.9 ± 14.4
Pyro6	Br	OH	Br	Cl	Cl	H	H	57.4 ± 4.2

Figure 2.14: Scaffold of pyrrolidinedione derivatives.

Table 2.6: Pyrrolidinedione based inhibitors of CDT. The inhibition data was determined in the NAD^+ quantification assay.

Pyro1-6 were docked into an ensemble of different CDTa conformations including all conserved waters described in Section 2.4. Due to the huge amount and diversity of obtained docking solutions, only models with an overrepresented protein-ligand interaction fingerprint were further analyzed by MD simulations*.

However, one binding mode was consistently preferred according to the docking scores and showed superior stability during all simulation runs. This model is exemplarily shown for *Pyro1* in Figure 2.15 and *Pyro5* in Figure 2.16. As can be seen from both Figures, the pyrrolidinedione scaffold was placed in central position inside the NAD^+ pocket of CDTa and a number of interactions with protein residues as well as conserved waters were observed. The pyrrolidinedione carbonyl group interact with the sidechain of Arg359 and the the conserved water *W4*. One of the benzyl subsituents was consistently placed inside the nicotinamide binding pocket, faciliated by hydrophobic interactions with residues of the STS-motif and the aromatic sidechain of Phe356. Depending on the particular subsituents at the benzyl group, further electrostatic

---

∗ Protocols see Appendix Section A.8.3.

interactions were observed - for example with water *W1* (see Figure 2.15) or with ARTT loop residues such as Glu385 (see Figure 2.16).

As indicated by the CDT inhibition values determined for *Pyro1-3* (see Table 2.6), chloro-substituents were clearly preferred at position R_4 and R_5. This might result from a formation of halogen bonds (see Figure 2.15), or due to a considerable hydrophobicity at this part of the CDTa pocket*.
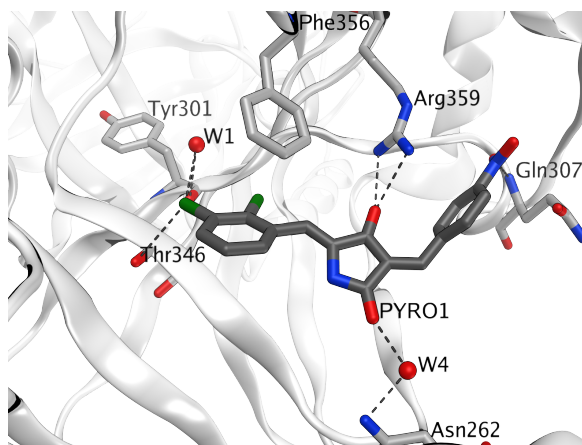

Figure 2.15: Binding model for CDTa and Pyro1. Hydrogen and halogen bonds are drawn as dashed lines.
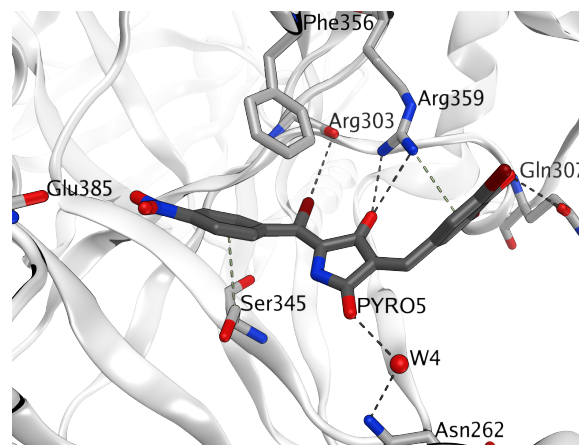
Figure 2.16: Binding model for CDTa and Pyro5. Hydrogen and halogen bonds are drawn as dashed lines.

The second (opposed) benzyl group was mostly docked to the adenosine-ribose pocket of CDTa. Depending on the particular R-groups, hydrophobic interactions as well as hydrogen bonds with the side chain of Gln307 were observed (see Figure 2.16). However, due to the limited amount of experimental data, all presented models of pyrrolidinediones and CDT should be considered as preliminary and must be confirmed by further assay tests.

2.9 Virtual Screening for CDT Inhibitors

While for other NAD^+-dependent enzymes a number of potent and selective inhibitors have been discovered in the last decades[35], much less was reported about small molecule inhibitors of ADPRTs. In the case of CDT, no inhibitor is known until now, that is why this target is interesting for *in-vitro* as well as *in-silico* screening campaigns. During this work, several virtual screenings were carried out and selected compounds were tested for inhibition of CDT activity. In the following sections, two specific virtual screening strategies will be described in detail.

---

* As described for the thiobarbiturate model shown in Figure 2.13.

2.9.1 Nicotinamide Similarity Screening

Most of the PARP inhibitors are based on a benzamide pharmacophore which mimics the interactions of the nicotinamide moiety of natively bound NAD^+ [35]. Their carboxamide group interacts with the highly conserved Arom-H/R motif and their aromatic ring is often bound between the PN-loop and the STS motif* by π- or van-der-Waals interactions.

This binding pattern seems to be conserved across the PARP and ADPRT family [36], that is why a benzamide similarity is a proper strategy to detect novel inhibitors of CDT. Moreover, the nicotinamide binding pocket of CDT exhibits superior conformational stability (see Section 2.3) which is important for the success of a structure-based virtual screening approach.

In order to generate a focussed library of benzamide related compounds, the Asinex database† was filtered by a MACCS-key fingerprint search. 571 compounds showed a sufficient similarity to the benzamide scaffold and were further clustered according to their pairwise fingerprint similarity. 58 diverse compounds were docked to an ensemble of CDTa models and 14 promising molecules were finally ordered from Asinex‡. Six of them (*VS1-VS6*, see Figure 2.17) showed inhibition of CDT activity during subsequent *in-vitro* assay tests (see Table 2.7).
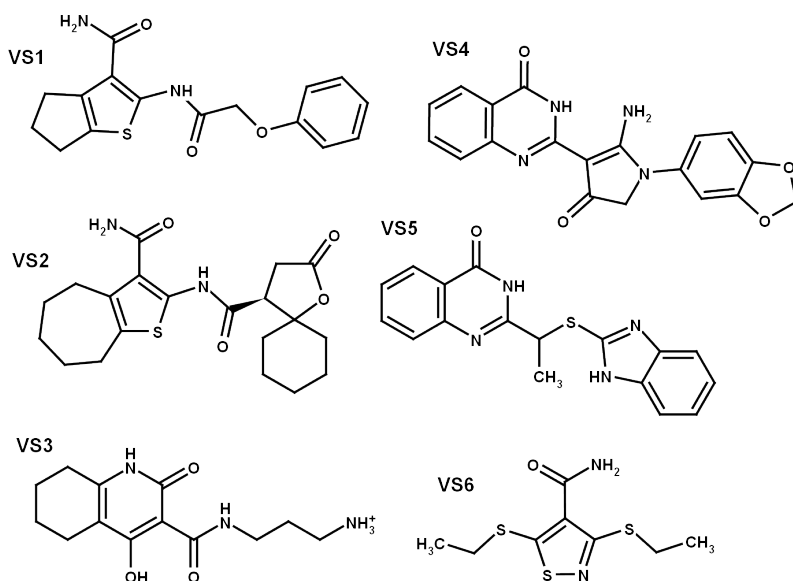
Figure 2.17: Virtual screening hits obtained from the nicotinamide similarity screening.

ID	CDT inhibition
VS1	52% at 125 µM
VS2	50% at 125 µM
VS3	43% at 125 µM
VS4	38% at 125 µM
VS5	35% at 125 µM
VS6	29% at 125 µM

Table 2.7: CDT inhibition by VS1-VS6 measured in a radiolabeled NAD^+ assay.

Putative binding modes obtained from docking are shown for two structural distinct hits

---

∗ Respectively Y-X_{10}-Y motif in DT-like toxins and PARPs.
† Asinex Gold dataset: 205883 diverse and druglike molecules.
‡ Protocols and detailed information on ordered compounds see Appendix Section A.9.1.

(*VS1* and *VS4*) in Figure 2.18 and Figure 2.19. Consistently, the amide function of both compounds interact with the backbone of Arg303, thus mimicking the nicotinamide moiety of native bound NAD$^+$. While the thiophenecarboxamide moiety of *VS1* seems to be optimal to form the desired hydrogen bonds, the pyrimidinone moiety of *VS4* was slightly too bulky for this kind of interaction. According to the docking results, the nicotinamide mimicking heterocycles of *VS1* and *VS4* were perfectly placed between the PN-loop and STS-motif, provided by π-π interactions with the sidechain of Phe356.

The second amide function of *VS1* forms a hydrogen bond with the side chain of Arg302 and/or the conserved water *W3* (see Figure 2.18). Such interactions were not observed for the docking results of *VS4*, mainly due to the formation of two intramolecular hydrogen bonds (see Figure 2.19). The thereby introduced rigidity of *VS4* might be a reason for the suboptimal distance between the pyrimidinone moiety and the backbone oxygen of Arg303. However, additional electrostatic or hydrophobic interactions with CDTa residues are possible for both compounds - for example with the side chain of Arg359 which can adopt various conformations as shown in Section 2.3.2.
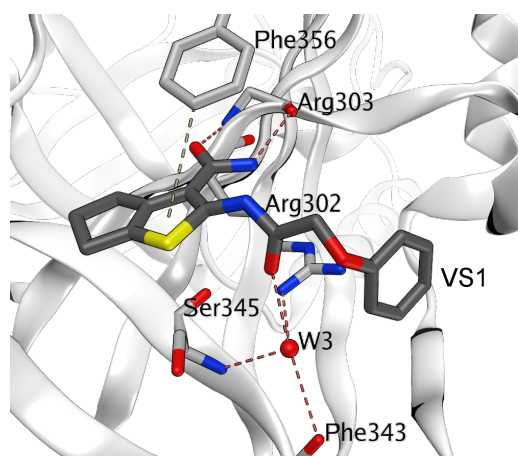
Figure 2.18: Binding model for CDTa and VS1. Hydrogen bonds are highlighted by dashed lines.
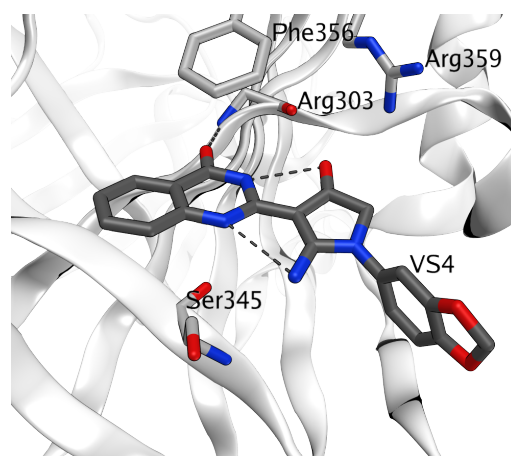
Figure 2.19: Binding model for CDTa and VS4. Hydrogen bonds are highlighted by dashed lines.

It is important to note that the binding models as well as the inhibition values of *VS1-VS6* should be considered as preliminary and have to be confirmed by further experimental tests.

2.9.2 Cholix Inhibitor Analogs

Recently, a number of Cholix-A inhibitors were discovered by an experimental screening of PARP inhibitor libraries[36]. Their binding mode was determined by X-ray crystallography and revealed analogous interactions at the NAD$^+$ pocket as already observed for several PARP structures. As can be seen from the structure of Cholix-A in complex with

the compound *V30* (see Figure 2.21), the inhibitor imide function forms two hydrogen bonds with a glycine residue that usually binds the nicotinamide moeity of NAD^+. The bicyclic aromatic ring interacts with both tyrosine residues that are part of the Y-X_{10}-Y motif.

Because this part of the NAD^+ pocket is highly conserved among PARP and ADPRT enzymes (see Figure 2.21), it can be assumed that related inhibitors are able to interact with CDTa as well[33]. To proof this hypothesis, *V30* was used as template for a similarity based virtual screening experiment. The Chembridge diversity database* was filtered for compounds sharing a similar MACCS key fingerprint as V30 and 182 hits were docked to different models of CDTa†.
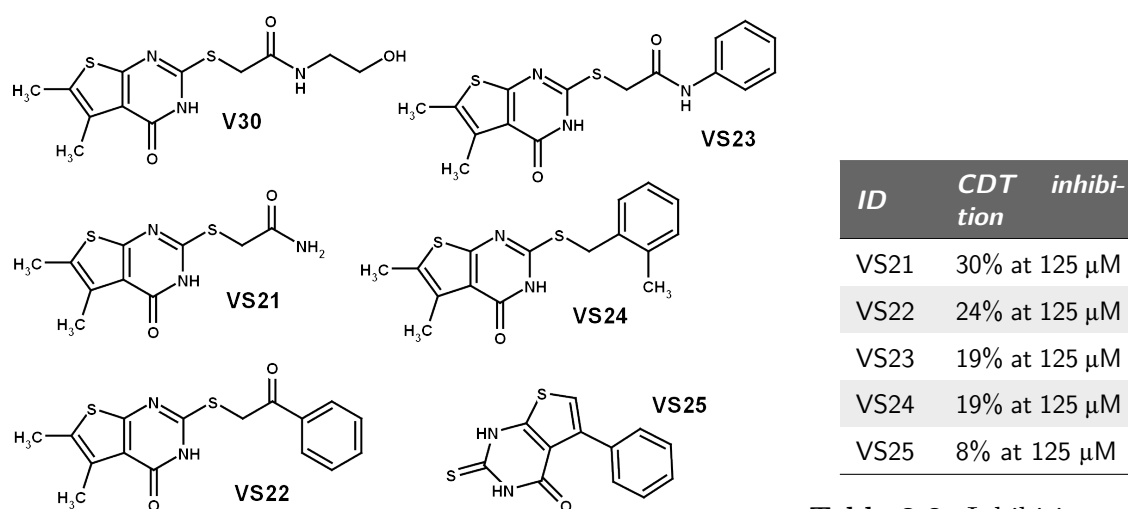
Figure 2.20: Structures of V30-similar virtual screening hits which showed CDT inhibition in *in-vitro* assay tests.

ID	CDT inhibition
VS21	30% at 125 µM
VS22	24% at 125 µM
VS23	19% at 125 µM
VS24	19% at 125 µM
VS25	8% at 125 µM

Table 2.8: Inhibition data for virtual screening hits as determined in the NAD^+ quantification assay.

Ten diverse molecules with high docking scores and plausible binding poses were ordered from Chembridge and tested for activity in the NAD^+ quantification assay‡. However, five of them (*VS21-VS25*, see Figure 2.20) showed weak inhibition of CDT activity at a concentration of 125 µM (see Table 2.8).

A putative binding mode of the most active inhibitor *VS21* is exemplarily shown in Figure 2.22. Consistent with the intitial hypothesis, the bicyclic heteroring of *VS21* might addressed the backbone of Arg303 as well as the aromatic side chain of Phe356. Importantly, both interactions are analog and thus consistent with the binding mode determined for *V30* and Cholix-A (compare Figure 2.21 and Figure 2.22). The methyl groups of *VS21* were well positioned inside a hydrophobic area of the CDTa pocket and the primary amide of *VS21* might interact with the side chain of Arg359. However,

---

*   Chembridge diversity dataset: 50.000 highly diverse compounds.
†   Protocols see Appendix Section A.9.2.
‡   Carried out by Dr. Benjamin Maurer, group Prof. Jung, University Freiburg.

probing different substituents at the amine function might be a promising strategy to optimize the inhibition values for related compounds.
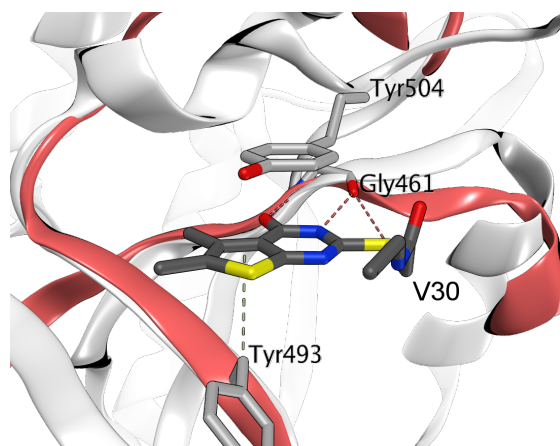

Figure 2.21: Structure of Cholix-A in complex with V30 (grey). The superimposed NAD$^+$ pocket of CDTa is shown in red and hydrogen bonds are drawn as dashed lines.
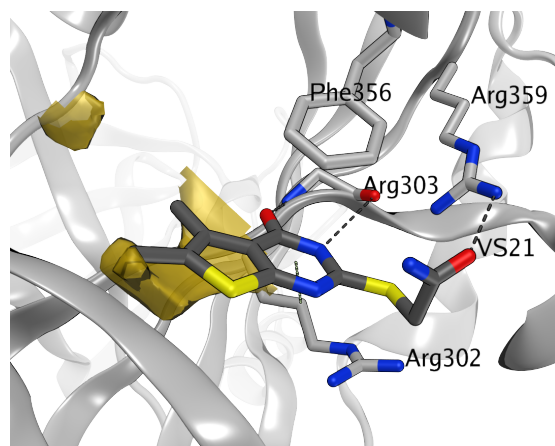

Figure 2.22: Binding mode of VS21 docked to CDTa. The interaction potential map for methyl probes is shown as beige surface and hydrogen bonds are drawn as dashed lines.

In summary, the results of the PARP-inhibitor similarity screening indicated a suitable strategy to find novel inhibitors of CDT. The structural conservation among bacterial ADPRTs and PARPs can be addressed by common inhibitors such as *V30* and analogous compounds.

2.10 Conclusions

The ADP-ribosyltransferase CDT is possibly involved into the pathogenicity of *Clostridium difficile* infections. Due to increasing resistance rates to antibiotic treatments, research focussing on alternative drug approaches, such as CDT specific inhibitors, are of medical relevance.

Within this work, the molecular structure of CDTa was analyzed by computational methods and compared with the structures of several related enzymes. It was clearly shown, that the conformation of NAD$^+$ which is preferred by bacterial toxins is very specific and significantly different from conformations preferred by other NAD$^+$ dependent enzymes. Thus, it is feasible to develop specific inhibitors of bacterial ADPRTs, although they share the same cofactor as many other enzymes such as oxidoreductases or Sirtuins (which are essential for metabolic pathways).

A flexibility analysis carried out by MD simulations revealed, that the buried part of the NAD$^+$ pocket is quite stable and an appropriate target for structure-based virtual screening campaigns. Four conserved waters were detected at this region and they were incorporated into the development of CDT-inhibitor binding models.

However, it became clear that the pocket of CDTa is structurally optimized for NAD^+ and alternative cofactors, such as $eNAD^+$ and $pNAD^+$ lead to a decreased efficiency of the ADP-ribosylation process. These insights were underlined by molecular docking and binding-free-energy calculations, which indicated a drop in electrostatic binding energy due to a loss of a hydrogen bond in the case of $eNAD^+$.

Putative binding models were suggested for thiobarbiturates and pyrrolidinedione derivatives and it was shown, that both types of CDT inhibitors might bind at a conserved and conformationally stable region inside the NAD^+ pocket. Furthermore, conserved waters are potentially involved into the binding process. This leads to the assumption that thiobarbiturates as well as pyrrolidinedione derivatives might be also inhibitors of other bacterial ADPRTs as well as PARPs.

In order to find further novel inhibitors of CDT, several virtual screenings were performed and selected candidates were tested for *in-vitro* inhibition of CDT activity. One of these screenings based on nicotinamide similarity and resulted in six compounds, which showed moderate inhibition within the assay tests. A second approach based on a recently reported Cholix-A and PARP-1 inhibitor (V30): A ligand- and structure-based virtual screening for related compounds resulted in five hits, which showed *in-vitro* inhibition of CDT activity. Thus, the structural relationship between PARPs and ADPRTs is close enough to share common inhibitors, but individual compounds need to be optimized in order to end up with potent and selective molecules.

In summary, the current virtual screening results underlined, that cyclic or coplanar bicyclic amide structures are appropriate scaffolds for CDT inhibitors. The potency and selectivity of the discovered inhibitors needs to be increased, but they provide an appropriate starting point for further optimization rounds. Future *in-vitro* and *in-silico* screenings, as well as crystallographic studies will lead to an increased knowledge on CDT biological function and support the development of novel therapeutical approaches to treat diseases associated with *Clostridium difficile* infections.

CHAPTER 3

Molecular Modeling Studies on Sirtuin 5

3.1 Introduction

Human Sirt5 is a mitochondrial enzyme involved in the regulation of metabolic pathways such as the urea cycle. Sirt5 catalyzes the acylation of CPS1, the first checkpoint of the urea cycle, which is essential for cellular detoxification[53]. It was recently discovered that Sirt5 shows unique enzymatic activity by transfering negatively charged PTMs including malonyl, succinyl and glutaryl groups from modified lysine residues to ADPR[12,52].
Several crystal structures provided valueable insights, how the enzyme recognizes acidic lysine modifcations by showing an two key residues deep inside the substrate binding pocket. Furthermore, these structures are appropriate starting points for structure-based virtual screening (SBVS) campaigns, in order to find novel Sirt5-specific inhibitors.
One of the most important steps in SBVS is a proper analysis of the protein target structure - e.g. in respect to conformational flexibility and pocket solvation states[85,86]. However, past research was mainly focussed on Sirt1-3, thus a detailed description of the structural variability and the role of waters inside the binding pocket was not reported for Sirt5 until now.
Within this chapter, an *in-silico* structure analysis of Sirt5, the development of protein-ligand binding models as well as various SBVS campaigns will be described.

3.2 The Molecular Structure of Sirtuins

A number of Sirtuins were already crystallized*, showing a structurally conserved core of about 260 residues folded in two characteristic domains: A larger Rossmann fold domain, typical for NAD^+ binding proteins, is connected by several loops with a smaller zinc binding domain containing a tetrahedral coordinated zinc ion[60,94]. The zinc binding domain is structurally more diverse among the different Sirtuin types, thus possibly important for the discrimination of isoform specific target substrates. The

---

* Examples see Appendix Sections B.1 and C.1.

variable N- and C-termini may promote substrate recognition, oligomerisation and possibly autoregulation. However, oligomerisation was already observed in a number of Sirtuins crystal structures, thus it seems likely that it plays a role in their structural or biochemical functions[104]. The binding site of NAD$^+$ and the acylated protein lysine residue is located in a large cleft between both domains (see Figure 3.1).
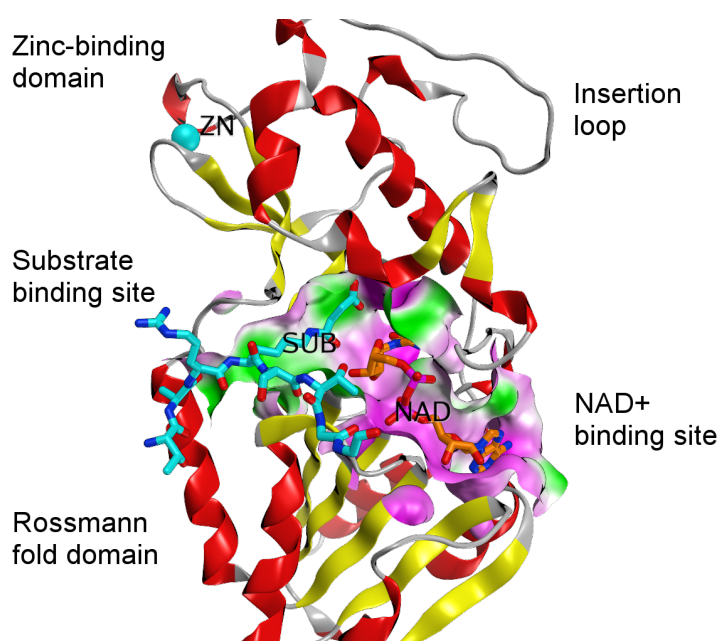
Figure 3.1: The crystal structure of Sirt5 (PDB: 3RIY) shows a typical architecture of Sir2-like proteins. A Rossmann fold domain is connected by several loop with a smaller zinc binding domain. The binding site of NAD$^+$ and the substrate is located in a large cleft between both domains. The pocket surface is colored according hydrophobic (green), hydrophilic (pink) and neutral (white) regions.

3.2.1 The NAD$^+$ Binding Site

The NAD$^+$ pocket of Sirtuins contains several invariant amino acids which are directly involved in cofactor binding and catalytical mechanisms*. As illustrated in Figure 3.2, this region can be divided into three pockets namely the A-, B- and C-site[60].
The adenosine ribose (AR) moiety of NAD$^+$ binds to the A-site by forming two conserved hydrogen bonds: One between the amide and a conserved glutamate (Glu64)† and a second between the hydroxyl of the adenosine ribose and a conserved asparagine (Asn275). Additional hydrophobic interactions between NAD$^+$ and a number of glycine residues (Gly60, Gly249) also contributes to cofactor binding.
The nicotinamide-ribose (NR) moiety of NAD$^+$ binds to the B-site by forming hydrogen

---

$*$ See also sequence alignment in Figure 4.1.

$†$ Sirt5 numbering is used in this chapter.

bonds between the hydroxyl groups and an invariant glutamine (Gln140) as well as asparagine (Asn141) residue. The proximal histidine (His158) recognizes the 3'-OH group of NR and activates the 2'-OH group for subsequent nucleophilic attack (see Section 1.3.4)[105].

In the absence of the substrate, NAD^+ binds in a non-productive conformation, showing the nicotinamide (NAM) group nearby the lysine binding site. However, substrate binding induces a number of conformational changes and leads to a movement of the NAM moiety towards the C-site. The productive conformation of NAD^+ is stabilized by hydrogen bonds between the carboxamide of the NAM moiety and the sidechain of a conserved aspartate (Asp143) as well as the backbone of an isoleucine (Ile142) residue (see Figure 3.2). Additional hydrophobic interactions with an invariant GAG motif (Gly58, Ala59, Gly60) forcing NAD^+ in a strained conformation, which is neccessary for the catalytic process.
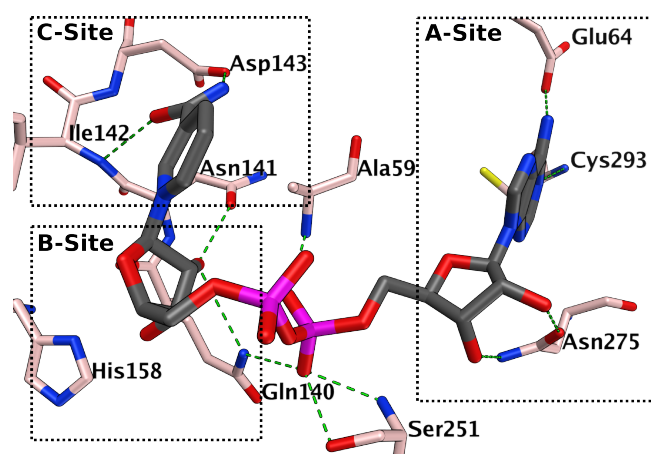
Figure 3.2: The NAD^+ pocket of Sirtuins can be divided into three subpockets. The AR moiety of NAD^+ binds to the A-site, the NR moiety of NAD^+ binds to the B-site and the NAM moiety of the productive NAD^+ conformation binds to the C-site.

3.2.2 The Cofactor Binding Loop

The C-site of Sirtuins is partially formed by the conformationally dynamic cofactor binding loop (CB-loop)*, a crucial structural component for NAD^+ binding, catalysis and product release[60].

Thereby, a conserved phenylalanine (Phe70) seems to play a central role: Initially, this residue is involved in NAD^+ binding by forming π-π-interactions with the NAM moiety. After NAD^+ cleavage and subsequent rearrangment of the CB-loop, the same phenylalanine protects the intermediate imidate against hydrolysis and a base-exchange reaction[106]. Because CB-loop residues highly influence the pocket characteristic of Sirtuins, their conformational dynamic if further analyzed in Section 3.3.5.1.

---

* Sirt5 residues 66 to 81.

3.2.3 The Substrate Binding Site

The acylated protein lysine residue binds in a hydrophobic cleft, formed by both domains and one of the connecting loops (see Figure 3.1). The lysine Nε forms a hydrogen bond to the backbone of a conserved valine (Val221), which adjusts the carbonyl oxygen for the nucleophilic attack on productive bound NAD$^+$ (see Figure 3.3).

It was shown that Sirtuins have only a limited specificity concerning their substrate sequence and possibly interactions outside the catalytic cleft might be important for a specific recognition[107]. However, the first N-terminal residue of the acylated lysine might be critical, possibly due to an interaction with a conserved glutamic acid (Glu225), which mediates a signal to the zinc-binding domain[108].

Interestingly, the region where the acyl group of the substrate lysine binds (acyl-pocket), shows a remarkable sequence variation within the Sirtuin family*. This variation might be the reason, why some Sirtuins deacylate other lysine modifications apart from an acetyl group.
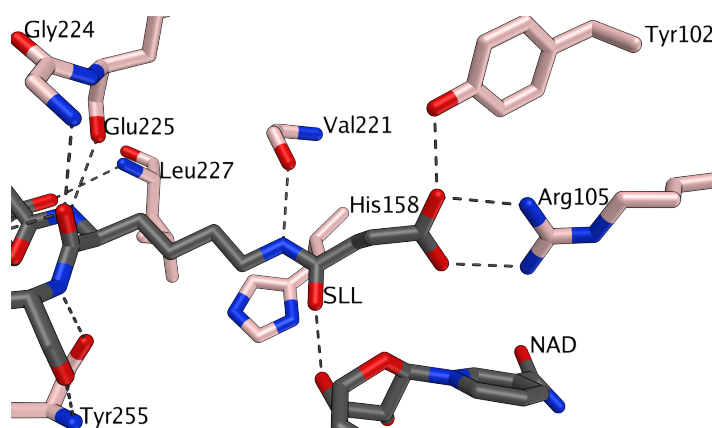
Figure 3.3: The substrate pocket of Sirt5 shows a number of conserved residues such as Val221 and the catalytic His158. Both, Tyr102 and Arg105 are specific for Sirt5 and critical for binding negatively charged succinylated lysine residues (SLL). Hydrogen bonds are drawn as dashed lines.

3.2.4 Structural Characteristics of Sirt5

Despite the conserved overall fold, each Sirtuin shows a number of unique structural features, which are relevant for their functional divergence. For example, Sirtuins that are efficient deacetylases (Sirt1-3), show a number of bulky hydrophobic residues which form the acyl-pocket. One of these residues (Sirt3: Phe180) is substituted to a smaller residues in Sirt4-5 (Sirt4: Ile90; Sirt5: Ala86) or even not present in Sirt6-7†.

---

* See sequence alignment in Section 4.
† See sequence alignment in Section 4.

Furthermore, one helix* that forms the backside of the acyl-pocket, shows a significant sequence variability within the Sirtuin family. In the case of Sirt5, this helix includes a tyrosine (Tyr102) and arginine (Arg105) residue, which specifically bind negatively charged lysine modifications (see Figure 3.3).

Sirt5 residues	Motif	Function	Conservation
G58, A59, G60	GAG motif	Binding of NA moiety of NAD$^+$	Invariant
N275		Binding of AR of moiety of NAD$^+$	Invariant
H158		Catalysis	Invariant
Residues 64-80	CB-loop	NAD$^+$ binding and catalytic mechanisms	Conserved
Q140, N141, I142, D143	(C-site)	Binding of productive NAD$^+$	Conserved
V221, F223, G224, E225		Binding of substrate lysine	Conserved
Residues 249-254		Binding of NAD$^+$ and substrate	Conserved
R217		Binding interaction between both domains	Conserved
Y102, R105	Y/R motif	Binding of acidic lysine modifcations	Sirt5 specific
A86		Acyl-pocket opening	Sirt5 specific
Residues 175-200	Insertion-loop	unknown	Sirt5 specific

Table 3.1: An overview of invariant, conserved and specific residues, forming the binding cleft of Sirt5.

Despite this unique Tyr102/Arg105 (Y/R) motif, Sirt5 contains an additional loop region [†], which was not observed for other human Sirtuin structures so far[109]. This *Insertion-loop* interacts with the flexible CB-loop and the α5-helix by forming different hydrogen bonds depending conformational state of the protein. The role of this loop is not clear until now, but a contribution protein-protein interactions, oligomerisation or the catalytic process might be possible.
Table 3.1 summarizes important residues and structurally conserved regions, forming the binding site of Sirt5.

3.3 Conformational Analysis of Sirt5

It is well known, that Sirtuins undergoes a number of conformational changes upon substrate binding and that the CB-loop plays an emergent role for maintaining protein structure and function[110,111]. However, most of the published Sirt5 structures are complexed with succinylated substrates and/or the cofactor (NAD$^+$, Carba-NAD$^+$or ADPR), thus the structural data is limited and and biased towards productive conforma-

---

*   α5-helix, residues 95 to 109.
†   *Insertion-loop*, residue 175-200, see Figure 3.1.

tions of the protein. Because the choice of certain protein conformations highly influence the outcome of structure-based virtual screening experiments, the conformational space of Sirt5 was closely analyzed by means of Molecular Dynamics (MD) simulation studies.

3.3.1 Conformational Sampling of Sirt5 Structures

Due to limited time scales and high energy barriers, conventional MD (cMD) simulations are usually not able to explore the whole conformational space of a protein[112]. To overcome this problem, accelerated MD (aMD) simulations were carried out during this work[113]. The choice for aMD simulations (and not alternative techniques such as replica-exchange) had several practical reasons: First, the method is computational efficient* and simple to parameterize† and second, it was recently implemented for graphics processing units (GPUs) within the Amber Software package[114].

The structure of Sirt5 in complex with NAD^+ and succinylated peptide (PDB: 3RIY) served as initial structure for four independent MD simulations. A 75 nanosecond simulation was carried out for the complete complex, both by the conventional as well as accelerated MD approach (*cMD-holo* and *aMD-holo*). Additionally, both ligands were removed and analog simulations were repeated for the unbound structure of Sirt5 (*cMD-apo* and *aMD-apo*). The latter simulations were carried out in order to sample apo-like conformations of the protein, which are not crystallized for Sirt5 until now. Detailed protocols for all four simulations can be found in the Appendix Section B.3.

3.3.2 Overall Structural Flexibility

Temperature factors (B-factors) obtained from X-ray crystallography are a standard measure of atomic motion and positional disorder. Analog informations can be extracted from MD trajectories by calculating the mean square fluctuation of the atoms relative to their average position[115]. To analyze the conformational flexibility of Sirt5, B-factors profiles were calculated from both accelerated MD simulations and compared with experimental determined values‡.

As can be seen in Figure 3.4, the estimated B-factors agreed well with the averaged values obtained from crystallographic refinement, thus support a sufficient accuracy of the simulated motions. In general, the B-factor-profile revealed areas of both, low and high flexibility, similar as described for other protein binding sites[116].

---

* Only a single system needs to be simulated
† Does not require additional knowledge, e.g. on the energy landscape.
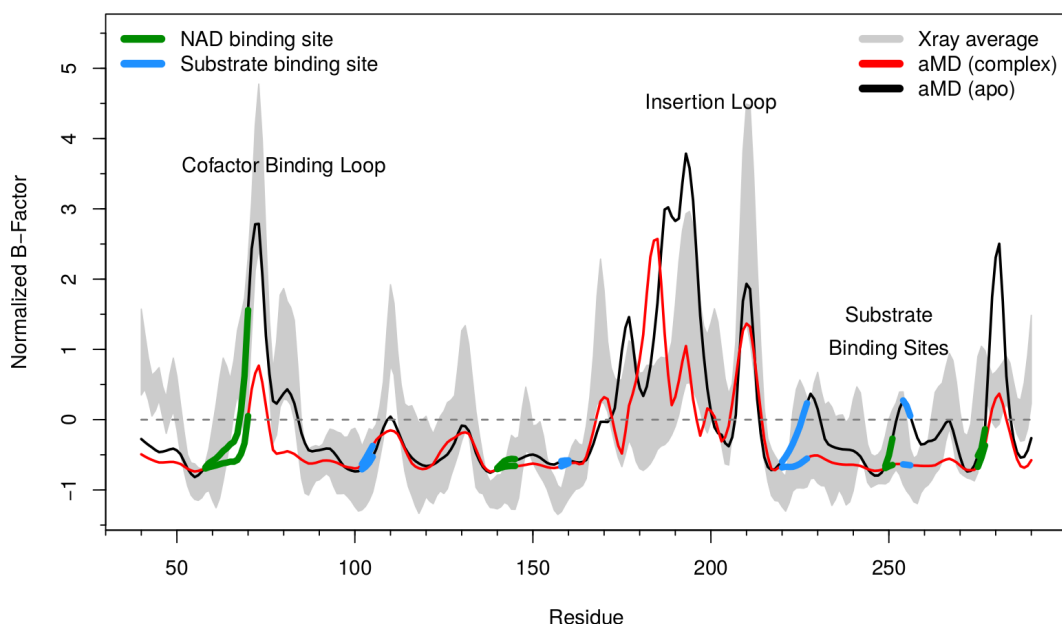‡ Protocols see Appendix Section B.3.1.

Figure 3.4: The B-factor profile of Sirt5 illustrates the average experimentally determined B-factor (gray) and computationally determined values (black and red) obtained from accelerated MD simulations. All B-factors are normalized, thus values below zero indicate an above-average stability and values higher than zero are a sign of structural flexibility.

Due to a stabilization by protein-ligand interactions, several residues of the CB-loop and the substrate binding site showed only a significant flexibility in the case of the unbound simulation. However, the Sirt5 *Insertion-loop* showed remarkable fluctuations during both simulations, but no cooperative effect with CB-Loop residues or other parts of the protein was detected*. Thus the functional role of this Sirt5-specific element remains an open question.

3.3.3 Conformational Space Analysis

It has been found that most of the motions observed during a MD simulation can be described by a few number of modes obtained from a principle components analysis (PCA) of the trajectory [117]. In order to study the conformational space explored by all four Sirt5 simulations, a PCA was performed on the *aMD-apo* trajectory and all conformations obtained from the other simulations, as well as selected crystal structures, were projected on the first two eigenvectors†.

∗ Cooperative effects were analyzed by a calculation of the correlation matrix from both aMD simulation.

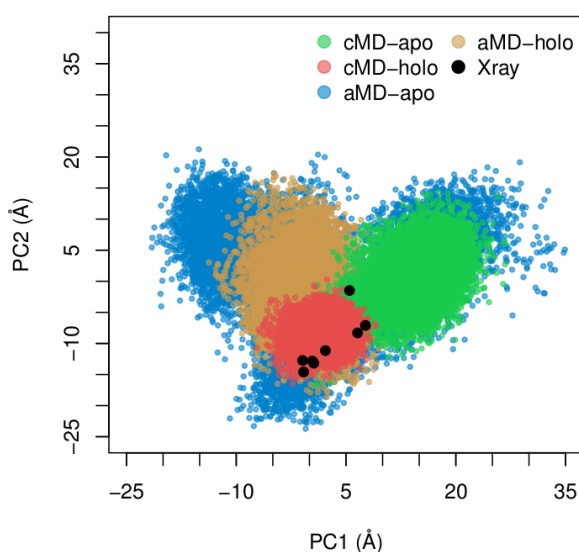† Protocols see Appendix Section B.3.2.

Figure 3.5: A PCA of the *aMD-apo* trajectory (blue) and the projection of sampled conformations, as well as experimentally determined structures (black), illustrates the conformational space of Sirt5.
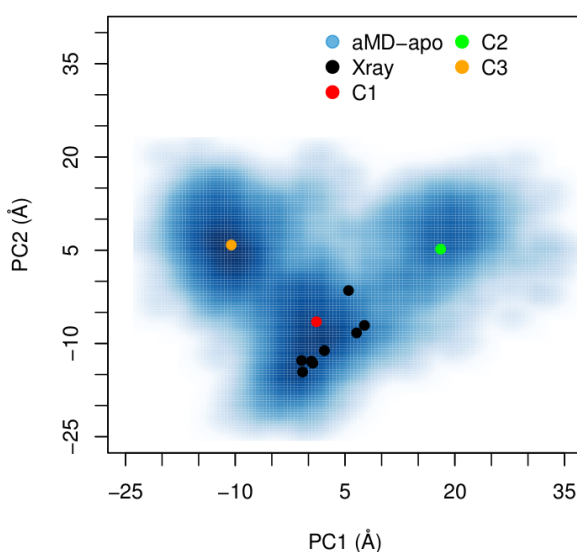

Figure 3.6: The density plot of *aMD-apo* conformations illustrates three regions within the PCA space. The projected representatives from hierarchical clustering (C1-C3) support the existence of three distinct conformations of Sirt5.

The PCA plot shown in Figure 3.5 clearly indicates an enhanced conformational sampling for the aMD simulations. While the *cMD-holo* simulation explores only a local vicinity nearby the crystal structures, both aMD simulations explored additional regions within the PCA space. The removal of both ligands (NAD$^+$ and peptide) lead to a decreased strain on the protein and allowed the transition to a conformational subspace that was not accessible during the substrate bound simulations of Sirt5. According to the density plot shown in Figure 3.6, all conformations sampled during the *aMD-apo* simulation can be divided into three highly populated clusters. Lower densities observed between these subspaces indicate a considerable energy barrier, that is why a full transition was only sampled during the aMD-apo simulation of Sirt5.

To identify Sirt5 structures which represent each cluster, a hierarchical clustering was done for the *aMD-apo* trajectory*. As shown in Figure 3.6, three cluster representatives (*C1-C3*) were projected nearby the cluster centers indicated by the PCA density plot. However, a structural comparison between these conformations revealed a number of interesting differences:

C1 is similar to the closed (productive) conformation as observed in nearly all crystal structures of Sirt5 (Cα-RMSD of 2.87 Å between *C1* and PDB 3RIY). Consistently, the corresponding cluster was mainly sampled during the *aMD-holo* simulation, but only in 1.9% of the snapshots obtained from the *aMD-apo* trajectory.

∗ Protocols see Appendix Section B.3.3.

C2 was observed for 21.3% of the *aMD-apo* trajectory and showed a more open (apo-like) conformation of Sirt5. In agreement with that, no similar structure was sampled during the whole *aMD-holo* simulation (see Figure 3.5).

C3 was exclusively observed during the *aMD-apo* simulation. The structure is characterized by a CB-loop conformation that close the acyl-pocket and permits the accessibility of the Y/R motif. However, such a conformation was not experimentally observed until now.

In respect to the diversity of the structures sampled during the *aMD-apo* simulation, it is likely that a number Sirt5 conformations exists which are significant different to all crystal structures resolved until now. Nevertheless, such conformations might be relevant for enzyme inhibition, especially for inhibitors that are structurally distinct to the co-crystallized substrates and NAD$^+$. Totally new models, such as observed for the cluster representative *C3*, indicate a putative inhibitory role of the CB-loop similar to autoinhibition mechanisms described for other enzymes like kinases[118].

3.3.4 A Putative Apo Conformation of Sirt5

Crystallographic studies on Sir2-like enzymes revealed a transition from an open (unbound) to a closed (substrate bound) conformation of the protein[111,119]. However, such structural information is not available for Sirt5, due to a lack of unbound crystal structures. Because an open conformation might be relevant for small molecule binding, two representative models obtained from MD simulations (*C2-C3*, see Section 3.3.3) were superimposed with apo structures of homologous human as well as bacterial Sirtuins*.

It was found that the *in-silico* conformation *C2* showed a high similarity with two of the closest apo approximations of Sirt5:

1) A Sirt5-ADPR-HEPES complex (PDB: 2B4Y) was superimposed with a backbone RMSD of 0.99 Å.

2) An apo structure of Sir2-TM (PDB: 2H2I) was superimposed with a backbone RMSD of 1.99 Å.

As can be seen in Figure 3.7, *C2* has a typical apo conformation which is characterized by a more open binding cleft as compared to the substrate bound form.
Thus, a transition from the initially closed structure to an open conformation happened during the *aMD-apo* simulation. To detect the opening process, the interdomain angle (α) between the Rossmann-fold domain and the Zinc-binding domain was calculated for each snapshot extracted from the trajectory and compared with angles calculated for Sir2-TM apo and holo structures (PDB: 2H2I and 1YC5)†.

∗   Protocols see Appendix Section B.3.4.
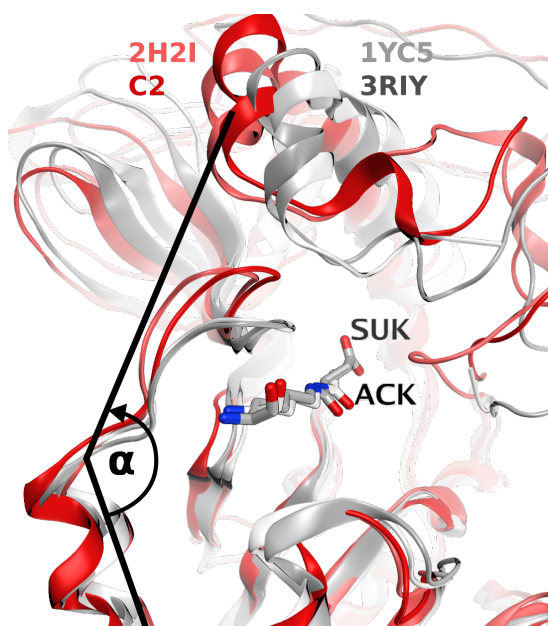†   Protocols see Appendix Section B.3.5.

Figure 3.7: Open (red) and closed (grey) conformation of the Sirt5 homolog Sir2-TM. The Sirt5 model *C2* showed a high overlap to the apo structure of Sir2-TM, as calculated by the interdomain angle (α).
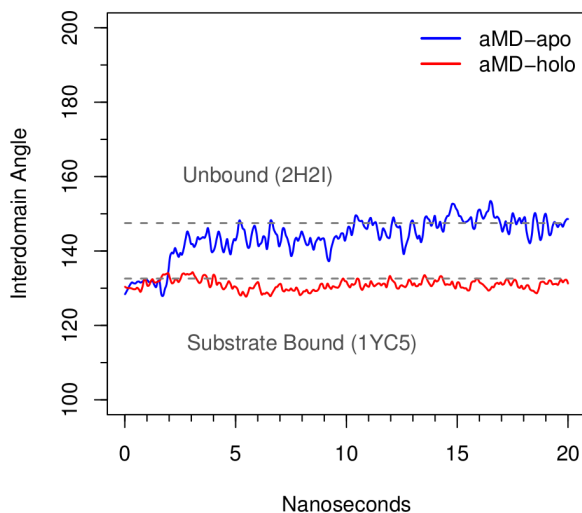
Figure 3.8: An interdomain angle analysis of the *aMD-apo* trajectory revealed a binding cleft opening after 2 ns. The equilibrated αvalue was similar to the interdomain angles observed for the apo structure of Sir2-TM.

As can be seen in Figure 3.8, the protein stayed in a closed conformation during the first two nanoseconds of the aMD simulation (α ≈ 130°). Starting at two nanoseconds, a transition to an open conformation (α ≈ 158°) occured, which was stablized after 15 ns until the end of the simulation. In the case of the substrate-bound simulation (*aMD-holo*), the closed conformation of Sirt5 was stabilized by the bound ligands and a transition was not detected within the whole trajectory (see Figure 3.8).

3.3.5 Flexibility at Binding Cleft

Most of the A- and B-pocket residues of Sirt5 did not show significant variability concerning their sidechain orientations, neither in the X-ray structures nor during conventional MD simulations. The highest flexibility proximal to the active site was observed for residues forming the CB-loop and the Sirt5 unique *Insertion-loop* (see Figure 3.4). Their influence on the binding site characteristic will be discussed in the following sections.

3.3.5.1 CB-Loop Flexibility and Pocket Conformations

The cofactor binding loop of Sirtuins is highly flexible (see Figure 3.4) and determines the characteristic of the NAD$^+$ binding site, especially the size and accessibility of the

C-pocket and neighboring regions. This can be easily shown for Sirtuins where holo- and apo-structures were resolved (e.g. for Sir2-TM, Sirt2 and Sirt3).

Also three Sirt5 conformation gained from a clustering of the *aMD-apo* trajectory*, revealed significant differences in shape and electrostatic properties of the inner binding pocket. As can be seen from a pocket comparison of the substrate-bound (*C1*, see Figure 3.9) and unbound conformation of Sirt5 (*C2*, see Figure 3.10), a hydrophobic extension of the *classical* C-pocket was observed for the latter model, due to an alternative conformation of the CB-loop as well as Arg105. However, such regions of the Sirt5 binding cleft might be only accessible in the absence of the substrate, or at least in the absence of a succinylated lysine residue that interacts with Arg105. Interestingly, this region is formed by a number of non-conserved residues and can be addressed by Sirt5-specific inhibitors.
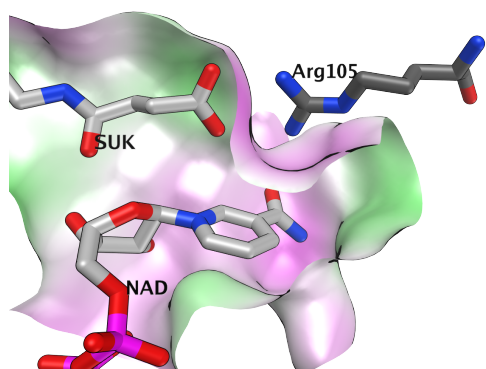
Figure 3.9: Structure Sirt5 in complex with a succinylated lysine (SUK) and NAD$^+$. The pocket surface is colored according hydrophobic (green), hydrophilic (pink) and neutral (white) regions.
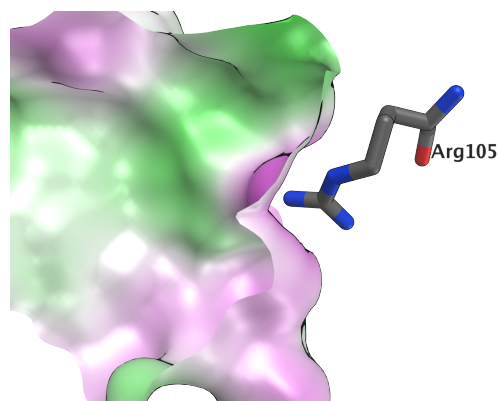
Figure 3.10: An apo model revealed different physicochemical properties of the Sirt5 pocket. The surface is colored according hydrophobic (green), hydrophilic (pink) and neutral (white) regions.

3.3.5.2 Flexibility of Arg105

Arg105 is a Sirt5-specific residue involved in the binding of acidic lysine modification and is possibly crucial for an efficient catalysis[52]. To address this residue by a proper chemical moiety, is a promising strategy to end up with Sirt5-specific inhibitors. In preparation for structure-based virtual screening experiments, the mobility of Arg105 was analyzed in detail.

In nearly all published structures of Sirt5, Arg105 is involved into a binding of the acylated lysine residue and thereby restricted to a conformation (*conf-1*) that enables the formation of a salt bridge (see Figures 3.3 and 3.9). However, two crystal structures without such an interacting ligand group (PDB: 3RIG and 2NYR), revealed an

---

* *C1-C3*, see Section 3.3.3.

alternative rotation of the Arg105 side chain in the direction to the C-pocket (*conf-2*). To study which conformation might be preferred, a dihedral analysis of both *cMD* trajectories was carried out*. As shown in Figure 3.11, Arg105 adopts a conformation similar to *conf-1* (3RIY) during the whole *cMD-holo* simulation. Thus, the succinylated lysine of the peptide restrained Arg105 to this specific conformation to retain the necessary saltbridge.

In contrast, other Arg105 conformations were preferred during the unbound simulation of Sirt5 (see Figure 3.11). Interestingly, these rotamers were nearly identical to *conf-2*, the alternative Arg105 conformation as observed in two Sirt5 crystal structures. As shown in Figure 3.10, the side chain of Arg105 in conformation *conf-2* points inside the C-Pocket and occupies the space for nicotinamide binding.
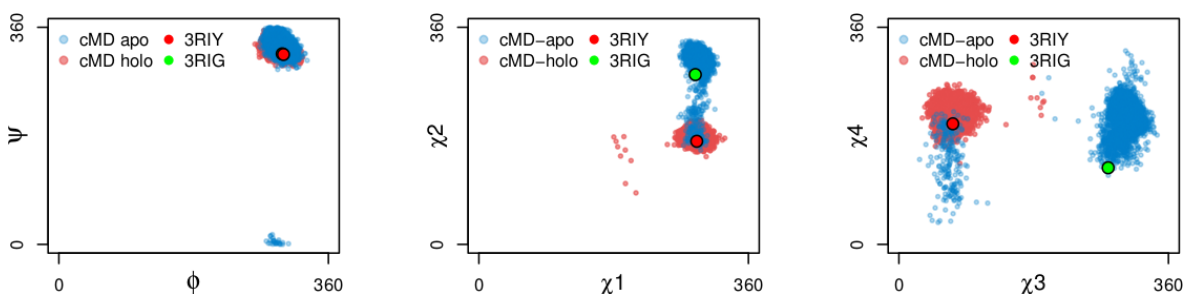
Figure 3.11: Torsion angle distributions of Arg105 during the substrate-bound (*cMD-holo*) and unbound (*cMD-apo*) simulation of Sirt5. Depending on the state, at least two distinguishable rotamers may exist (*conf-1* and *conf-2*). This is underlined by the torsion angles observed for two representative crystal structures of Sirt5 (PDB: 3RIY and 3RIG).

3.4 Solvent Analysis at Sirt5 Binding Site

Water contributes to protein structure and is frequently involved in non-covalent binding processes such as protein-ligand complexation[99]. Therefore, a proper knowledge of water locations at protein binding sites is crucial for the development of reliable protein-ligand models and the prediction of binding affinities[120].

Critical water molecules can be identified by crystallographic evidence or predicted by computational methods such as the three-dimensional reference interaction site model (3D-RISM)[121]. In the following sections, 3D-RISM calculations were performed on selected structures of Sirt5 and the results were compared with conserved waters found in several Sirtuin crystal structures.

---

* Protocols see Appendix Section B.3.6.

3.4.1 Conserved Waters in the Sirt5-Substrate Complex

It was assumed that important waters are conserved in different crystal structures of Sirt5, but also among crystal structures of homologous Sirtuins[99]. In order to detect conserved waters, a number of Sirtuin structures were superimposed and the positions of co-crystallized solvent molecules were compared*.

Seven waters were consistently found in different crystal structures of Sirt1-3 and Sirt5-6 (see Table 3.2). However, due to the lack of sufficient electron density, it is often not possible to resolve all relevant waters within a crystal structure. This leads to a certain degree of inconsistency between the single structures, making it difficult to decide which water molecule is really important.

ID	Interacting Residues	B-factor	ΔG_{pred} [kcal/mol]	Putative role	Conservation
W1	G60, E64, C293, NAD$^+$	22.8	-2.68	Structure, NAD$^+$ binding	High
W2	Q140, T250, V254	32.3	-2.61	Structure	High
W3	A59, V67, P68, NAD$^+$	23.3	-3.03	Structure, NAD$^+$ binding	High
W4	H158, Y255	22.8	-2.70	Structure	High
W5	Q140, N141, I142, suK, NAD$^+$	19.5	-2.76	NAD$^+$ binding, substrate binding	Weak
W6	R105, NAD$^+$	32.0	-2.44	NAD$^+$ binding	Weak
W7	R71, S251, NAD$^+$	20.55	-2.73	NAD$^+$ binding	Weak

Table 3.2: Seven water molecules consistently found in crystal structures of different Sirtuins. Their binding energy was approximated by the radial distribution function obtained from 3D-RISM.

Alternative computational approaches, such as the 3D-RISM method, describes pocket hydration by spatial distributions which characterize the organization of solvent molecules around a solute[121]. Such distributions can be calculated from unsolvated protein structures and provide information on existence and locations of single water molecules as well as an estimation of their binding affinity.

To confirm the seven conserved waters found by the crystal structure comparison, a 3D-RISM analysis was carried out for the substrate bound structure of Sirt5†. The

---

* Protocols see Appendix Section B.4.1.
† Protocols see Appendix Section B.4.2.

continuous solvent distribution was translated into explicit water locations using the recently developed algorithm *Placevent*[122]. As can be seen in Figure 3.12, the positions of the predicted waters nicely coincide with the conserved waters found in crystal structures (mean positional error of 0.55Å ± 0.42Å). Thus, the solvent distributions were correctly reproduced and the 3D-RISM approach seems to be adequate to predict additional (non-resolved) waters or even pocket hydration in computationally determined protein models.

3.4.2 Predicted Waters in the Apo Model of Sirt5

To predict the hydration of a substrate unbound Sirt5, 3D-RISM calculations were carried out for the apo-like conformation of Sirt5 which was obtained from accelerated MD simulations (*C2*, see Section 3.3.4). A comparison of waters found in the substrate-bound complex of Sirt5 with waters placed inside the binding site of *C2*, revealed some notable differences. As can be seen in Figure 3.12, additional (stable) waters were predicted inside the C-pocket, as well as the substrate-lysine binding site of *C2*. It seems likely, that both regions of the Sirt5 binding cleft are filled with weakly bound waters which are displaced upon substrate and NAD+ binding. In agreement with that, other Sirtuin crystal structures without co-crystallized NAD+ show extensive water networks inside the C-pocket ranging from the weakly conserved water *W6* to the absolutely conserved water *W1*.
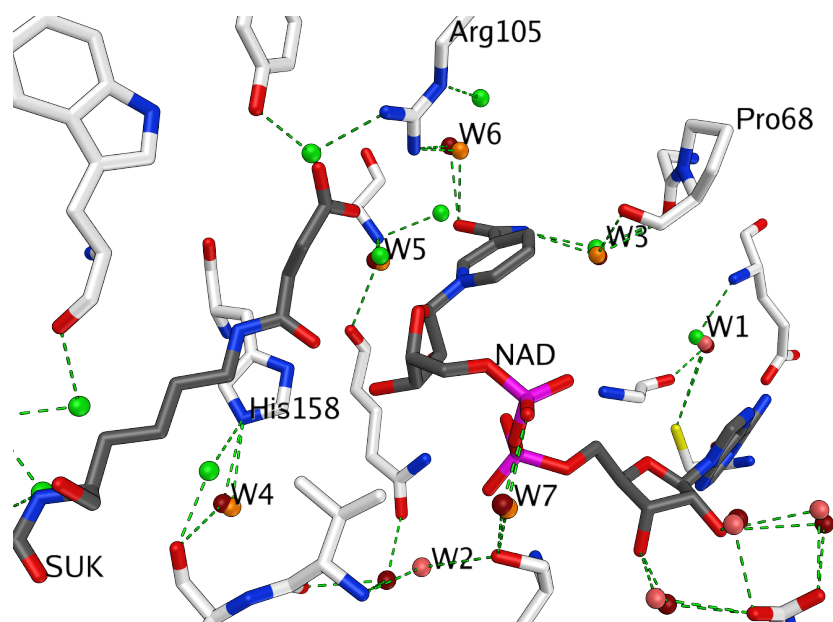

Figure 3.12: Structure of Sirt5-substrate complex (white) superimposed with conserved waters found in several Sirtuin crystal structures (brown), waters predicted from 3D-RISM (orange) and waters predicted for the apo-model of Sirt5 (green). Hydrogen bonds between water molecules and protein residues are drawn by dashed lines.

Interestingly, several water molecules (*W1* and *W3-W6*) were detected in both models, underlining their putative role in stabilizing the structure of the Sirt5 binding cleft. One conserved water (*W2*) was not predicted for the apo-model (*C2*) due to a conformational change of the substrate binding site at this location. This reflects the structural variability within this region that was also observed in the B-factor profile shown in Figure 3.4.

3.4.3 Putative Roles of Seven Conserved Water Molecules

The solvent analysis described in Sections 3.4.1 and 3.4.2 clearly indentified seven conserved water molecules inside the binding cleft of Sirt5. A putative role for each of these waters will be suggested as follows:

- *W1* and *W2* are likely structural waters part of the A- and the B-pocket of Sirt5 (and other Sirtuin isoforms)

- *W3* might stabilize the productive complex of Sirt5, by establishing a hydrogen bond between the nicotinamide moiety of NAD^+ and conserved CB-loop residues (Pro68).

- *W4* possibly stabilizes the sidechain of His158 in the right orientation for the catalytic process.

- *W5* might be relevant for substrate binding, by forming hydrogen bonds between several highly conserved residues, the succinylated lysine as well as NAD^+.

- *W6* could be Sirt5-specific, by bridging hydrogen bond interaction between Arg105 and the nicotinamide moiety of NAD^+.

- *W7* seems to be involved in NAD^+ binding, by bridging hydrogen bonds between the phosphate groups and CB-Loop, as well as A- and B-pocket residues.

3.5 Implications for Docking and Virtual Screening

Currently available crystal structures of Sirt5 are biased towards substrate-bound conformations which are not necessarily conformations used by small molecule inhibitors. However, it was shown that some key residues of the binding cleft are highly flexibile, including CB-loop residues and the Sirt5-specific Arg105 (see Section 3.3). Because such a mobility is critical for structure-based virtual screening (SBVS), it is necessary to incorporate different Sirt5 models within docking and SBVS experiments.

Furthermore, it has been clarified that a number of water molecules stabilize the binding cleft and might contribute to ligand binding as well as the catalytic reaction (see Section 3.4). Some of these waters seems not easily displaceable by ligands and should be considered as a part of the protein structure. Other (more weakly bound) waters might

be displaceable and can be targeted by proper chemical groups in order to gain binding affinity for Sirt5 inhibitors.

However, SBVS methods, such as protein-ligand docking, are highly sensitive concerning minimal changes in the receptor representation - thus, a proper handling of the target structure variability is crucial[101]. The simultaneous usage of multiple protein models is one strategy to incorporate pocket flexibility and different solvation models into one docking experiment. Such an ensemble of protein structures reduce the risk of selecting a non-optimal single structure for virtual screening campaigns[123]. Hence, a small and diverse set of Sirt5 models was used for docking and virtual screening experiments carried out in this work. Insights gained from the flexibility and solvation analysis were incorporated into the choice of structural ensemble. However, due to the considerable flexibility observed for CB-loop residues and the lack of evaluation datasets, there was still an uncertainty if the structures were optimally chosen.

3.6 Binding Models for CPS1-based Peptides

Besides succinylated peptides, other modifications of lysine might bind to the active site of Sirt5. To answer this question, the lysine side chain of a CPS1 derived peptide was systematically modified with a number of different chemical groups[67]. All peptides were measured in an HPLC activity assay* and some of them were further characterized by X-ray crystallisation studies on *Danio rerio* (zebrafish) Sirt5 (zSirt5)[†].

Within this work, a number of CPS1-based peptides were analyzed by computational techniques, in order to predict their molecular interactions with Sirt5 and to support the development of novel derivatives. The chemical structures of these peptides can be found in Section B.5.1 and the data obtained from kinetic measurements is shown in Table 3.3.

3.6.1 Probing of Different Acidic Lysine Modifications

As already described, Sirt5 cleaves succinylated and glutarylated peptides more efficient than malonylated substrates. This effect is mainly k_{cat} driven, as both variants showed comparable K_M values in the HPLC activity assay (see Table 3.3).

---

* Carried out by Theresa Nowak, group of Prof. Mike Schutkowski, University Halle-Wittenberg. Details on HPLC assay see Appendix Section B.2.2.

† Carried out by Martin Pannek, group of Prof. Clemens Steegborn, University Bayreuth.

ID	Lys modification	K_M (µM)	K_{cat} (s^{-1})	K_{cat}/K_M	K_i (µM)
CP1	Oxalyl	415.8 ± 24.3	$1.6 \times 10^{-3} \pm 8 \times 10^{-5}$	4	-
CP2	Malonyl	5.1 ± 1.1	$1.9 \times 10^{-2} \pm 1 \times 10^{-3}$	3758	-
CP3	Succinyl	3.8 ± 0.6	$5.3 \times 10^{-2} \pm 2 \times 10^{-3}$	13995	-
CP4	Glutaryl	4.1 ± 1.0	$7.7 \times 10^{-2} \pm 2 \times 10^{-3}$	18699	-
CP5	Adipoyl	6.5 ± 1.6	$1.0 \times 10^{-2} \pm 6 \times 10^{-4}$	1538	-
CP6	Pimeloyl	80.5 ± 22.9	$2.8 \times 10^{-4} \pm 4 \times 10^{-5}$	4	-
CP7	Suberoyl	409.1 ± 283.0	$5.3 \times 10^{-4} \pm 2 \times 10^{-5}$	1	-
CP8	3,3-dimethylsuccinyl	5.3 ± 1.0	$2.2 \times 10^{-4} \pm 8 \times 10^{-6}$	42	-
CP9	3-phenylsuccinyl	-	-	-	100.0 ± 0.45
CP10	3S-Z-aminosuccinyl	-	-	-	38.1 ± 0.63

Table 3.3: Kinetic data for different CPS1-based peptide derivatives and Sirt5.

Binding models of malonylated (*CP2*) and succinylated (*CP3*) peptides, obtained from molecular docking to Sirt5, revealed a number of possible reasons for the different efficiency of both substrates*. Both peptides bind with their carboxyl function to the Y/R-motif of Sirt5, but the shorter acyl chain of *CP2* results in a slightly different localization of the peptide amide bond. As shown in Figure 3.13, the carbonyl of *CP2* is more distant to the C1 atom of NAD^+, which might explain the lower turnover rate. An elongation of the acyl chain leads to glutarylated (*CP4*) or adipoylated (*CP5*) peptides, which showed similar interactions in zSirt5 crystal structures as compared to *CP3* [67].
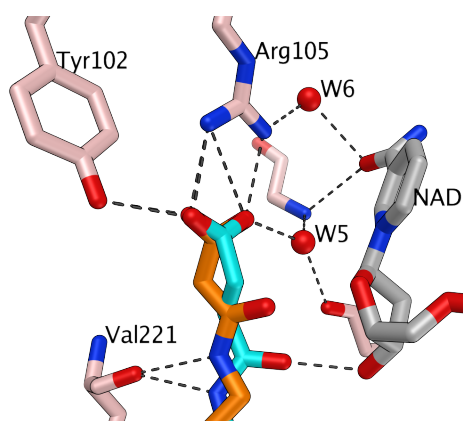

Figure 3.13: Binding model for CP2 (orange) and CP3 (blue) at Sirt5 binding site. Hydrogen bonds are drawn as dashed lines.
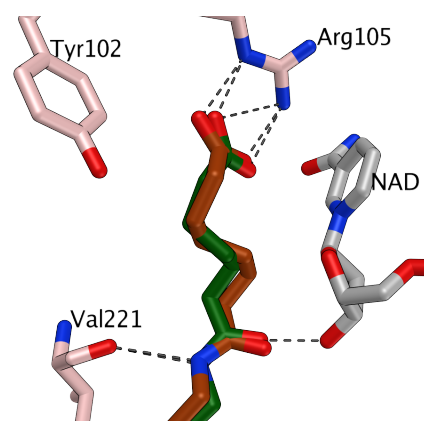

Figure 3.14: Binding model for CP5 (green) and CP6 (brown) at Sirt5 binding site. Hydrogen bonds are drawn as dashed lines.

---

* Protocols see Appendix Section B.5.2.

However, longer acyl modification of the lysine side chain, such as pimeloyl (*CP6*) or suberoyl (*CP7*) groups, are still substrates of Sirt5 but their binding mode was not determined by X-ray crystallography.

Molecular docking of *CP6* and *CP7* to an ensemble of Sirt5 conformations, including different Arg105 rotamers, gave a binding hypothesis for both peptides*. As can be seen from Figure 3.14, both peptides required the alternative conformation of Arg105 (*conf-2*, see Section 3.3.5) which increased the space, sufficient for longer acyl modifications. The loss of the hydrogen bond to Tyr102 and a possibly non-optimal positioning of the peptide carbonyl group, appear to be the reasons for the higher K_M and lower k_{cat} values determined in the HPLC experiments.

Interestingly, an oxalylated derivative (*CP1*) leads to a significant drop in K_M, as compared to the succinylated substrate (*CP3*). Modeling of *CP1* and Sirt5 clearly showed, that the distance between the carboxyl group and the Y/R-motif is too large for hydrogen bond or salt bridge interactions (see Figure 3.15). Additionally, the oxalyl group was very close to the backbone carbonyl of Val221 which might contribute to a K_M penalty compared to the native substrate.
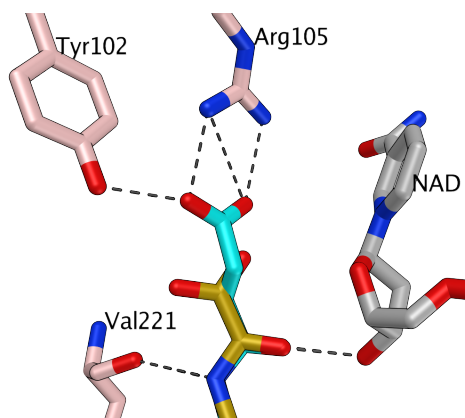
Figure 3.15: Binding model for CP1 (orange) and CP3 (blue) at Sirt5 pocket. Hydrogen bonds are drawn as dashed lines.
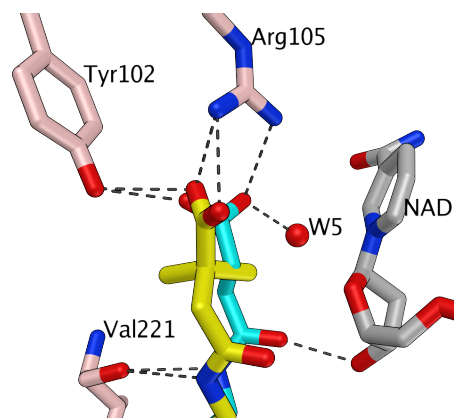
Figure 3.16: Binding model for CP8 (yellow) and CP3 (blue) at Sirt5 pocket. Hydrogen bonds are drawn as dashed lines.

Introducing two methyl substituents at position 3 of the lysine-succinyl group, did not affect the K_M value of the resulting substrate (*CP8*). Consistently, molecular docking showed a similar binding mode for *CP8* and *CP3*, where both methyl groups were placed inside a weak lipophilic region (see Figure 3.16). However, the methyl groups lead to a non-optimal position of the carbonyl groups which might explain the significant lower k_{cat} values measured for *CP8*.

In summary, the length of the lysine acyl modification, as well as the orientation of the

---

* Protocols see Appendix Section B.5.2.

NAD^+ attacking carbonyl group has a strong influence on the catalytic efficiency of the peptidic Sirt5 substrate.

3.6.2 CPS1-based Peptidic Inhibitors

Modifications at position 3 of the lysine succinyl group, enables the development of Sirt5 selective inhibitors[67]. This was underlined by a crystal structure of zSirt5 in complex with a 3-phenylsuccinyl peptide (*CP9*, see Figure 3.17). The phenyl substituent points towards the Sirtuin C-pocket, which is promising for further optimization studies on CPS1-derived inhibitors.

Based on this structure, a number of *CP9* derivatives were generated and computationally probed by means of docking and binding pose refinements*. Especially halogen substituted phenyl or benzyl moieties at position 3 of succinylated peptides were interesting candidates to explore the C-pocket of Sirt5. As can be seen in Figure 3.17, a 3-meta-chlorophenyl or even a 3-para-chlorobenzyl substituted succinyllysine would allow additional hydrophobic or halogen bond interactions inside the C-pocket of Sirt5. A crystal structure obtained for zSirt5 and a 3S-Z-aminosuccinylated CPS1-based peptide (*CP10*, see Figure 3.18) revealed the aromatic ring of the succinyllysine modification in nearly the same position that is observed for the nicotinamide moiety of NAD^+ [67]. Subsequent dockings of *CP10*-based derivatives containing nicotinamide similar moieties, showed that a phenylethylamine moiety with a carboxamide group at meta position would nicely mimic the conserved interactions of productive bound NAD^+ (see Figure 3.18)†.
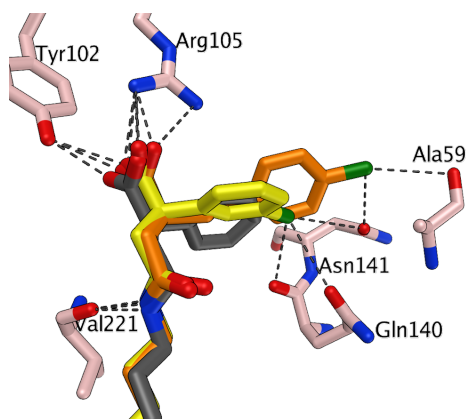

Figure 3.17: Structure of Sirt5 in complex with CP9 (gray, PDB: 4UTV). Two derivatives (orange and yellow) were proposed by molecular modeling studies.
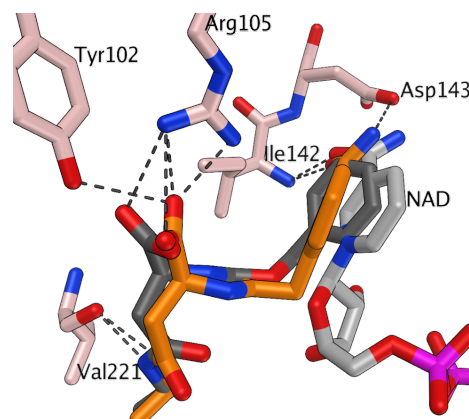

Figure 3.18: Structure of Sirt5 in complex with CP10 (gray, PDB: 4UUA). A derivative was proposed as optimized inhibitor (orange).

---

* Protocols see Appendix Section B.5.3.
† Protocols see Appendix Section B.5.3.

However, synthesis and assay tests of proposed peptide derivatives would be the next step to proof the hypotheses obtained from molecular modeling.

3.7 Binding Models for Thiobarbiturate Derivatives

A number of inhouse compounds were screened for Sirt5 activity, using a fluorescence-based *in-vitro* assay and Z-Lys(succ)-AMC as artificial substrate[*]. Thereby, compounds containing a thiobarbiturate scaffold were found as novel inhibitors of Sirt5[77]. Moreover, two of the most potent derivatives (*ThiFu5* and *ThiFu13*, see Table B.3) showed a furylidene substructure.
In order to characterize this class of inhibitors, virtual compound libraries from Chembridge, Princeton and Asinex were screened for molecules containing a furylidene-substituted thiobarbiturate scaffold[†]. A SMARTS[‡] based pattern search and visual selection of diverse hits resulted in 13 compounds which were ordered and experimentally tested at University Freiburg[§]. However, 11 molecules showed significant inhibition of Sirt5 activity and four of them belong to the most potent small molecule inhibitors reported until now. To get an idea of putative interactions between Sirt5 and thiobarbiturate compounds, a binding mode was predicted by means of docking and MD simulations.

3.7.1 Dataset of Compounds

In total, 35 (thio)barbiturate derivatives[¶] showed significant inhibition of Sirt5 desuccinylation activity[102]. Based on their chemical structure, the dataset can be divided into three main scaffolds:

S1: Furylidene-substituted thiobarbiturates showed the highest inhibition of Sirt5 with a median IC$_{50}$ value of 4.3 µM.

S2: Benzylidene-substituted thiobarbiturates showed moderate inhibition of Sirt5 with a median IC$_{50}$ value of 19.3 µM.

S3: Indolylidene-substituted thiobarbiturates were only weak inhibitors of Sirt5 with a median IC$_{50}$ value of 46.5 µM.

The structure of all three scaffolds as well as the most potent derivatives (both from class *S1*) are shown in Figure 3.19. However, four thiobarbiturates showed other scaffolds and only moderate to weak inhibition of Sirt5 (see inhibition data in Table B.3).

---

*   Details on assay see Appendix Section B.2.1.
†   Protocols see Appendix Section B.6.1.
‡   Smiles arbitrary target specification[124]
§   Dr. Benjamin Maurer, group of Prof. Manfred Jung, University Freiburg.
¶   Full list of compounds see Appendix Section B.6.2.

It is important to note, that nearly all tested thiobarbiturates were also inhibitors of Sirt1-3, thus they act as general Sirtuin inhibitors. Nevertheless, *ThiFu1* and *ThiFu2* are the most potent small molecule inhibitors reported for Sirt5 until now, that is why they serve as valueable tools for structure-based molecular modeling and virtual screeening studies. In the following section, a consistent binding mode of *ThiFu1* and *ThiFu2* will be suggested for Sirt1-3 as well as Sirt5.
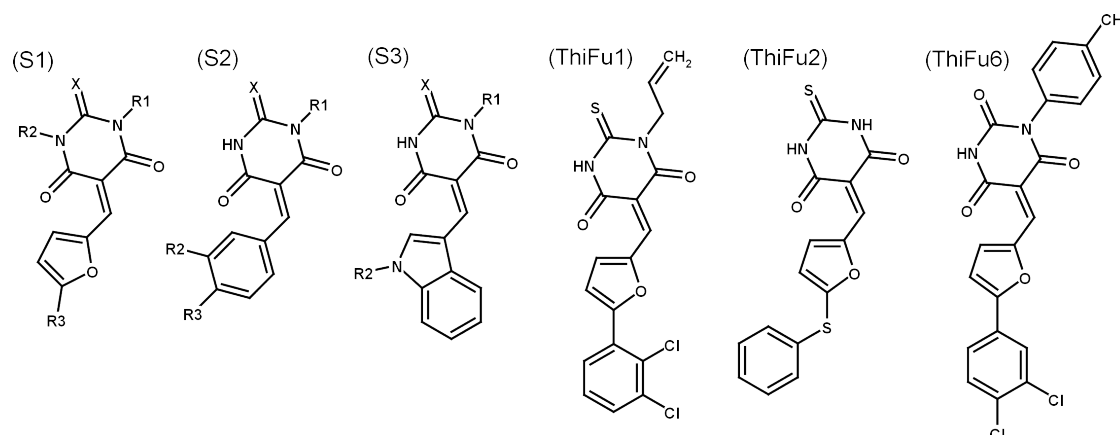
Figure 3.19: The dataset of thiobarbiturate inhibitors consists of the three main scaffolds *S1-S3*. *ThiFu1*, *ThiFu2* and *ThiFu6* were used to generate binding models for Sirt5.

Compound	IC_{50} Sirt1	IC_{50} Sirt2	IC_{50} Sirt3	IC_{50} Sirt5
ThiFu1	5.3 µM	9.7 µM	n.d.	2.3 µM
ThiFu2	3.8 µM	3.5 µM	14.6 µM	2.8 µM
S1 derivatives	n.d.	n.d.	n.d.	2.3 - 29.3 µM
S2 derivatives	9.2 - 50.5 µM	3.4 - 14.7 µM	39.3 - 121.0 µM	6.2 - 67.2 µM
S3 derivatives	n.d.	n.d.	n.d.	16.2 - 65.9 µM
Other derivatives	n.d.	n.d.	n.d.	16.2 - 55.9 µM

Table 3.4: Inhibition values for thiobarbiturate derivatives. The complete set of compounds was only tested for Sirt5.

3.7.2 Predicted Binding Mode

Due to the remarkable size of the Sirtuin binding cleft[*] and the large amount of interactions sites for the thiobarbiturate scaffold, docking constraints are necessary to guide the conformational search process. The constraints used for the docking studies,

---

∗ Approximately 1300 Å^3.

based on three assumptions emerged from the experimental test results:

1. Thiobarbiturates are also inhibitors of CDTa activity (see Section 2.7) - thus they bind to the NAD$^+$ binding site

2. Thiobarbiturates inhibit Sirt1-3 as well as Sirt5 - thus they bind to a conserved region within the Sirtuin binding cleft

3. Alkylation of both thiobarbiturate nitrogens leads to inactive compounds - thus at least one nitrogen is crucial for binding

As can be seen from multiple sequence alignments (Figure 4.1), the B- and C-pocket are the regions with the highest sequence conservation among the Sirtuin family. Therefore, the most potent Sirt5 inhibitor, with comparable inhibition of Sirt1-3 (*ThiFu2*), was intensively docked to region covering the B- and C-pocket of Sirt5*.
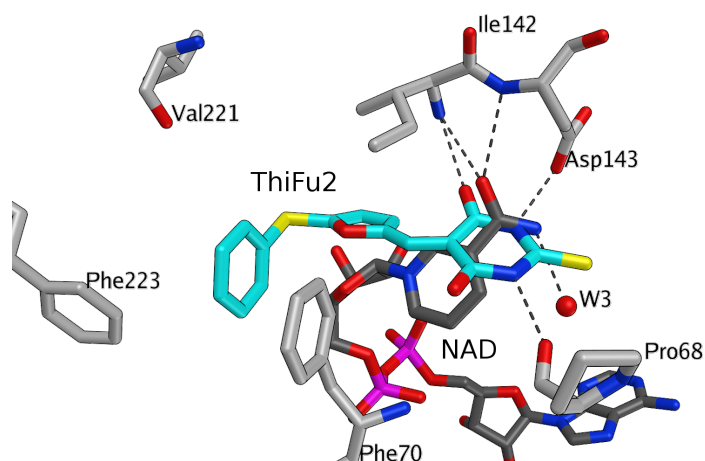
Figure 3.20: Binding model of *ThiFu2* (cyan), superimposed with the structure of Sirt5 in complex with NAD$^+$ (gray). The thiobarbiturate scaffold mimics the binding mode of nicotinamide inside the C-pocket of Sirt5. Hydrogen bonds are drawn as dashed lines.

Several docking models were refined by energy minimization and proofed for stability by a 15 nanosecond MD simulation run. Interestingly, the most stable model showed a similar binding mode as described for CDTa, where the thiobarbiturate ring mimics the native binding mode of nicotinamide (see Section 2.7). As can be seen in Figure 3.20, the thiobarbiturate ring interacts by hydrogen bonds with the backbone of Pro68, Ile142 and the side chain of Asp143. The furylidene group of *ThiFu2* was placed inside the B-pocket, similar to the nicotinamide-ribose group of productive bound NAD$^+$.

To proof this hypothesis on other human Sirtuins, analog dockings of *ThiFu2* were carried out on several protein structures of Sirt1-3[†]. Ensemble dockings and pose

---

∗ Protocols see Appendix Section B.6.3.

† Protocols see Appendix Section B.6.4.

refinements lead to similar binding models as described for Sirt5 (see Figure 3.21 (B-D)). Interestingly, all involved protein residues are strongly conserved, which might explain why thiobarbiturates are inhibitors of all human Sirtuin tested so far.
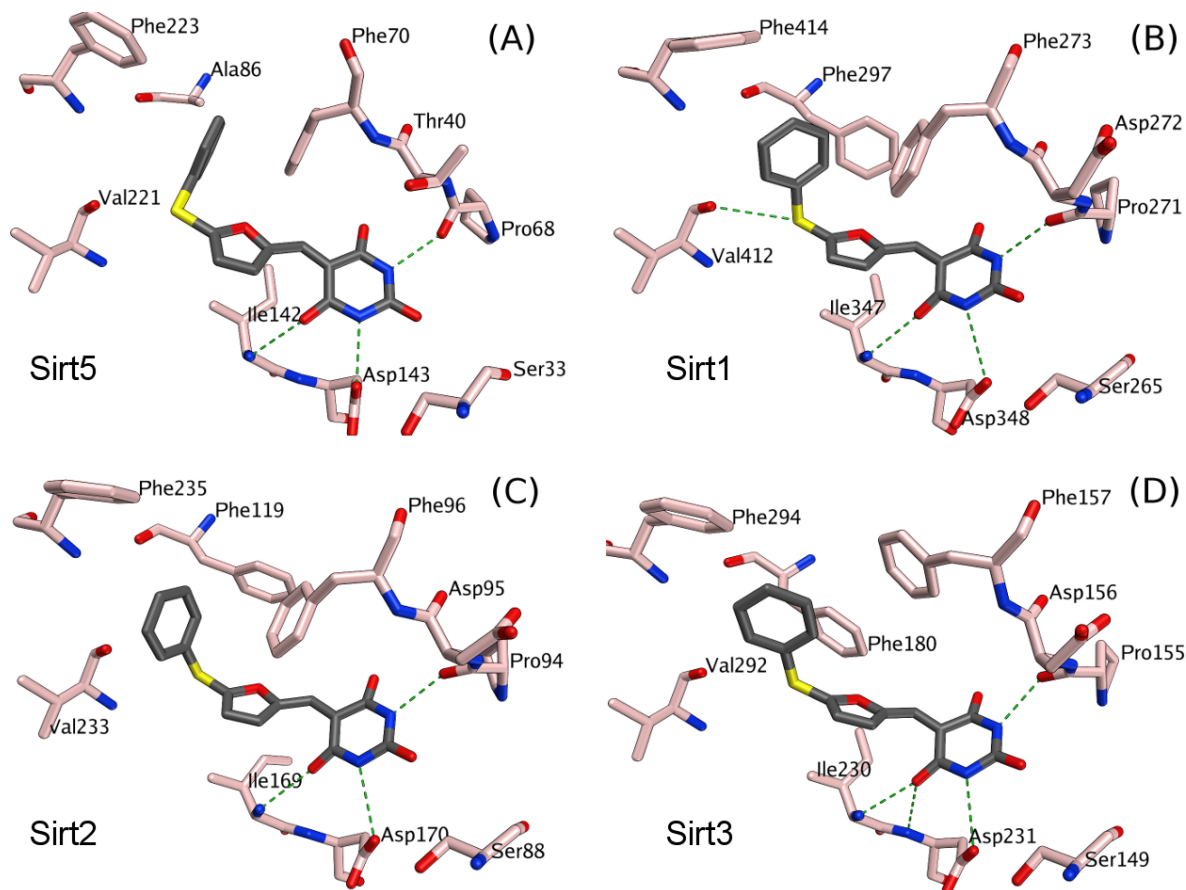
Figure 3.21: A consistent binding mode of *ThiFu2* was found for Sirt5 (A), Sirt1 (B) Sirt2 (C) and Sirt3 (D). Hydrogen bonds are drawn as dashed lines.

The model further indicates a NAD^+ and substrate competitive binding mode, which is consistent with preliminary kinetic data gained from assay experiments at University Freiburg[*]. The binding hypothesis was further proofed for the 33 remaining compounds of the thiobarbiturate dataset. However, analogous poses were obtained for 21 compounds, in fact all derivatives without substituents at the thiobarbiturate nitrogen atoms.

∗ Unpublished data

3.7.3 N-alkylated Thiobarbiturates

The thiobarbiturate *ThiFu1* (see Figure 3.19) and 13 other compounds of the dataset were alkylated at one of the thiobarbiturate nitrogens. However, using the same Sirt5 conformation as for non-alkylated thiobarbiturates, a similar docking pose was not obtainable for alkylated derivatives, due to a sterical hinderance caused by Arg105 and proximal CB-loop residues. Because these residues were shown to be the most flexible components of the Sirt5 binding pocket*, an ensemble of different Sirt5 conformations was incorporated into the docking of alkylated thiobarbiturates.

Two potent alkylated (thio)barbiturates (*ThiFu1* and *ThiFu6*, see Figure 3.19) were chosen for extensive pose sampling and several docking results were subjected to MD simulations in order to proof their stability and to refine the binding poses[†]. Finally, the model shown in Figure 3.22 was sufficient stable for both N-alkylated (thio)barbiturates.
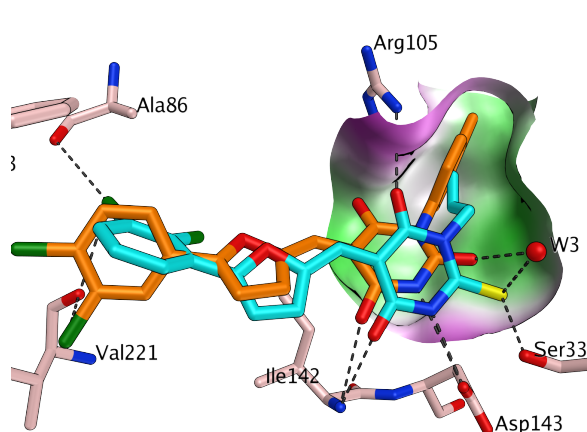
Figure 3.22: The binding models of *ThiFu1* (cyan) and *ThiFu6* (orange) showed several hydrogen bonds interactions (dashed lines) inside the C-Pocket of Sirt5. The Sirt5-specific Arg105 might be involved in binding.
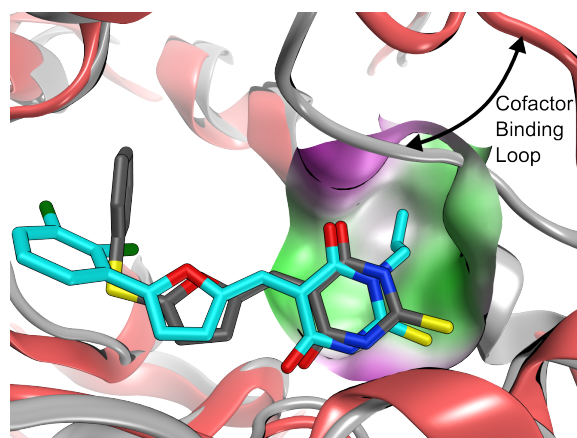
Figure 3.23: Comparison of binding models for *ThiFu1* (cyan) and *ThiFu2* (grey). The N-alkylation addressed an hydrophobic pocket that was specific for the putative apo conformation of Sirt5 (*C2*).

While the thiobarbiturate scaffold showed a similar binding mode as described for the non-alkylated derivatives, the alkyl group was placed inside a hydrophobic pocket that was only observed for an apo-like conformation of Sirt5 (*C2*, see Section 3.3.4). Thus, N-alkylated (thio)barbiturates might exploit two important features of the Sirtuin binding cleft - they bind to several conserved residue inside the C-pocket and exploit the remarkable flexibility of the CB-loop (see Figure 3.23).

One conserved water (*W3*, see Figure 3.22) might be involved in binding by forming hydrogen bonds between one of the barbiturate oxygens and the backbone of Ala59.

---

* See Section 3.3.5.

† Protocols see Appendix Section B.6.5.

Interestingly, the substrate unbound conformation of Arg105 (*conf-2*, see Section 3.3.5) is optimal to form a hydrogen bond with one of the (thio)barbiturate oxygens. However, comparable models were obtained for the E- and Z-isomers of alkylated thiobarbiturate derivatives, that is why the question for the preferred stereo configuration remains unresolved.

3.7.4 Conclusions and Perspectives

In summary, *in-vitro* and *in-silico* experiments on different Sirtuins and thiobarbituratic inhibitors revealed a number of interesting structure activity relationships. Both, thiobarbiturates and barbiturates show the same activity on Sirt5, that is why the sulfur (or oxygen) is likely not involved in strong interactions. This was also suggested by the docking models shown in Figure 3.21 and Figure 3.22.

A single alkylation of one of the thiobarbiturate nitrogens had no significant effect on Sirt5 inhibition, but double N-alkylation leads to a complete loss of activity. Hence, one of the nitrogen is critical for binding and might be involved into a hydrogen bond that is conserved across the whole Sirtuin family. Such a key residue might be the absolutely conserved aspartate* inside the C-pocket, as suggested by the docking models shown in Figure 3.21.

N-alkyl substituents of the thiobarbiturate ring were placed inside a hydrophobic area, formed by the flexible CB-Loop. This interaction might compensate for the loss of a weak hydrogen bond that was predicted for the non-alkylated derivatives and Arg105 (compare Figure 3.21 and 3.22). The (additional) pocket region adressed by alkylated thiobarbiturates, is shaped by a number of hydrophobic residues. Thus it can be assumed, that non-polar substituents at the thiobarbiturate nitrogen are preferred for binding.

The experimental data clearly showed, that furylidene-substituted thiobarbiturates are slightly more potent than benzylidene- or indolylidene derivatives (see inhibition data in Table B.3). A possible explanation was suggested by the here developed docking models, where the furan group mimics the nicotinamide-ribose moiety of NAD^+.

3.8 Virtual Screening for Novel Sirt5 Inhibitors

The search for small molecule inhibitors of Sirt5 is important to proceed with biological and biochemical characterization and to proof the therapeutical relevance of this enzyme[63]. Apart from peptidic compounds, there is a clear lack of potent and Sirt5-specific inhibitors[66]. In order to fill this gap, several virtual screenings, based on unique structural features of Sirt5, were carried out during this work.

∗ Asp143 in the case of Sirt5.

3.8.1 Succinyl-lysine Analogs

An initial virtual screening based on the recent finding, that Sirt5 binds succinylated and glutarylated lysine residues, which seems to be unique among the Sirtuin family[52]. The specificity for negatively charged lysine modifications is structurally related to the Y/R motif as explained in Section 3.2.4. To address this motif by small organic molecules, three commercial libraries were screened for compounds containing a succinyl or glutaryl substructure (see Figure 3.24). 778 compounds (0.08 % of the screened databases) contained the searched pattern and were subsequently docked to an ensemble of three different Sirt5 models*.

(A)

[#6][#7X3H1]C(=O)[CX4H2][CX4H2][CX3](=O)[OX1H0-,OX2H1]

(B)

[#6][#7X3H1]C(=O)[CX4H2][CX4H2][CX4H2][CX3](=O)[OX1H0-,OX2H1]
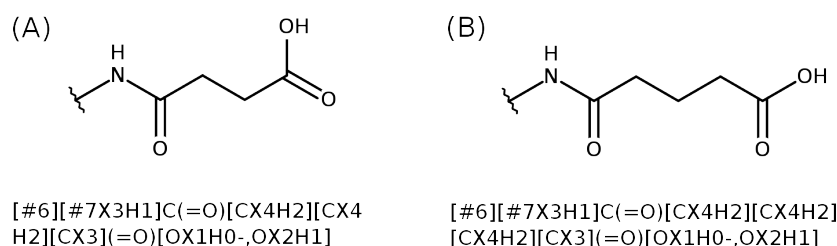
Figure 3.24: Three vendor catalogs were filtered for (A) succinyl-lysine analogs and (B) glutaryl-lysine analogs. The corresponding SMARTS patterns were used for the substructure search.

After visual inspection of 100 top scored solutions and model refinements, 14 diverse compounds were ordered from their corresponding vendors†. However, experimental tests in a fluorescence-based *in-vitro* assay‡ did not show any significant inhibition of Sirt5 desuccinylation activity for these VS candidates.

There are several reasons, why such small substrate-like probes are not appropriate to affect Sirt5 activity: First, their binding affinity might be too low compared to the competing (larger) substrate. Second, interactions distant to the Y/R motif are necessary to induce a conformational change which lead to the required conformation of Sirt5. This would be in agreement with a recently reported study on peptidic inhibitors, where only larger and specific peptides were found to be inhibitors of Sirt5[66]. However, future screenings for larger succinyl-lysine analogs might be promising to end up with active VS hits.

3.8.2 Carboxylic Acids and Sulfonamides

In order to find Sirt5 specific inhibitors which address the characteristic Y/R motif, three virtual libraries were screened for compounds containing a primary sulfonamide or carboxylic acid group. More than 1 million molecules were filtered and over 60.000

---

unique compounds were docked to an ensemble of different Sirt5 protein models[*]. The best scored compounds were clustered according to their molecular fingerprint and about 200 docking solutions were visually inspected. Finally, nine compounds (6 carboxylic acids and 3 sulfonamides) were ordered from their corresponding vendors, in order to test their activity in a fluorescence-based *in-vitro* assay[†]. Five virtual screening hits showed moderate inhibition of Sirt5 desuccinylation activity (data see Table 3.6).
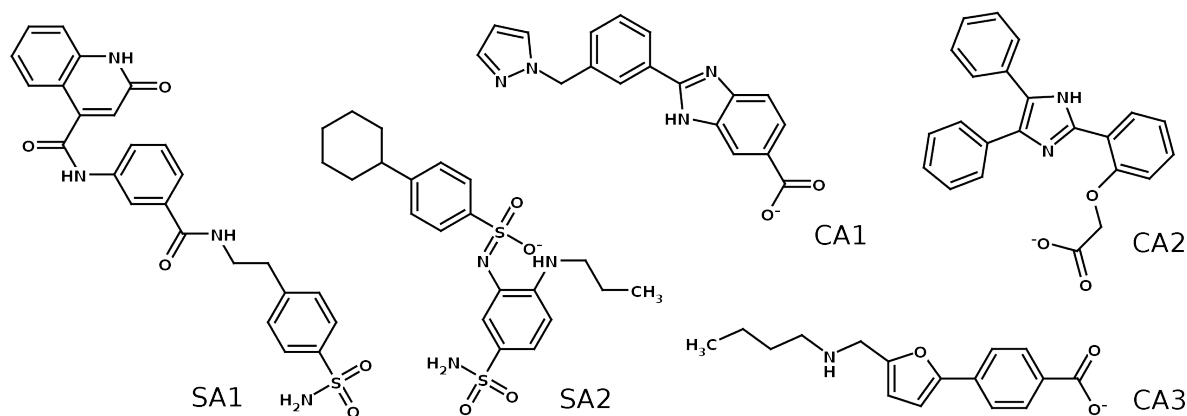
Figure 3.25: Structure of Sirt5 inhibitors resulted from virtual screening for compounds containing a carboxylic acid or sulfonamide function.

As can be seen in Figure 3.25, the two most active hits contain a sulfonamide group (*SA1-2*) and three other compounds are carboxylic acids (*CA1-3*). A binding model for the most potent compound *SA1* (IC$_{50}$ of 68 µM) was predicted by molecular docking and subsequent MD refinements. Figure 3.26 shows, that compound might bind to the substrate binding site of Sirt5 and that the sulfonamide group likely interact with the Y/R motif of Sirt5. According to this model, *SA1* forms hydrogen bonds with Gly224 and Tyr255, which were also observed for the native binding mode of the succinylated peptide (see Figure 3.3).

Although these VS hits were not highly potent in preliminary assay tests, a hit rate of 55% indicates a suitable strategy in finding active compounds (even with new scaffolds). Thus, *SA1* or sulfonamide in general are promising candidates for future virtual screenings studies.

∗   Protocols see Appendix Section B.7.2.
†   Details see Appendix Section B.2.1.

ID	Sirt5 inhibition
SA1	IC$_{50}$: 68µM
SA2	IC$_{50}$: 100µM
CA1	19% at 80 µM
CA2	14% at 80 µM
CA3	10% at 80 µM

Table 3.5: Inhibition data for Sirt5 virtual screening hits.
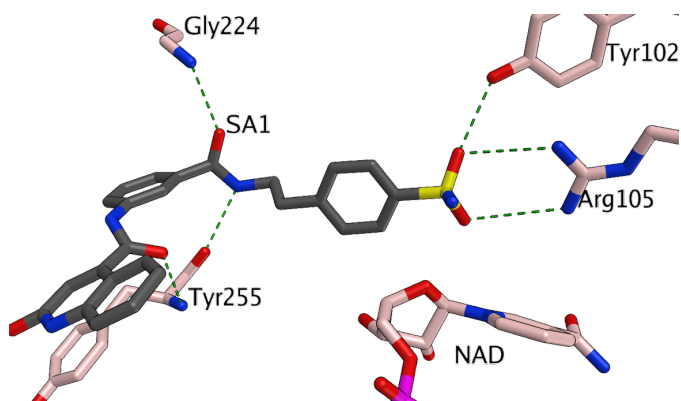
Figure 3.26: Proposed binding model for SA1 and Sirt5. Hydrogen bonds are drawn as dashed lines.

3.8.3 Amidobenzamide Screening

Compounds containing an amidobenzamide structure were proposed as Sirtuin inhibitors during initial virtual screening rounds. The most potent inhibitor *AB1* (IC$_{50}$ of 36 µM, see Figure 3.27) was an interesting lead candidate, because no inhibition was detected for Sirt3 in a comparable *in-vitro* assay.

Preliminary docking studies on *AB1* and Sirt5 suggested a binding mode inside the substrate binding site of Sirt5. The compound might form hydrogen bonds to Val221, Gly224 and Tyr255 as well as π-π-interactions with Phe223 and His158 (see Figure 3.28). Interestingly, the benzodioxan moiety of *AB1* was docked inside the acyl pocket of Sirt5, which is sterically blocked by a phenylalanine (Phe 188) in the case of Sirt3.

In order to characterize amidobenzamides as a novel class of Sirt5 inhibitors, a virtual screening based on *AB1* similarity was carried out during this work. Each molecule of the ZINC druglike database[125] was scored for fingerprint similarity to *AB1* and the 100 best scored compounds were docked to an ensemble of Sirt5 models*. 16 compounds were ordered for experimental testing and four of them inhibited Sirt5 in the micromolar range (compounds *AB2-5*, see Figure 3.27).

The most potent hit *AB2* (IC$_{50}$ of 41 µM) indicates, that substitutions of the diphenyl moiety of *AB1* are tolerated. In contrast, substitutions of the benzodioxan moiety resulted in significant lower inhibition values as shown for *AB6*. Thus, a screening for amidobenzamide-benzodioxan derivatives might be promising for future optimization rounds.

---

* Protocols see Appendix Section B.7.3.
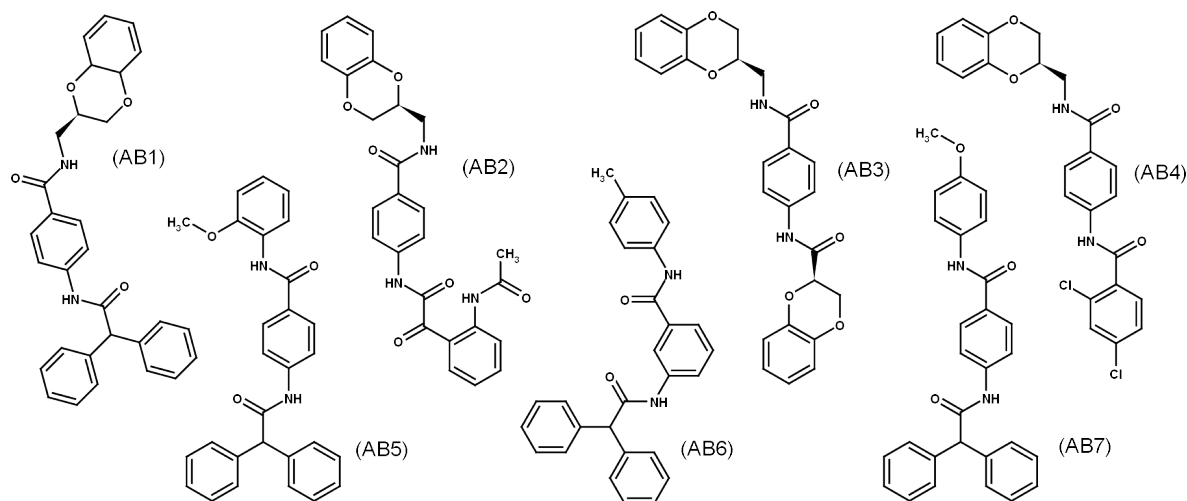
Figure 3.27: Sirt5 inhibitors resulted from virtual screening for amidobenzamide derivatives.

Interestingly, the four amidobenzamides with the highest activity (*AB1-AB4*) showed a R-configuration at the chiral center nearby the benzodioxan moiety, whereas a similar compound in S-configuration (*AB9*, see Figure B.15) was nearly inactive. Thus, Sirt5 inhibition by amidobenzamide derivatives might be stereoselective, which is in agreement with spatial limitations shown for the binding model of *AB1* (Figure 3.28).

ID	Sirt5 IC$_{50}$
AB1	36 µM
AB2	41 µM
AB3	48 µM
AB4	50 µM
AB5	75 µM
AB6	83 µM
AB7	88 µM

Table 3.6: Inhibition data for Sirt5 virtual screening hits with an IC$_{50}$ value below 100 µM. The full list can be found in the Appendix Section B.7.3.
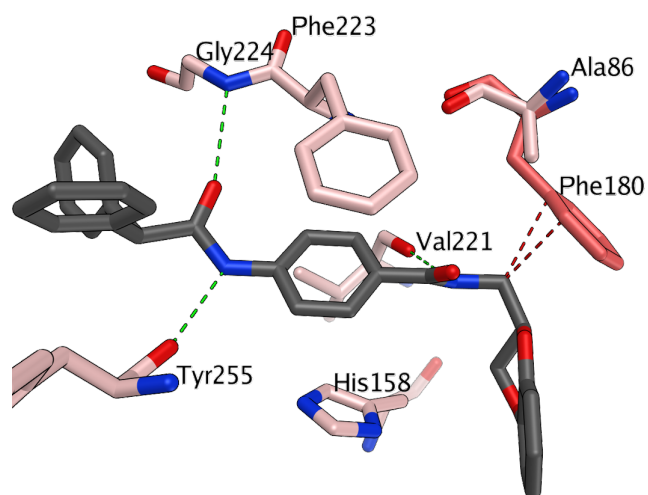
Figure 3.28: Binding model of *AB1* and Sirt5 (light pink). The benzodioxan moiety might bind to a region that is blocked in the case of Sirt3 (dark pink). Hydrogen bonds are drawn as green and sterical hinderance as red dashed lines

3.9 Conclusions

Sirt5 is a novel target that needs to be characterized by biological, biochemical as well as computational studies. Due to its unique activity as protein lysine desuccinylase/deglutarylase in human mitochondria, it has a great potential to become a target for therapeutical interventions of metabolic disorders.

For a proper *in-silico* characterization of Sirt5, an analysis of the protein structure, the development of binding models as well as the discovery of Sirt5-specific inhibitors is necessary. During this work, the molecular structure of Sirt5 was analyzed in detail with a focus on structural flexibility and pocket solvation.

Because current crystal structures of Sirt5 are biased towards substrate-bound conformations, MD simulations were carried out to explore the conformational space of the protein. The application of an enhanced sampling technique (accelerated MD) revealed a significant flexibility of single residues as well as whole secondary structure elements forming the binding site of Sirt5. The highest mobility was observed for the cofactor binding loop and the Sirt5-specific *Insertion-loop*, especially during the substrate-unbound simulation of the protein.

Principal components as well as domain angle analysis clearly indicated a transition from the initially closed to an open conformation, and a structural comparisons of representative snapshots with apo structures of homologous proteins revealed a high similarity between them. Thus apo models sampled during MD simulations can be used for docking and virtual screening experiments on Sirt5.

The Sirt5-specific Arg105 seems to prefer two distinct side chain conformations: One conformation (*conf-1*) is specific for the recognition of succinylated peptides and the alternative conformation (*conf-2*) seems to be relevant for the substrate-unbound state of Sirt5. It became clear, that both conformations should be considered for the development of binding models as well as structure-based virtual screening campaigns. Despite a large number of studies published for Sir2-like proteins in the last decade, no detailed analysis of the pocket hydration was reported until now. To fill this gap, 3D-RISM calculations were carried out, and a number of important waters were identified inside the binding cleft of Sirt5. Putative roles of these waters were suggested and they were considered during the development of protein-ligand models as well as virtual screening experiments.

Binding models for Sirt5 and CPS1-derived peptides were generated and further modifications of their chemical structures were suggested, in order to increase their affinity and specificity. Furthermore, a consistent binding mode of thiobarbiturate inhibitors was developed for Sirt1-3 as well as Sirt5. It was shown that the incorporation of receptor flexibility and conserved water molecules is necessary to end up with reliable model, especially in the case of N-alkylated derivatives.

In order to find novel inhibitors of Sirt5, a number of different virtual screening strategies were applied. It was shown that small succinyl-lysine analogs are not adequate to inhibit Sirt5, but alternative strategies resulted in several compounds which inhibited Sirt5 in the micromolar range of concentration. A number of novel inhibitors were found by

virtual screening, including sulfonamides and compounds containing a carboxylic acid function which likely interact with the Sirt5-specific residue Arg105.

However, there are lot of challenges in discovering Sirt5-specific inhibitors: Until now, there is a lack of experimental data, validated datasets and crystal structures showing binding modes of small organic compounds. Furthermore, the high conformational flexibility and the complex enzymatic mechanism of Sirtuins are important hurdles for computer-based approaches.

The current study contributes to an increased understanding of the structural dynamics and the role of pocket solvation for Sirt5. It was pointed out, that both aspects are highly relevant for virtual screening and the development reliable protein-ligand binding models. Future work can be done by studying the influence of protein flexibility on the pocket solvation states. In addition, models and inhibitors found during this work, provide a promising starting point for future virtual screening campaigns on this exciting target.

CHAPTER 4

Molecular Modeling Studies on Sirtuin 4

Up to now, Sirt4 is the least characterized member of human mitochondrial Sirtuins. Critical roles in regulating insulin secretion, fatty acid metabolism and ATP homeostasis were suggested, and it was shown, that the enzyme has tumor suppressor functions by inhibiting glutamine metabolism and thereby affecting proliferation and survival of tumor cells[126–129]. Thus, Sirt4 might be from therapeutical relevance for various metabolic diseases (e.g. diabetes type 2) and also for cancer therapy.

Very recently, an efficient removal of biotinyl and lipoyl groups of modified lysine residues was reported[51]. However, a detailed characterization is still necessary and also a molecular structure of Sirt4, for example in complex with one of the suggested substrates, needs to be resolved. In the current study, a protein structure of Sirt4 was modelled, in order to predict putative substrates and to propose potential inhibitors by a structure-based virtual screening approach.

4.1 Homology Modeling

Due to a high structural conservation among Sir2-like proteins, a template-based modeling was carried out for Sirt4. Initially, several modeling servers were tested*, but delivered very inhomogeneous results, that is why a manual protocol was favored. The protocol was validated on Sirt5† and resulted in homology models which were highly similar to available crystal structures of this protein.

The procedure starts with a search for the best template structure contained in the Protein Data Bank (PDB), followed by multiple sequence alignments and the generation of several Sirt4 homology models. The quality of all models was assessed by several scoring functions and selected models were further refined after visual inspection. Each step of the Sirt4 modeling process will be described in the following sections.

---

*   Swiss-Model[130] and I-Tasser[131] servers.
†   The structure of Sirt5 was modelled based on a homolog Sir2-like structure.

4.1.1 Template Structures

Although Sirtuins share a common fold, their sequence identity is only low*, which is critical for a template-based modeling approach. Since a simple sequence-based method such as BLAST[132] might lead to suboptimal results, the following comprehensive algorithms were used to detect protein homology:

HHPred predicts homology by a pairwise comparison of profile hidden Markov models[133]

I-Tasser predicts template structures by a method called protein threading[131]

Both algorithms where chosen, because they showed a superior performance in a recent CASP† contest. The sequence of Sirt4 was downloaded from Uniprot and served as input to find the closest Sirt4 homologs within the PDB‡.
Consistently, *HHPred* and *I-Tasser* suggested the same proteins as top five homologs of Sirt4 (see Table 4.1). Four hits were bacterial Sirtuins including Sir2-Tm from *Thermotoga maritima*, Sir2-Pf from *Plasmodium falciparum* and Sir2-Af as well as Sir2-Af2 from *Archaeoglobus fulgidus*. Human Sirt5 was the closest homolog in eukaryotes and was scored as best Sirt4 template by the I-Tasser algorithm.

Protein	Organism	Sequence Identity	Sequence Coverage	Rank I-Tasser (HHPred)	PDB Code
Sirt5	*Homo sapiens*	27 %	0.93	1 (5)	3RIY
Sir2-Tm	*Thermotoga maritima*	31 %	0.85	2 (1)	2H59
Sir2-Pf	*Plasmodium falciparum*	29 %	0.88	3 (2)	3U31
Sir2-Af2	*Archaeoglobus fulgidus*	35 %	0.85	4 (3)	1S7G
Sir2-Af	*Archaeoglobus fulgidus*	32 %	0.87	5 (4)	1M2G

Table 4.1: Top five homologous proteins of Sirt4 resulted from template search within the PDB. The coverage is equal to the number of aligned residues divided by the length of the query protein.

The closest bacterial homolog of Sirt4 was Sir2-Tm, suggested as best template from the HHPred results. Interestingly, a phylogenetic study of Sir2-like proteins already described Sir2-Tm as an *intermediate* Sirtuin, evolutionary situated between Sirt4 and Sirt5 homologous proteins[135]. Finally, it was not clear if Sirt5 or Sir2-Tm is the closest homolog of Sirt4, therefore both candidates were used to generate a sample of homology models.

---

* Average sequence identity below 30%.
† Critical assessment of techniques for protein structure prediction[134].
‡ Protocols see Appendix Section C.2.1.

4.1.2 Sequence Alignments

Due to the low sequence identity between Sirt4 and Sirt5 (27%) as well as Sirt4 and Sir2-Tm (31%), the alignment is the most critical step in this modeling protocol. To obtain reliable results, a multiple alignment of all human Sirtuins and Sir2-Tm was constructed using structure information (if available)*. Alignment constraints were applied for highly conserved residues, which are involved in elementary functions such as NAD^+ and substrate-lysine binding (see Table 4.2). The constraints were equally distributed among the whole sequence of Sirt4 (see Figure 4.1), in order to guide the alignment process of surrounding (unconserved) regions.

Sir2-Tm	Sirt1	Sirt2	Sirt3	Sirt4	Sirt5	Sirt6	Sirt7	Function
G21	G261	G84	G145	G62	G58	G50	G107	NAD^+ binding
G38	G278	G102	G163	G80	G74	G67	G124	CB-Loop
Q98	Q345	Q167	Q228	Q143	Q140	Q111	Q167	NAD^+ binding
H116	H363	H187	H248	H161	H158	H131	H187	Catalysis
C124	C371	C195	C256	C169	C166	C140	C195	Zn binding
C127	C375	C200	C259	C172	C169	C142	C198	Zn binding
C148	C395	C221	C280	C220	C207	C164	C225	Zn binding
C151	C398	C224	C283	C123	C212	C175	C228	Zn binding
V160	V412	V233	V292	V232	V221	L184	V237	Substrate binding
G188	G440	G261	G319	G260	G249	G213	G268	NAD^+ binding
N214	N465	N286	N344	N286	N275	N238	N297	NAD^+ binding

Table 4.2: Highly conserved residues that were used as constraints for the multiple sequence alignment procedure.

As can be seen in Figure 4.1, only functional residues involved in NAD^+ binding, zinc coordination or substrate-lysine binding are well conserved, but flanking residues, especially in the zinc binding domain, are highly diverse. Interestingly, the *Insertion-loop* as well as the Tyr102/Arg105-motif which were described as Sirt5-specific elements[†], are also present in Sirt4 (Tyr105/Arg108, see Figure 4.1).
Furthermore, an alanine (Ala86) that is important for the *opening* of the Sirt5 acyl pocket, is substituted to a structural similar valine (Val90) in Sirt4. In respect of the final alignment, Sirt4 is clearly more related to Sirt5 than to all other human Sirtuins including Sir2-Tm which also lacks a Tyr/Arg motif. Thus, Sirt5 was found to be an appropriate template for a subsequent modeling of the Sirt4 protein structure.

---

* Protocols see Appendix Section C.2.2.
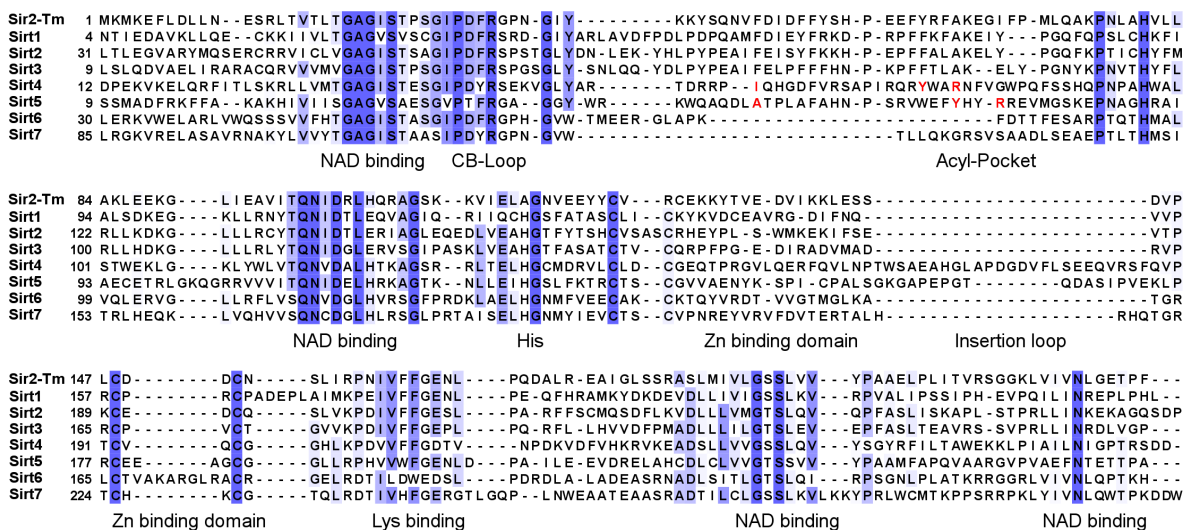† See Section 3.2.4.

Figure 4.1: Sequence alignment of the catalytic core of Sirt1-7 and Sir2-TM. Conserved columns are colored blue. The Tyr102/Arg105 motif of Sirt5 is also present in Sirt4 (Tyr105/Arg108, see red highlighted residues).

4.1.3 Modeling and Structure Refinement

Within this section, the generation, selection and refinement of a Sirt4 homology model will be briefly described - a more detailed protocol can be found in the appendix of this work*.

Due to N-terminal cleavage during mitochondrial import[50], residues 1-28 were truncated from the Sirt4 sequence for the subsequent modeling process. 15 models were generated for each template, using the Modeller software[136] and the sequence alignments shown in Figure 4.1. The coordinates of NAD^+, as bound in productive conformation†, were included as rigid body constraints, to avoid artificial side chain conformations inside the modelled NAD^+ pocket.

The best five models, scored by the Modeller objective function, were assessed for geometrical and stereochemical quality using Molprobity and the composite scoring function QMEAN[137,138]. QMEAN covers different aspects of protein folding and stability and also estimates the local residue error, for example at the ligand binding site.

For each subset of Sirt4 models, the model with highest QMEAN score was selected and the quality was compared with the quality of both selected template structures. As can be seen from Table 4.3, both template structures showed the highest quality in respect to geometry and QMEAN scores. This was not surprising, because many quality assessment functions are calibrated on experimental structures and crystal structures are usually optimized in respect to their geometry.

---

* See Appendix Section C.2.
† Extracted from the Sirt5 complex structure (3RIY).

However, the Sirt4 model based on the Sirt5 structure revealed a slightly better quality than the model generated from the Sir2-Tm template. This was a bit surprising, since Sirt4 and Sir2-Tm share a higher sequence similarity - but it demonstrates that global similarity is not the only relevant aspect for choosing appropriate templates.

Protein	*PDB code (Template)*	*Sequence Identity*	*Poor Rotamers*	*Ramachandran Outliers*	*Clash Score*	*QMEAN Z-Score*
Sirt5	3RIY	-	0.92%	0.00%	3.15	0.764
Sir2-Tm	2H59	-	3.32%	0.41%	4.14	0.797
Sirt4*	(3RIY)	27%	3.38%	0.75%	9.93	0.611
Sirt4*	(2H59)	31%	6.83%	3.87%	13.43	0.551
Sirt5*	(1M2G)	43%	2.74%	1.64%	8.10	0.643

Table 4.3: The quality of each homology model (indicated by *) and the template structures was assessed by Molprobity and the QMEAN scoring function. A Sirt5 homology model based on Sir2-Af structure was included for validation purpose.

A Sirt5 model developed for validation purpose* obtained comparable scores as the best Sirt4 model (see Table 4.3). This was quite important, because key structural features, such as residues involved in NAD^+ and substrate binding, were modeled accurate enough.

Consequently, the Sirt4 model based on Sirt5 was chosen as final result and further refined by adjusting side chain conformations according to the template structure[†]. The modelled complex of Sirt4 and NAD^+ showed superior stability in a 15 nanosecond MD simulation and was subsequently used for a detailed structure analysis as well as docking and virtual screening experiments.

4.1.4 Structural Characteristics of Sirt4 Model

A general comparison of the Sirt4 homology model and the template structures of Sirt5 and Sir2-Tm is shown in Figure 4.2. As already known from other Sir2-like structures, the Rossmann fold domain is highly conserved among the whole Sirtuin family. Consistently, the Cα-RMSD between the Sirt4 model and both template structures was approximately 1.3Å at this domain and thereby significantly lower than the Cα-RMSD at the zinc binding domain (about 2.0Å).

[∗] See Appendix Section C.2.3.
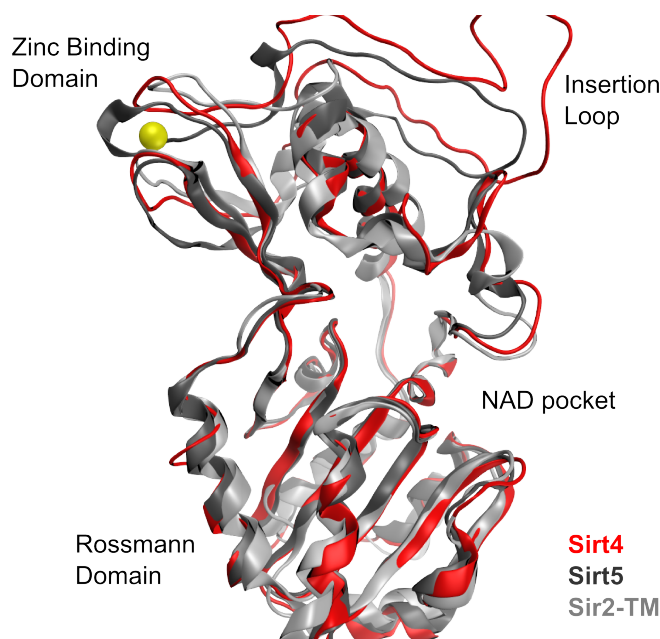[†] Protocols see Appendix section C.2.3.

Figure 4.2: Ribbon diagram of the Sirt4 homology model (red) superimposed with the template structure of Sirt5 (dark grey) and Sir2-Tm (light grey). The zinc cation is drawn a yellow ball.

Interestingly, Sirt4 and Sirt5 share a common *Insertion-loop* (see Figure 4.2), which is not present in Sir2-TM and all other human Sirtuin types*. However, this loop might be important for protein-protein interactions, but the exact role is not clear until now. Common features, but also characteristic differences were observed at the binding cleft of Sirt4 and its homologs.

4.1.4.1 Substrate and NAD$^+$ Binding Pocket

A superpositioning of the Sirt4 model and both templates structures† revealed nearly identical NAD$^+$ pockets of all three enzymes (see Figure 4.3). However, two substitutions were observed among the residues that are involved in NAD$^+$ binding:

(i) A glutamic acid, that interacts with the primary amine of the NAD$^+$ adenosine moiety, is only present in Sirt5 (Glu64) and Sirt4 (Glu68), but not in Sir2-Tm. Possibly it affects the binding affinity of NAD$^+$ and prevents the binding of derivatives, such as eNAD$^+$ or pNAD$^+$ (see Figure 2.9).

(ii) Sirt4 has an additional arginine (Arg87) nearby the catalytic center of the binding cleft (see Figure 4.3). The exact orientation of the Arg87 side chain is hard to predict by homology modeling, but a rotation towards the inner binding pocket would allow interactions with both substrates.

∗   See sequence alignments in Figure 4.1
†   Protocols see Appendix Section C.2.4.

Arg87 was very mobile during a MD simulation of Sirt4, that is why putative interactions with NAD$^+$ (as shown in Figure 4.3) should not be over-interpreted. All in all, the NAD$^+$ pocket of Sirtuins is highly conserved and it seems to be difficult to develop subtype specific inhibitors which bind at this region.
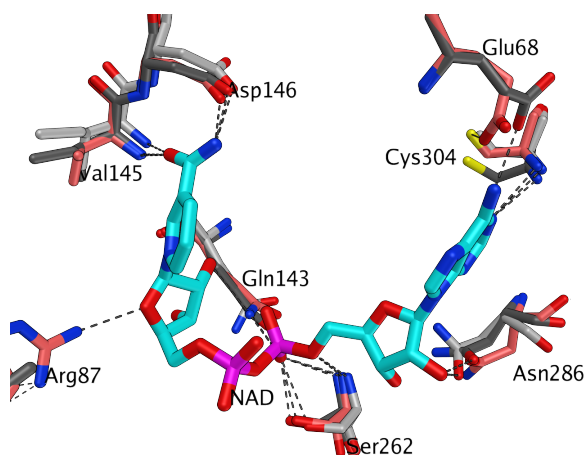

Figure 4.3: NAD$^+$ (cyan) bound to Sir2-Tm (light grey), Sirt5 (dark grey) and Sirt4 (light red). Hydrogen bonds are drawn as dashed lines.
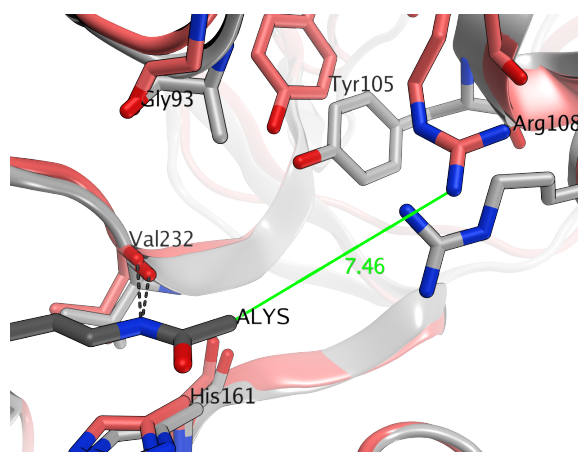
Figure 4.4: Acetylated lysine residue (dark grey) modeled at the Sirt5 (light grey) and Sirt4 (light red) binding sites. The distance between the acetyl group and Arg108 of Sirt4 is 7.46 Å.

In contrast, the substrate binding sites of Sirtuins are much more divergent in respect to structural as well as physicochemical properties. While the substrate-lysine binds in a comparable mode to all Sirtuins, the specific posttranslational modification occupies a region that is characteristic for each Sirtuin type*.

As can be seen in Figure 4.4, Sirt4 contains a tyrosine (Tyr105) and arginine (Arg108) residue deep inside the binding cleft, which are proximal to the functional important Y/R-motif of Sirt5. The distance between a modeled acetyl-lysine residues and the guanidino group of Arg108 was about 7.46Å, thus appropriate for longer (acidic) lysine modification, such as succinyl or glutaryl groups.

In section 4.2, several lysine modifications will be probed by molecular modeling, in order to predict their compatibility with the Sirt4 binding pocket.

4.1.4.2 Compatibility with Conserved Waters

In section 3.4, seven conserved waters were described for Sirt5 and other human Sirtuins. To confirm the reliability of the here developed Sirt4 protein model, most of these waters should also fit inside the predicted binding pocket.

---

* See sequence alignment in Figure 4.1.

In order to proof this by an unbiased method, the continuous solvent distribution was calculated for the Sirt4-NAD$^+$ complex, using the 3D-RISM approach[121]. Explicit water molecules were mapped into the most likely water locations and compared with the solvation model obtained for Sirt5*.

As can be seen in Figure 4.5, six out of seven conserved waters were predicted nearby their assumed location at the binding cleft of Sirt4. Only water W6 was not obtained, most probably due to structural differences between Sirt4 and Sirt5 at this specific region (acyl pocket). All other six waters were confirmed and their approximated binding energies were comparable to the binding energies calculated for the Sirt5-NAD$^+$ complex (see Table 4.4).
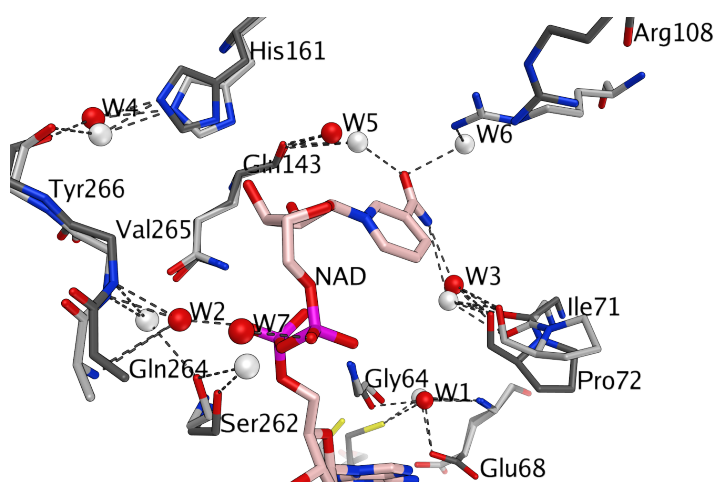

Figure 4.5: Predicted waters inside Sirt4 pocket (dark grey, red), superimposed with conserved waters found for Sirt5 (light grey, white). Hydrogen bonds are indicated by dashed lines.

ID	ΔG_{pred} Sirt4	ΔG_{pred} Sirt5
W1	-2.75	-2.68
W2	-2.03	-2.61
W3	-3.12	-3.03
W4	-2.61	-2.70
W5	-2.14	-2.76
W6	n.d.	-2.44
W7	-1.93	-2.73

Table 4.4: Predicted binding energies of conserved waters as approximated by the radial distribution functions obtained from 3D-RISM calculations.

4.1.5 Implications for Docking and Virtual Screening

Indeed, homology models based on templates with low sequence identity should be analyzed critical. Even the best modeling algorithms can only guess the conformation of loops and amino acid side chains, especially for non-conserved residues. Because docking programs are highly sensitive concerning minimal changes in atomic positions, already small prediction errors can lead to totally misleading results and thereby wrong binding hypothesis.

In the case of the Sirt4 homology model, the uncertainty is only minimal at the Rossmann fold domain as well as the NAD$^+$ binding pocket. As shown in Figure 4.1 and Figure 4.3, the conservation is high enough to claim a sufficient accuracy of the predicted protein structure.

---

* Protocols see Appendix section C.2.5.

In contrast, the region where the substrate-lysine modification binds (acyl pocket), is highly diverse among all Sirtuins and therefore hard to predict by a template-based modeling approach. Thus, docking and structure-based virtual screenings at the NAD$^+$ pocket can be assumed as safe, but results obtained for the Sirt4 acyl pocket should be interpreted carefully. However, six conserved waters which were found for other human Sirtuins, agreed well with water locations predicted at the Sirt4 binding pocket. Therefore, they should be included in molecular docking and virtual screening studies.

4.2 Docking of Putative Substrates

Sirt4 did not show any significant deacetylase activity and a proposed function as ADP-ribosyltransferase is still under discussion[57]. A recent study showed an efficient removal of lipoyl- and biotinyl groups from modified lysine residues, but alternative PTMs might be also cleaved by Sirt4[51]. Within the current study, several CPS1-based peptide derivatives* were docked to the protein model of Sirt4, in order to proof their compatibility with the predicted binding site.

In a first proof-of-principle, lipoyl- and biotinyl-lysine peptides (*CP11* and *CP12*, see Figure B.7) were docked to the modelled complex of Sirt4 and NAD$^+$ †. To guide the conformational search, the flanking residues of the modified lysine were constrained at their (most likely) positions, obtained from the superimposed complex of zSirt5 and *CP3* (PDB: 4UTN). Several docking results were refined by an energy minimization, to obtain the final models shown in Figure 4.6 and Figure 4.7. As can be seen from both pictures, the lysine modification of *CP11* and *CP12* fits nicely inside the acyl pocket of the Sirt4. The heterocycle was placed between the side chains of Tyr105 and Arg108, without showing strong electrostatic interactions with one of these residues. However, a weak hydrogen bond between the biotinyl carbonyl group of *CP12* and the hydroxyl of Tyr105 (see Figure 4.7) was observed for several docking result.

Because the Tyr/Arg motif of Sirt5 was shown to be critical for substrate recognition[67], it was assumed that also Sirt4 binds acidic lysine modifications by the related residues Tyr105 and Arg108. In order to proof this hypothesis, malonylated (*CP2*), succinylated (*CP3*) and glutarylated (*CP4*) peptides were docked to the homology model of Sirt4‡. Interestingly, the final docking models showed analog protein-peptide interactions as observed for the experimentally resolved structures of zSirt5 (compare Figure 4.8 and Figure 3.13).

---

*   See Section 3.6
†   Protocols see Appendix Section C.3.
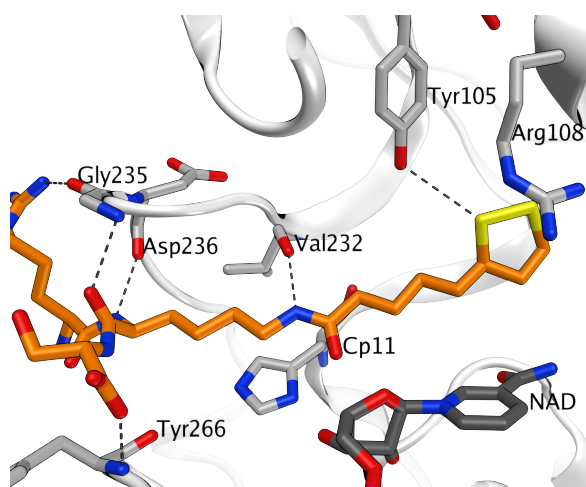‡   Protocols see Appendix Section C.3.

Figure 4.6: Putative binding mode of lipoyl-lysine CPS1-based peptide (CP11, orange) and Sirt4. Hydrogen bonds are drawn as dashed lines.
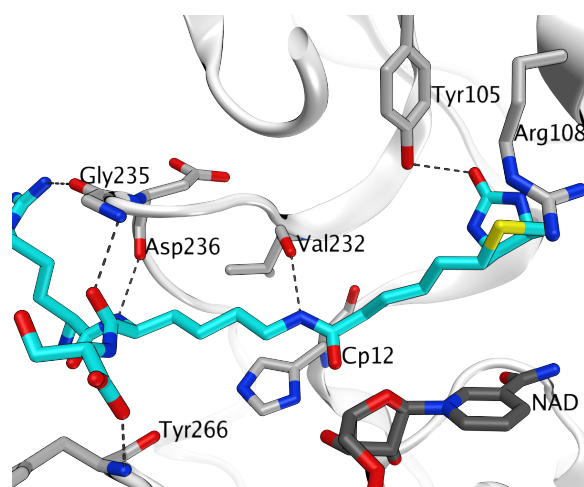
Figure 4.7: Putative binding mode of biotinylated CPS1-based peptide (CP12, blue) and Sirt4. Hydrogen bonds are drawn as dashed lines.

Due to a conserved hydrogen bond between the substrate lysine and the backbone of Val232, only *CP3* and *CP4* were able to address the Tyr/Arg motif of Sirt4. While the glutarylated peptide (*CP4*) seems to have an optimal length to interact with Arg108, shorter acyl groups, like the malonyl group of *CP2*, are possibly not appropriate to form the desired saltbridge (see Figure 4.8).

However, it was not possible to obtain alternative rotamers of Arg108, because the variability was restricted by the proximal side chain of Arg87. As shown in Figure 4.9, position 3 of the glutaryl group of *CP4* is only 3.6Å distant to the guanidino group of Arg87 - thus it might be possible, that this residue is also involved in substrate recognition. Indeed, it is not clear if the side chain of Arg87 is rotated towards the catalytic site, but if so, it might have interesting consequences for the type of reaction catalyzed by Sirt4.

Another interesting residue is Gly93, which is substituted to an alanine (Ala86) in the case of Sirt5 (see Figure 4.9). Such a substitution might increase the space for more bulky lysine modifications, which is in agreement with the recently proposed lipoylated and biotinylated substrates[51].
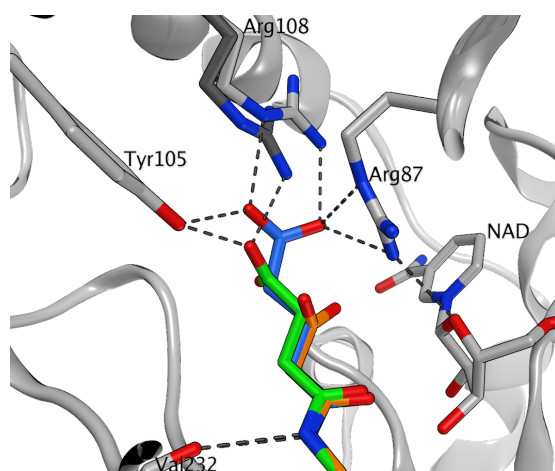
Figure 4.8: Putative binding mode of CP2 (orange), CP3 (green) and CP4 (blue) at the Sirt4 substrate pocket. Slightly different conformations of Arg108 are possible (light and dark grey). Hydrogen bonds are drawn as dashed lines.
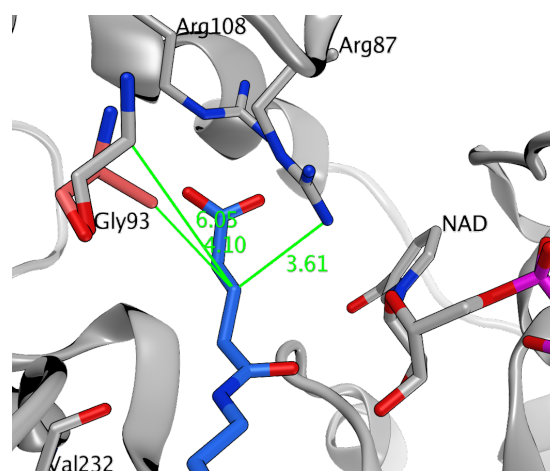
Figure 4.9: Putative binding mode of CP4 (dark grey) and Sirt4. An alanine residue in Sirt5 (light red) is substituted to Gly93 in Sirt4, which results in more space for modifications on position 3 of the acyl group. Distances (in Å) are drawn as green lines.

4.3 Virtual Screening for Sirt4 Inhibitors

Virtual screening for Sirt4 inhibitors is important to proceed with biological and biochemical characterization, but also challenging due to the lack of experimental data. Currently, ligand-based approaches are not applicable* and a structure-based virtual screening can only be done by using computationally predicted protein models.

To discover the first small molecule inhibitors of Sirt4, the here developed homology model was used for a virtual screening strategy with moderate risk. The screening based on recently determined crystal structures of Sirt3 in complex with different ELT inhibitors, which showed a general principle how to inhibit Sirtuin activity [78]. As shown in Figure 4.10, the inhibitor ELT-11c binds competitively to the binding cleft of Sirt3, by simultaneously adressing residues involved in substrate binding (e.g. Val292 and Glu296) as well as residues involved in binding of productive NAD$^+$ (e.g. Ile230 and Asp231).

A superpositioning of the Sirt3 structure inhibited by ELT-11c (PDB: 4JSR) and the Sirt4 homology model indicated, that such a binding mode is transferable to other Sirtuins due to the conservation of all protein residues involved in binding (see Figure 4.11). However, several differences were observed for surrounding residues, thus subtype specific molecules can be obtained, for example by a structure-based virtual screening

---

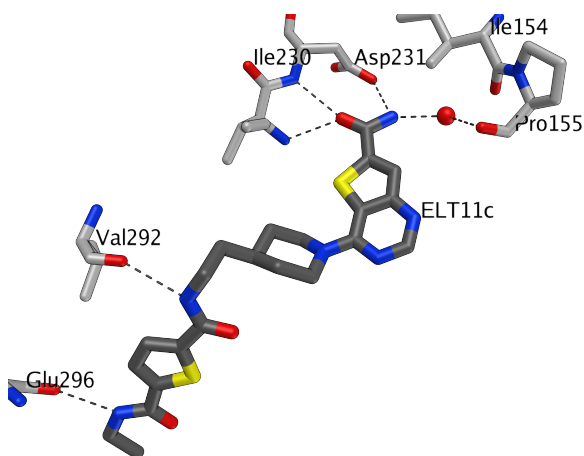* Because no inhibitor was reported for Sirt4 until now.

approach.

Figure 4.10: Structure of Sirt3 inhibited by the ELT inhibitor 11c (PDB: 4JSR). Hydrogen bonds are drawn as dashed lines.
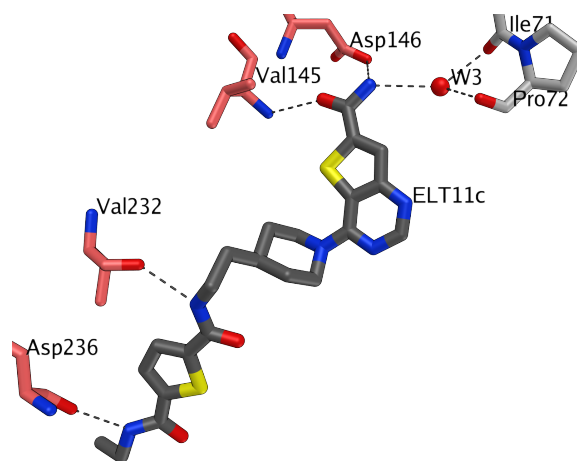

Figure 4.11: Docking model of ELT inhibitor 11c and Sirt4. The red highlighted residues and water W3 were used as constraints for virtual screening.

In order to discover a number of diverse Sirt4 inhibitors, a large-scale virtual screening was carried out during this work: The Princeton database* was prefiltered for druglike and diverse compounds and about 470.000 molecules were docked to the homology model of Sirt4. The pose sampling was constrained by the postulated hydrogen bonds interactions shown in Figure 4.11 and the water *W3* was included as part of the protein model[†]. The 10.000 best scored compounds were subjected to a diversity clustering and about 200 compounds were closely analyzed to proof the plausibility of the generated docking poses. Finally, 43 compounds[‡] were ordered from Princeton, in order to test their *in-vitro* activity in newly developed Sirt4 assay.

Most of the ordered compounds were structural distinct to the template inhibitor ELT-11c, as can be seen for the best scored molecules (*VS41-43*) shown in Figure 4.12. Nevertheless, all virtual screening hits satisfied at least three of the five hydrogen bond constraints that were applied for the molecular docking experiment. As examplarily shown for *VS41* (Figure 4.13) and *VS42* (Figure 4.14), several compounds were suggested to bind to the nicotinamide binding residues Val145 and Asp146 as well as the substrate-lysine binding residue Val232. In some cases, the conserved water *W3* was involved in hydrogen bond interactions, but in other cases, the same water was displaced by bulky ligand group, such as the nicotinamide-mimicking moiety of *VS43*. However, none of the 200 inspected models satisfied all five hydrogen bond constraints, possibly due to the limited number of docking results that were manually analyzed.

---

*   Princeton Express collection 2013 (about 700.000 molecules).

†   Protocols see Appendix Section C.4.

‡   Structures see Appendix Section C.4.
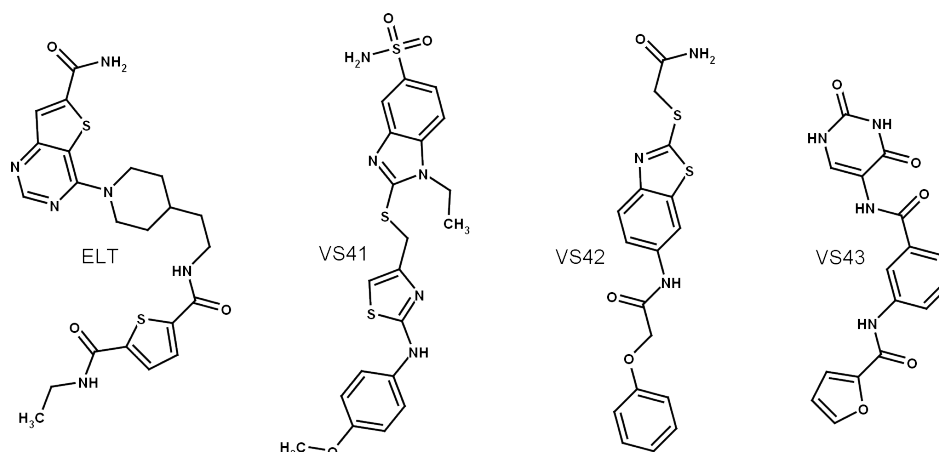
Figure 4.12: Structures of ELT inhibitor and the three best scored virtual screening hits VS41-43.

It will be interesting to see, if an inhibition of Sirt4 can be confirmed by the *in-vitro* assay test currently carried out at University Bayreuth*. If this is the case, such compounds can be used for further virtual screening rounds in order to improve their potency and/or selectivity.
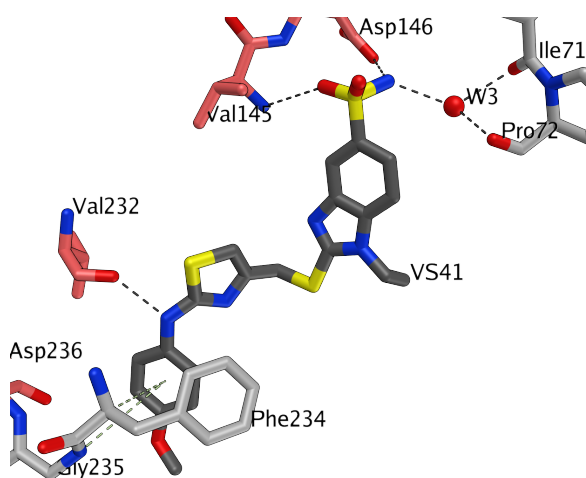
Figure 4.13: Docking model of Sirt4 virtual screening hit VS41. The red highlighted residues and water W3 were used as constraints. Hydrogen bonds are drawn as dashed lines.
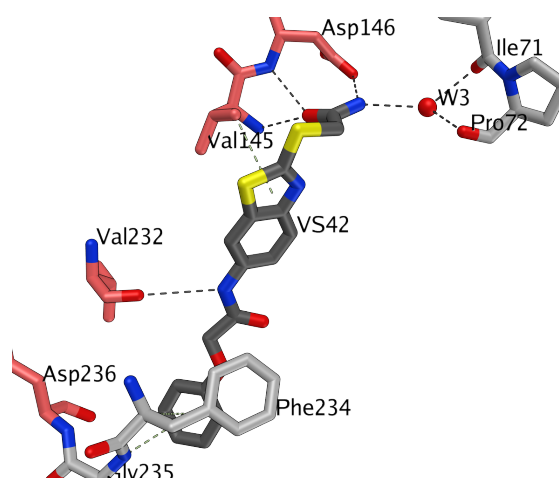
Figure 4.14: Docking model of Sirt4 virtual screening hit VS42. The red highlighted residues and water W3 were used as constraints. Hydrogen bonds are drawn as dashed lines.

∗ Group of Prof. Steegborn, University Bayreuth.

4.4 Conclusions

Sirt4 is a potential target to support cancer therapy and to treat metabolic diseases, such as diabetes type 2[126,129]. However, we are still at the beginning to understand the biological and chemical functions of this protein, thus further research is necessary, also in the field of structure biology and medicinal chemistry.

Up to now, there are certain difficulties to study Sirt4 *in-vitro*, that is why the current work focussed on a pure *in-silico* approach. A protein structure was predicted and putative substrates as well as small organic inhibitors were suggested by means of docking and subsequent model refinement. The challenge in developing a Sirt4 homology model was a comparable low sequence identity to all template structures currently available in the PDB. A multiple sequence alignment of all human Sirtuins revealed that only amino acids involved in NAD^+ binding, zinc coordination and substrate-lysine binding are conserved among the whole family. About 60% of the sequence is non-conserved, which is critical for generating reliable alignments as necessary input for homology modeling algorithms.

Nevertheless, a set of Sirt4 models was developed from two distinct templates (Sir2-Tm and Sirt5), whereas the model based on a Sirt5 structure showed better properties according several validation approaches. The overall fold and especially the NAD^+ pocket of Sirt4 is very similar to all other human Sirtuins, which leads to the assumption that NAD^+ competitive inhibitors of other Sirtuins might be also active for Sirt4.

In contrast, the substrate binding site is much more diverse among the Sirtuin family - an important aspect that can be exploited by the design of subtype specific inhibitors. The here developed protein model revealed a Tyr/Arg motif deep inside the acyl pocket of Sirt4* - an analog motif was shown to be critical for the substrate specificity and the desuccinylation/deglutarylation reaction catalyzed by Sirt5[67].

Consequently, the predicted structure of Sirt4 was computationally probed by selected CPS1-based peptides which has been discovered as *in-vitro* substrates of Sirt5. Whereas malonylated peptides seemed to be suboptimal to address the (slightly shifted) Tyr/Arg motif of Sirt4, glutarylated peptides were appropriate according to the docking results. Due to several amino acid substitutions between the acyl pockets of Sirt4 and Sirt5, analog moieties or even small modifications of the glutaryl group might be also relevant. It will be interesting to see, if these *in-silico* substrate predictions can be confirmed by upcoming *in-vitro* assay tests of CPS1-based peptide derivatives.

Although it seems to be critical to used homology models for a blind virtual screening campaign, it was shown that a carefully chosen strategy can be successful to detect inhibitor candidates for a novel target protein. An interaction-based screening of a large and diverse compound library, leads to a number of Sirt4 inhibitor candidates suggested for *in-vitro* testing. While most of these virtual screening hits are structural distinct to all other Sirtuin inhibitors reported until now, they are potentially able to mimic a conserved binding motif, that was observed for a series of potent Sirt3 inhibitors.

∗ Tyr105 and Arg108, see Section 4.1.4.1.

However, it will be interesting to see if an inhibition of Sirt4 can be confirmed by upcoming assay tests of these compounds. Indeed, experimental data is elementary to validate the models and assumptions developed within the current work.

Acknowledgements

First, I thank my supervisor Prof. Dr. Wolfgang Sippl for academic guidance and permanent support to finish this work. I would also like to thank all my former colleagues and friends at the Medicinal Chemistry group for their help, interesting discussions and a pleasant working atmosphere. For great technical support and many stimulating discussions I thank Martin Pippel and German Erlenkamp. Dina Robaa and Berin Karaman are thanked for their helpful comments on previous versions of this thesis.

Furthermore, I like to thank Prof. Dr. Manfred Jung, Benjamin Maurer, Theresa Nowak, Martin Pannek, Prof. Dr. Clemens Steegborn and Prof. Dr. Mike Schutkowski for providing us with experimental data and for many fruitful discussions on Sirtuin research. I am grateful to Prof. Dr. Gerhard Wolber for giving me the opportunity to work on an interesting project at his group in Berlin. I also owe my sincere thanks to Prof. Dr. Ivo Große for examining this thesis. For financial support I thank Deutsche Forschungsgemeinschaft (DFG).

Last but not least, I like to thank my family, especially my wife Claudia for her love, patience and understanding, that I have spent many evenings in front of the computer.

Bibliography

[1] Christopher T Walsh, Sylvie Garneau-Tsodikova, and Gregory J Gatto. Protein posttranslational modifications: the chemistry of proteome diversifications. *Angew. Chem. Int. Ed. Engl.*, 44(45):7342–72, December 2005. doi: 10.1002/anie.200501023.

[2] Francois-Xavier Theillet, Caroline Smet-Nocca, Stamatios Liokatis, Rossukon Thongwichian, Jonas Kosten, Mi-Kyung Yoon, Richard W Kriwacki, Isabelle Landrieu, Guy Lippens, and Philipp Selenko. Cell signaling, post-translational protein modifications and NMR spectroscopy. *J. Biomol. NMR*, 54(3):217–36, November 2012. doi: 10.1007/s10858-012-9674-x.

[3] O Hayaishi and K Ueda. Poly(ADP-ribose) and ADP-ribosylation of proteins. *Annu. Rev. Biochem.*, 46:95–116, 1977. doi: 10.1146/annurev.bi.46.070177.000523.

[4] Alexander Bürkle. Poly(ADP-ribose). The most elaborate metabolite of NAD+. *FEBS J.*, 272(18):4576–89, September 2005. doi: 10.1111/j.1742-4658.2005.04864. x.

[5] Go-Woon Kim and Xiang-Jiao Yang. Comprehensive lysine acetylomes emerging from bacteria to humans. *Trends Biochem. Sci.*, 36(4):211–20, April 2011. doi: 10.1016/j.tibs.2010.10.001.

[6] Gregory R Wagner and R Mark Payne. Widespread and enzyme-independent N?-acetylation and N?-succinylation of proteins in the chemical conditions of the mitochondrial matrix. *J. Biol. Chem.*, 288(40):29036–45, October 2013. doi: 10.1074/jbc.M113.486753.

[7] Chunaram Choudhary, Chanchal Kumar, Florian Gnad, Michael L Nielsen, Michael Rehman, Tobias C Walther, Jesper V Olsen, and Matthias Mann. Lysine acetylation targets protein complexes and co-regulates major cellular functions. *Science*, 325(5942):834–40, August 2009. doi: 10.1126/science.1175371.

[8] Shimin Zhao, Wei Xu, Wenqing Jiang, Wei Yu, Yan Lin, Tengfei Zhang, Jun Yao, Li Zhou, Yaxue Zeng, Hong Li, Yixue Li, Jiong Shi, Wenlin An, Susan M Hancock, Fuchu He, Lunxiu Qin, Jason Chin, Pengyuan Yang, Xian Chen, Qunying Lei, Yue Xiong, and Kun-Liang Guan. Regulation of cellular metabolism

by protein lysine acetylation. *Science*, 327(5968):1000–4, February 2010. doi: 10.1126/science.1179689.

[9] Chao Peng, Zhike Lu, Zhongyu Xie, Zhongyi Cheng, Yue Chen, Minjia Tan, Hao Luo, Yi Zhang, Wendy He, Ke Yang, Bernadette M M Zwaans, Daniel Tishkoff, Linh Ho, David Lombard, Tong-Chuan He, Junbiao Dai, Eric Verdin, Yang Ye, and Yingming Zhao. The first identification of lysine malonylation substrates and its regulatory enzyme. *Mol. Cell Proteomics*, 10(12):M111.012658, December 2011. doi: 10.1074/mcp.M111.012658.

[10] Zhihong Zhang, Minjia Tan, Zhongyu Xie, Lunzhi Dai, Yue Chen, and Yingming Zhao. Identification of lysine succinylation as a new post-translational modification. *Nat. Chem. Biol.*, 7(1):58–63, January 2011. doi: 10.1038/nchembio.495.

[11] Brian T Weinert, Christian Schölz, Sebastian A Wagner, Vytautas Iesmantavicius, Dan Su, Jeremy A Daniel, and Chunaram Choudhary. Lysine succinylation is a frequently occurring modification in prokaryotes and eukaryotes and extensively overlaps with acetylation. *Cell Rep*, 4(4):842–51, August 2013. doi: 10.1016/j. celrep.2013.07.024.

[12] Minjia Tan, Chao Peng, Kristin A Anderson, Peter Chhoy, Zhongyu Xie, Lunzhi Dai, Jeongsoon Park, Yue Chen, He Huang, Yi Zhang, Jennifer Ro, Gregory R Wagner, Michelle F Green, Andreas S Madsen, Jessica Schmiesing, Brett S Peterson, Guofeng Xu, Olga R Ilkayeva, Michael J Muehlbauer, Thomas Braulke, Chris Mühlhausen, Donald S Backos, Christian A Olsen, Peter J McGuire, Scott D Pletcher, David B Lombard, Matthew D Hirschey, and Yingming Zhao. Lysine Glutarylation Is a Protein Posttranslational Modification Regulated by SIRT5. *Cell Metab.*, 19(4):605–17, April 2014. doi: 10.1016/j.cmet.2014.03.014.

[13] Woon Ki Paik, David Pearson, Hyang Woo Lee, and Sangduk Kim. Nonenzymatic acetylation of histones with acetyl-CoA. *Biochimica et Biophysica Acta (BBA) - Nucleic Acids and Protein Synthesis*, 213(2):513–522, 1970. ISSN 0005-2787. doi: 10.1016/0005-2787(70)90058-4. URL `http://www.sciencedirect.com/science/article/pii/0005278770900584`.

[14] Weihai Ying. NAD+ and NADH in cellular functions and cell death. *Front. Biosci.*, 11:3129–48, 2006.

[15] Anthony A Sauve, Cynthia Wolberger, Vern L Schramm, and Jef D Boeke. The biochemistry of sirtuins. *Annu. Rev. Biochem.*, 75:435–65, 2006. doi: 10.1146/annurev.biochem.74.082803.133500.

[16] Qing Deng and Joseph T Barbieri. Molecular mechanisms of the cytotoxicity of ADP-ribosylating toxins. *Annu. Rev. Microbiol.*, 62:271–88, 2008. doi: 10.1146/annurev.micro.62.081307.162848.

[17] Daniela Corda and Maria Di Girolamo. Functional aspects of protein mono-ADP-ribosylation. *EMBO J.*, 22(9):1953–8, May 2003. doi: 10.1093/emboj/cdg209.

[18] Kenneth P Holbourn, Clifford C Shone, and K R Acharya. A family of killer toxins. Exploring the mechanism of ADP-ribosylating toxins. *FEBS J.*, 273(20): 4579–93, October 2006. doi: 10.1111/j.1742-4658.2006.05442.x.

[19] Bradley G Stiles, Darran J Wigelsworth, Michel R Popoff, and Holger Barth. Clostridial binary toxins: iota and C2 family portraits. *Front Cell Infect Microbiol*, 1:11, 2011. doi: 10.3389/fcimb.2011.00011.

[20] Klaus Aktories, Alexander E Lang, Carsten Schwan, and Hans G Mannherz. Actin as target for modification by bacterial protein toxins. *FEBS J.*, 278(23):4526–43, December 2011. doi: 10.1111/j.1742-4658.2011.08113.x.

[21] Carsten Schwan, Bärbel Stecher, Tina Tzivelekidis, Marco van Ham, Manfred Rohde, Wolf-Dietrich Hardt, Jürgen Wehland, and Klaus Aktories. Clostridium difficile toxin CDT induces formation of microtubule-based protrusions and increases adherence of bacteria. *PLoS Pathog.*, 5(10):e1000626, October 2009. doi: 10.1371/journal.ppat.1000626.

[22] Martin Vogelsgesang, Alexander Pautsch, and Klaus Aktories. C3 exoenzymes, novel insights into structure and action of Rho-ADP-ribosylating toxins. *Naunyn Schmiedebergs Arch. Pharmacol.*, 374(5-6):347–60, February 2007. doi: 10.1007/s00210-006-0113-y.

[23] B D Spangler. Structure and function of cholera toxin and the related Escherichia coli heat-labile enterotoxin. *Microbiol. Rev.*, 56(4):622–47, December 1992.

[24] Susan P Yates, René Jørgensen, Gregers R Andersen, and A Rod Merrill. Stealth and mimicry by deadly bacterial toxins. *Trends Biochem. Sci.*, 31(2):123–33, February 2006. doi: 10.1016/j.tibs.2005.12.007.

[25] Nathan C Simon, Klaus Aktories, and Joseph T Barbieri. Novel bacterial ADP-ribosylating toxins: structure and function. *Nat. Rev. Microbiol.*, 12(9):599–611, September 2014. doi: 10.1038/nrmicro3310.

[26] S Han, J A Craig, C D Putnam, N B Carozzi, and J A Tainer. Evolution and mechanism from structures of an ADP-ribosylating toxin and NAD complex. *Nat. Struct. Biol.*, 6(10):932–6, October 1999. doi: 10.1038/13300.

[27] Hazel R Evans, J Mark Sutton, Daniel E Holloway, Joanne Ayriss, Clifford C Shone, and K Ravi Acharya. The crystal structure of C3stau2 from Staphylococcus aureus and its complex with NAD. *J. Biol. Chem.*, 278(46):45924–30, November 2003. doi: 10.1074/jbc.M307719200.

[28] Sapan L Parikh and Vern L Schramm. Transition state structure for ADP-ribosylation of eukaryotic elongation factor 2 catalyzed by diphtheria toxin. *Biochemistry*, 43(5):1204–12, February 2004. doi: 10.1021/bi035907z.

[29] Jun Sakurai, Masahiro Nagahama, Junzo Hisatsune, Nobuhiko Katunuma, and Hideaki Tsuge. Clostridium perfringens iota-toxin, ADP-ribosyltransferase: structure and mechanism of action. *Adv. Enzyme Regul.*, 43:361–77, 2003.

[30] M Domenighini and R Rappuoli. Three conserved consensus sequences identify the NAD-binding site of ADP-ribosylating enzymes, expressed by eukaryotes, bacteria and T-even bacteriophages. *Mol. Microbiol.*, 21(4):667–74, August 1996.

[31] Daniela Corda and Maria Di Girolamo. Mono-ADP-ribosylation: a tool for modulating immune response and cell signaling. *Sci. STKE*, 2002(163):pe53, December 2002. doi: 10.1126/stke.2002.163.pe53.

[32] Paul O Hassa, Sandra S Haenni, Michael Elser, and Michael O Hottiger. Nuclear ADP-ribosylation reactions in mammalian cells: where are we today and where are we going? *Microbiol. Mol. Biol. Rev.*, 70(3):789–829, September 2006. doi: 10.1128/MMBR.00040-05.

[33] Yu-Ming Lee, C Satheesan Babu, Yao Chi Chen, Milos Milcic, Yuanyuan Qu, and Carmay Lim. Conserved structural motif for recognizing nicotinamide adenine dinucleotide in poly(ADP-ribose) polymerases and ADP-ribosylating toxins: implications for structure-based drug design. *J. Med. Chem.*, 53(10):4038–49, May 2010. doi: 10.1021/jm1001106.

[34] Mattias E Ivarsson, Jean-Christophe Leroux, and Bastien Castagner. Targeting bacterial toxins. *Angew. Chem. Int. Ed. Engl.*, 51(17):4024–45, April 2012. doi: 10.1002/anie.201104384.

[35] Dana V Ferraris. Evolution of poly(ADP-ribose) polymerase-1 (PARP-1) inhibitors. From concept to clinic. *J. Med. Chem.*, 53(12):4561–84, June 2010. doi: 10.1021/jm100012m.

[36] Zachari Turgeon, René Jørgensen, Danielle Visschedyk, Patrick R Edwards, Sarah Legree, Caroline McGregor, Robert J Fieldhouse, Dev Mangroo, Matthieu Schapira, and A Rod Merrill. Newly discovered and characterized antivirulence compounds inhibit bacterial mono-ADP-ribosyltransferase toxins. *Antimicrob. Agents Chemother.*, 55(3):983–91, March 2011. doi: 10.1128/AAC.01164-10.

[37] Athanassios Vassilopoulos, Kristofer S Fritz, Dennis R Petersen, and David Gius. The human sirtuin family: evolutionary divergences and functions. *Hum. Genomics*, 5(5):485–96, July 2011.

[38] Hong Jiang, Saba Khan, Yi Wang, Guillaume Charron, Bin He, Carlos Sebastian, Jintang Du, Ray Kim, Eva Ge, Raul Mostoslavsky, Howard C Hang, Quan Hao,

and Hening Lin. SIRT6 regulates TNF-? secretion through hydrolysis of long-chain fatty acyl lysine. *Nature*, 496(7443):110–3, April 2013. doi: 10.1038/nature12038.

[39] Shaday Michan and David Sinclair. Sirtuins in mammals: insights into their biological function. *Biochem. J.*, 404(1):1–13, May 2007. doi: 10.1042/BJ20070140.

[40] Marcia C Haigis and David A Sinclair. Mammalian sirtuins: biological insights and disease relevance. *Annu Rev Pathol*, 5:253–95, 2010. doi: 10.1146/annurev. pathol.4.110807.092250.

[41] Debra Toiber, Carlos Sebastian, and Raul Mostoslavsky. Characterization of nuclear sirtuins: molecular mechanisms and physiological relevance. *Handb Exp Pharmacol*, 206:189–224, 2011. doi: 10.1007/978-3-642-21631-2_9.

[42] Kevin Pruitt, Rebekah L Zinn, Joyce E Ohm, Kelly M McGarvey, Sung-Hae L Kang, D Neil Watkins, James G Herman, and Stephen B Baylin. Inhibition of SIRT1 reactivates silenced cancer genes without loss of promoter DNA hyperme-thylation. *PLoS Genet.*, 2(3):e40, March 2006. doi: 10.1371/journal.pgen.0020040.

[43] Eriko Michishita, Ronald A McCord, Elisabeth Berber, Mitomu Kioi, Hesed Padilla-Nash, Mara Damian, Peggie Cheung, Rika Kusumoto, Tiara L A Kawahara, J Carl Barrett, Howard Y Chang, Vilhelm A Bohr, Thomas Ried, Or Gozani, and Katrin F Chua. SIRT6 is a histone H3 lysine 9 deacetylase that modulates telomeric chromatin. *Nature*, 452(7186):492–6, March 2008. doi: 10.1038/nature06736.

[44] Matthew F Barber, Eriko Michishita-Kioi, Yuanxin Xi, Luisa Tasselli, Mitomu Kioi, Zarmik Moqtaderi, Ruth I Tennen, Silvana Paredes, Nicolas L Young, Kaifu Chen, Kevin Struhl, Benjamin A Garcia, Or Gozani, Wei Li, and Katrin F Chua. SIRT7 links H3K18 deacetylation to maintenance of oncogenic transformation. *Nature*, 487(7405):114–8, July 2012. doi: 10.1038/nature11043.

[45] Brian J North, Brett L Marshall, Margie T Borra, John M Denu, and Eric Verdin. The human Sir2 ortholog, SIRT2, is an NAD+-dependent tubulin deacetylase. *Mol. Cell*, 11(2):437–44, February 2003.

[46] Jing-Yi Huang, Matthew D Hirschey, Tadahiro Shimazu, Linh Ho, and Eric Verdin. Mitochondrial sirtuins. *Biochim. Biophys. Acta*, 1804(8):1645–51, August 2010. doi: 10.1016/j.bbapap.2009.12.021.

[47] Wenjuan He, John C Newman, Margaret Z Wang, Linh Ho, and Eric Verdin. Mitochondrial sirtuins: regulators of protein acylation and metabolism. *Trends Endocrinol. Metab.*, 23(9):467–76, September 2012. doi: 10.1016/j.tem.2012.07. 004.

[48] David B Lombard, Frederick W Alt, Hwei-Ling Cheng, Jakob Bunkenborg, Ryan S Streeper, Raul Mostoslavsky, Jennifer Kim, George Yancopoulos, David Valenzuela, Andrew Murphy, Yinhua Yang, Yaohui Chen, Matthew D Hirschey, Roderick T Bronson, Marcia Haigis, Leonard P Guarente, Robert V Farese, Sherman Weissman, Eric Verdin, and Bjoern Schwer. Mammalian Sir2 homolog SIRT3 regulates global mitochondrial lysine acetylation. *Mol. Cell. Biol.*, 27(24):8807–14, December 2007. doi: 10.1128/MCB.01636-07.

[49] David B Lombard, Daniel X Tishkoff, and Jianjun Bao. Mitochondrial sirtuins in the regulation of mitochondrial activity and metabolic adaptation. *Handb Exp Pharmacol*, 206:163–88, 2011. doi: 10.1007/978-3-642-21631-2_8.

[50] Marcia C Haigis, Raul Mostoslavsky, Kevin M Haigis, Kamau Fahie, Danos C Christodoulou, Andrew J Murphy, David M Valenzuela, George D Yancopoulos, Margaret Karow, Gil Blander, Cynthia Wolberger, Tomas A Prolla, Richard Weindruch, Frederick W Alt, and Leonard Guarente. SIRT4 inhibits glutamate dehydrogenase and opposes the effects of calorie restriction in pancreatic beta cells. *Cell*, 126(5):941–54, September 2006. doi: 10.1016/j.cell.2006.06.057.

[51] Rommel A Mathias, Todd M Greco, Adam Oberstein, Hanna G Budayeva, Rumela Chakrabarti, Elizabeth A Rowland, Yibin Kang, Thomas Shenk, and Ileana M Cristea. Sirtuin 4 is a lipoamidase regulating pyruvate dehydrogenase complex activity. *Cell*, 159(7):1615–25, December 2014. doi: 10.1016/j.cell.2014.11.046.

[52] Jintang Du, Yeyun Zhou, Xiaoyang Su, Jiu Jiu Yu, Saba Khan, Hong Jiang, Jungwoo Kim, Jimin Woo, Jun Huyn Kim, Brian Hyun Choi, Bin He, Wei Chen, Sheng Zhang, Richard A Cerione, Johan Auwerx, Quan Hao, and Hening Lin. Sirt5 is a NAD-dependent protein lysine demalonylase and desuccinylase. *Science*, 334(6057):806–9, November 2011. doi: 10.1126/science.1207861.

[53] Takashi Nakagawa, David J Lomb, Marcia C Haigis, and Leonard Guarente. SIRT5 Deacetylates carbamoyl phosphate synthetase 1 and regulates the urea cycle. *Cell*, 137(3):560–70, May 2009. doi: 10.1016/j.cell.2009.02.026.

[54] Marcia C Haigis and Leonard P Guarente. Mammalian sirtuins–emerging roles in physiology, aging, and calorie restriction. *Genes Dev.*, 20(21):2913–21, November 2006. doi: 10.1101/gad.1467506.

[55] Ramkumar Rajendran, Richa Garva, Marija Krstic-Demonacos, and Constantinos Demonacos. Sirtuins: molecular traffic lights in the crossroad of oxidative stress, chromatin remodeling, and transcription. *J. Biomed. Biotechnol.*, 2011:368276, 2011. doi: 10.1155/2011/368276.

[56] Jintang Du, Hong Jiang, and Hening Lin. Investigating the ADP-ribosyltransferase activity of sirtuins with NAD analogues and 32P-NAD. *Biochemistry*, 48(13): 2878–90, April 2009. doi: 10.1021/bi802093g.

[57] Anthony A Sauve. Sirtuin chemical mechanisms. *Biochim. Biophys. Acta*, 1804 (8):1591–603, August 2010. doi: 10.1016/j.bbapap.2010.01.021.

[58] Lei Tong and John M Denu. Function and metabolism of sirtuin metabolite O-acetyl-ADP-ribose. *Biochim. Biophys. Acta*, 1804(8):1617–25, August 2010. doi: 10.1016/j.bbapap.2010.02.007.

[59] Anthony A Sauve and Vern L Schramm. Sir2 regulation by nicotinamide results from switching between base exchange and deacetylation chemistry. *Biochemistry*, 42(31):9249–56, August 2003. doi: 10.1021/bi034959l.

[60] Brandi D Sanders, Brittany Jackson, and Ronen Marmorstein. Structural basis for sirtuin function: what we know and what we don't. *Biochim. Biophys. Acta*, 1804(8):1604–16, August 2010. doi: 10.1016/j.bbapap.2009.09.009.

[61] José L Avalos, Katherine M Bever, and Cynthia Wolberger. Mechanism of sirtuin inhibition by nicotinamide: altering the NAD(+) cosubstrate specificity of a Sir2 enzyme. *Mol. Cell*, 17(6):855–68, March 2005. doi: 10.1016/j.molcel.2005.02.022.

[62] Carlos Sebastián, F Kyle Satterstrom, Marcia C Haigis, and Raul Mostoslavsky. From sirtuin biology to human diseases: an update. *J. Biol. Chem.*, 287(51): 42444–52, December 2012. doi: 10.1074/jbc.R112.402768.

[63] Jörg Schemies, Urszula Uciechowska, Wolfgang Sippl, and Manfred Jung. NAD(+) -dependent histone deacetylases (sirtuins) as novel therapeutic targets. *Med Res Rev*, 30(6):861–89, November 2010. doi: 10.1002/med.20178.

[64] Siva Lavu, Olivier Boss, Peter J Elliott, and Philip D Lambert. Sirtuins–novel therapeutic targets to treat age-associated diseases. *Nat Rev Drug Discov*, 7(10): 841–53, October 2008. doi: 10.1038/nrd2665.

[65] Brett M Hirsch and Weiping Zheng. Sirtuin mechanism and inhibition: explored with N(ε)-acetyl-lysine analogs. *Mol Biosyst*, 7(1):16–28, January 2011. doi: 10.1039/c0mb00033g.

[66] Bin He, Jintang Du, and Hening Lin. Thiosuccinyl peptides as Sirt5-specific inhibitors. *J. Am. Chem. Soc.*, 134(4):1922–5, February 2012. doi: 10.1021/ ja2090417.

[67] Claudia Roessler, Theresa Nowak, Martin Pannek, Melanie Gertz, Giang T T Nguyen, Michael Scharfe, Ilona Born, Wolfgang Sippl, Clemens Steegborn, and Mike Schutkowski. Chemical probing of the human sirtuin 5 active site reveals its substrate acyl specificity and peptide-based inhibitors. *Angew. Chem. Int. Ed. Engl.*, 53(40):10728–32, September 2014. doi: 10.1002/anie.201402679.

[68] Takayoshi Suzuki, Keiko Imai, Hidehiko Nakagawa, and Naoki Miyata. 2-Anilinobenzamides as SIRT inhibitors. *ChemMedChem*, 1(10):1059–62, October 2006. doi: 10.1002/cmdc.200600162.

[69] J T Slama and A M Simmons. Inhibition of NAD glycohydrolase and ADP-ribosyl transferases by carbocyclic analogues of oxidized nicotinamide adenine dinucleotide. *Biochemistry*, 28(19):7688–94, September 1989.

[70] H Ota, E Tokunaga, K Chang, M Hikasa, K Iijima, M Eto, K Kozaki, M Akishita, Y Ouchi, and M Kaneki. Sirt1 inhibitor, Sirtinol, induces senescence-like growth arrest with attenuated Ras-MAPK signaling in human cancer cells. *Oncogene*, 25 (2):176–85, January 2006. doi: 10.1038/sj.onc.1209049.

[71] E Lara, A Mai, V Calvanese, L Altucci, P Lopez-Nieva, M L Martinez-Chantar, M Varela-Rey, D Rotili, A Nebbioso, S Ropero, G Montoya, J Oyarzabal, S Velasco, M Serrano, M Witt, A Villar-Garea, A Imhof, A Inhof, J M Mato, M Esteller, and M F Fraga. Salermide, a Sirtuin inhibitor with a strong cancer-specific proapoptotic effect. *Oncogene*, 28(6):781–91, February 2009. doi: 10.1038/onc.2008.436.

[72] Birgit Heltweg, Tonibelle Gatbonton, Aaron D Schuler, Jeff Posakony, Hongzhe Li, Sondra Goehle, Ramya Kollipara, Ronald A Depinho, Yansong Gu, Julian A Simon, and Antonio Bedalov. Antitumor activity of a small-molecule inhibitor of human silent information regulator 2 enzymes. *Cancer Res.*, 66(8):4368–77, April 2006. doi: 10.1158/0008-5472.CAN-05-3617.

[73] Andrew D Napper, Jeffrey Hixon, Thomas McDonagh, Kenneth Keavey, Jean-Francois Pons, Jonathan Barker, Wei Tsung Yau, Patricia Amouzegh, Adam Flegg, Estelle Hamelin, Russell J Thomas, Michael Kates, Stephen Jones, Manuel A Navia, Jeffrey O Saunders, Peter S DiStefano, and Rory Curtis. Discovery of indoles as potent and selective inhibitors of the deacetylase SIRT1. *J. Med. Chem.*, 48(25):8045–54, December 2005. doi: 10.1021/jm050522v.

[74] Xun Zhao, Dagart Allison, Bradley Condon, Feiyu Zhang, Tarun Gheyi, Aiping Zhang, Sheela Ashok, Marijane Russell, Iain MacEwan, Yuewei Qian, James A Jamison, and John Gately Luz. The 2.5 Å crystal structure of the SIRT1 catalytic domain bound to nicotinamide adenine dinucleotide (NAD+) and an indole (EX527 analogue) reveals a novel mechanism of histone deacetylase inhibition. *J. Med. Chem.*, 56(3):963–9, February 2013. doi: 10.1021/jm301431y.

[75] Johannes Trapp, Rene Meier, Darunee Hongwiset, Matthias U Kassack, Wolfgang Sippl, and Manfred Jung. Structure-activity studies on suramin analogues as inhibitors of NAD+-dependent histone deacetylases (sirtuins). *ChemMedChem*, 2 (10):1419–31, October 2007. doi: 10.1002/cmdc.200700003.

[76] Urszula Uciechowska, Jörg Schemies, Robert C Neugebauer, Elisabeth-Maria Huda, Martin L Schmitt, Rene Meier, Eric Verdin, Manfred Jung, and Wolfgang Sippl. Thiobarbiturates as sirtuin inhibitors: virtual screening, free-energy calculations, and biological testing. *ChemMedChem*, 3(12):1965–76, December 2008. doi: 10.1002/cmdc.200800104.

[77] Benjamin Maurer, Tobias Rumpf, Michael Scharfe, Diana A. Stolfa, Martin L. Schmitt, Wenjuan He, Eric Verdin, Wolfgang Sippl, and Manfred Jung. Inhibitors of the NAD+-Dependent Protein Desuccinylase and Demalonylase Sirt5. *ACS Medicinal Chemistry Letters*, 3(12):1050–1053, 2012.

[78] Jeremy S Disch, Ghotas Evindar, Cynthia H Chiu, Charles A Blum, Han Dai, Lei Jin, Eli Schuman, Kenneth E Lind, Svetlana L Belyanskaya, Jianghe Deng, Frank Coppo, Leah Aquilani, Todd L Graybill, John W Cuozzo, Siva Lavu, Cheney Mao, George P Vlasuk, and Robert B Perni. Discovery of thieno[3,2-d]pyrimidine-6-carboxamides as potent inhibitors of SIRT1, SIRT2, and SIRT3. *J. Med. Chem.*, 56(9):3666–79, May 2013. doi: 10.1021/jm400204k.

[79] T E Voogd, E L Vansterkenburg, J Wilting, and L H Janssen. Recent research on the biological activity of suramin. *Pharmacol. Rev.*, 45(2):177–203, June 1993.

[80] Konrad T Howitz, Kevin J Bitterman, Haim Y Cohen, Dudley W Lamming, Siva Lavu, Jason G Wood, Robert E Zipkin, Phuong Chung, Anne Kisielewski, Li-Li Zhang, Brandy Scherer, and David A Sinclair. Small molecule activators of sirtuins extend Saccharomyces cerevisiae lifespan. *Nature*, 425(6954):191–6, September 2003. doi: 10.1038/nature01960.

[81] Abigail H Davies, April K Roberts, Clifford C Shone, and K Ravi Acharya. Super toxins from a super bug: structure and function of Clostridium difficile toxins. *Biochem. J.*, 436(3):517–26, June 2011. doi: 10.1042/BJ20110106.

[82] K Aktories. ADP-ribosylation of actin. *J. Muscle Res. Cell. Motil.*, 11(2):95–7, April 1990.

[83] Dale N Gerding, Stuart Johnson, Maja Rupnik, and Klaus Aktories. Clostridium difficile binary toxin CDT: mechanism, epidemiology, and potential clinical importance. *Gut Microbes*, 5(1):15–27. doi: 10.4161/gmic.26854.

[84] C P Kelly and J T LaMont. Clostridium difficile infection. *Annu. Rev. Med.*, 49: 375–90, 1998. doi: 10.1146/annurev.med.49.1.375.

[85] Ferran Feixas, Steffen Lindert, William Sinko, and J Andrew McCammon. Exploring the role of receptor flexibility in structure-based drug discovery. *Biophys. Chem.*, 186:31–45, February 2014. doi: 10.1016/j.bpc.2013.10.007.

[86] Tiejun Cheng, Qingliang Li, Zhigang Zhou, Yanli Wang, and Stephen H Bryant. Structure-based virtual screening for drug discovery: a problem-centric review. *AAPS J*, 14(1):133–41, March 2012. doi: 10.1208/s12248-012-9322-0.

[87] Amit Sundriyal, April K Roberts, Clifford C Shone, and K Ravi Acharya. Structural basis for substrate recognition in the enzymatic component of ADP-ribosyltransferase toxin CDTa from Clostridium difficile. *J. Biol. Chem.*, 284(42): 28713–9, October 2009. doi: 10.1074/jbc.M109.043018.

[88] I Gülke, G Pfeifer, J Liese, M Fritz, F Hofmann, K Aktories, and H Barth. Characterization of the enzymatic component of the ADP-ribosyltransferase toxin CDTa from Clostridium difficile. *Infect. Immun.*, 69(10):6004–11, October 2001. doi: 10.1128/IAI.69.10.6004-6011.2001.

[89] Martin Vogelsgesang and Klaus Aktories. Exchange of glutamine-217 to glutamate of Clostridium limosum exoenzyme C3 turns the asparagine-specific ADP-ribosyltransferase into an arginine-modifying enzyme. *Biochemistry*, 45(3): 1017–25, January 2006. doi: 10.1021/bi052253g.

[90] Martin Karplus and J Andrew McCammon. Molecular dynamics simulations of biomolecules. *Nat. Struct. Biol.*, 9(9):646–52, September 2002. doi: 10.1038/nsb0902-646.

[91] Julie Ménétrey, Gilles Flatau, Patrice Boquet, André Ménez, and Enrico A Stura. Structural basis for the NAD-hydrolysis mechanism and the ARTT-loop plasticity of C3 exoenzymes. *Protein Sci.*, 17(5):878–86, May 2008. doi: 10.1110/ps.073398508.

[92] Paul E. Smith and John J. Tanner. Conformations of nicotinamide adenine dinucleotide (NAD+) in various environments. *Journal of Molecular Recognition*, 13(1):27–34, 2000. ISSN 1099-1352. doi: 10.1002/(SICI)1099-1352(200001/02)13: 1<27::AID-JMR483>3.0.CO;2-8. URL `http://dx.doi.org/10.1002/(SICI)`
`1099-1352(200001/02)13:1<27::AID-JMR483>3.0.CO`.

[93] Gopi Kuppuraj, Karen Sargsyan, Yun-Hao Hua, A Rod Merrill, and Carmay Lim. Linking distinct conformations of nicotinamide adenine dinucleotide with protein fold/function. *J Phys Chem B*, 115(24):7932–9, June 2011. doi: 10.1021/jp1118663.

[94] M G Rossmann, D Moras, and K W Olsen. Chemical and biological evolution of nucleotide-binding protein. *Nature*, 250(463):194–9, July 1974.

[95] M Karplus and J A McCammon. Dynamics of proteins: elements and function. *Annu. Rev. Biochem.*, 52:263–300, 1983. doi: 10.1146/annurev.bi.52.070183.001403.

[96] S Parthasarathy and M R Murthy. Analysis of temperature factor distribution in high-resolution protein structures. *Protein Sci.*, 6(12):2561–7, December 1997. doi: 10.1002/pro.5560061208.

[97] Hideaki Tsuge, Masahiro Nagahama, Masataka Oda, Shinobu Iwamoto, Hiroko Utsunomiya, Victor E Marquez, Nobuhiko Katunuma, Mugio Nishizawa, and Jun Sakurai. Structural basis of actin recognition and arginine ADP-ribosylation by Clostridium perfringens iota-toxin. *Proc. Natl. Acad. Sci. U.S.A.*, 105(21): 7399–404, May 2008. doi: 10.1073/pnas.0801215105.

[98] Seungil Han and John A Tainer. The ARTT motif and a unified structural understanding of substrate recognition in ADP-ribosylating bacterial toxins and eukaryotic ADP-ribosyltransferases. *Int. J. Med. Microbiol.*, 291(6-7):523–9, February 2002.

[99] Yaakov Levy and José N Onuchic. Water mediation in protein folding and molecular recognition. *Annu Rev Biophys Biomol Struct*, 35:389–415, 2006. doi: 10.1146/annurev.biophys.35.040405.102134.

[100] P J Goodford. A computational procedure for determining energetically favorable binding sites on biologically important macromolecules. *J. Med. Chem.*, 28(7): 849–57, July 1985.

[101] Sérgio Filipe Sousa, Pedro Alexandrino Fernandes, and Maria João Ramos. Protein–ligand docking: Current status and future challenges. *Proteins: Structure, Function, and Bioinformatics*, 65(1):15–26, 2006. ISSN 1097-0134. doi: 10.1002/prot.21082. URL http://dx.doi.org/10.1002/prot.21082.

[102] Benjamin Maurer. *Development of fluorescence-based In-vitro assays for identifying inhibitors of NAD+- dependent enzymes using Clostridium difficile transferase and Sirt5 as model enzymes.* PhD thesis, 2013.

[103] Nadine Homeyer and Holger Gohlke. Free Energy Calculations by the Molecular Mechanics Poisson?Boltzmann Surface Area Method. *Molecular Informatics*, 31(2):114–122, 2012. ISSN 1868-1751. doi: 10.1002/minf.201100135. URL http://dx.doi.org/10.1002/minf.201100135.

[104] Xiumei Guo, Mehmet Kesimer, Gökhan Tolun, Xunhai Zheng, Qing Xu, Jing Lu, John K Sheehan, Jack D Griffith, and Xiaoling Li. The NAD(+)-dependent protein deacetylase activity of SIRT1 is regulated by its oligomeric status. *Sci Rep*, 2:640, 2012. doi: 10.1038/srep00640.

[105] Yeyun Zhou, Hongmin Zhang, Bin He, Jintang Du, Hening Lin, Richard A Cerione, and Quan Hao. The bicyclic intermediate structure provides insights into the desuccinylation mechanism of human sirtuin 5 (SIRT5). *J. Biol. Chem.*, 287(34): 28307–14, August 2012. doi: 10.1074/jbc.M112.384511.

[106] Yawei Shi, Yanzi Zhou, Shenglong Wang, and Yingkai Zhang. Sirtuin Deacetylation Mechanism and Catalytic Role of the Dynamic Cofactor Binding Loop. *J Phys Chem Lett*, 4(3):491–495, February 2013. doi: 10.1021/jz302015s.

[107] Ahlia N Khan and Peter N Lewis. Unstructured conformations are a substrate requirement for the Sir2 family of NAD-dependent protein deacetylases. *J. Biol. Chem.*, 280(43):36073–8, October 2005. doi: 10.1074/jbc.M508247200.

[108] Christine Schlicker, Melanie Gertz, Panagiotis Papatheodorou, Barbara Kachholz, Christian F W Becker, and Clemens Steegborn. Substrates and regulation mechanisms for the human mitochondrial sirtuins Sirt3 and Sirt5. *J. Mol. Biol.*, 382(3): 790–801, October 2008. doi: 10.1016/j.jmb.2008.07.048.

[109] Anja Schuetz, Jinrong Min, Tatiana Antoshenko, Chia-Lin Wang, Abdellah Allali-Hassani, Aiping Dong, Peter Loppnau, Masoud Vedadi, Alexey Bochkarev, Rolf Sternglanz, and Alexander N Plotnikov. Structural basis of inhibition of the human NAD+-dependent deacetylase SIRT5 by suramin. *Structure*, 15(3):377–89, March 2007. doi: 10.1016/j.str.2007.02.002.

[110] Sébastien Moniot, Mike Schutkowski, and Clemens Steegborn. Crystal structure analysis of human Sirt2 and its ADP-ribose complex. *J. Struct. Biol.*, 182(2): 136–43, May 2013. doi: 10.1016/j.jsb.2013.02.012.

[111] Lei Jin, Wentao Wei, Yaobin Jiang, Hao Peng, Jianhua Cai, Chen Mao, Han Dai, Wendy Choy, Jean E Bemis, Michael R Jirousek, Jill C Milne, Christoph H Westphal, and Robert B Perni. Crystal structures of human SIRT3 displaying substrate-induced conformational changes. *J. Biol. Chem.*, 284(36):24394–405, September 2009. doi: 10.1074/jbc.M109.014928.

[112] Lars Skjaerven, Nathalie Reuter, and Aurora Martinez. Dynamics, flexibility and ligand-induced conformational changes in biological macromolecules: a computational approach. *Future Med Chem*, 3(16):2079–100, December 2011. doi: 10.4155/fmc.11.159.

[113] Donald Hamelberg, John Mongan, and J Andrew McCammon. Accelerated molecular dynamics: a promising and efficient simulation method for biomolecules. *J Chem Phys*, 120(24):11919–29, June 2004. doi: 10.1063/1.1755656.

[114] Levi C T Pierce, Romelia Salomon-Ferrer, Cesar Augusto F de Oliveira, J Andrew McCammon, and Ross C Walker. Routine Access to Millisecond Time Scale Events with Accelerated Molecular Dynamics. *J Chem Theory Comput*, 8(9): 2997–3002, September 2012. doi: 10.1021/ct300284c.

[115] Zheng Yuan, Timothy L Bailey, and Rohan D Teasdale. Prediction of protein B-factor profiles. *Proteins*, 58(4):905–12, March 2005. doi: 10.1002/prot.20375.

[116] I Luque and E Freire. Structural stability of binding sites: consequences for binding affinity and allosteric effects. *Proteins*, Suppl 4:63–71, 2000.

[117] A Amadei, A B Linssen, and H J Berendsen. Essential dynamics of proteins. *Proteins*, 17(4):412–25, December 1993. doi: 10.1002/prot.340170408.

[118] Thomas Schindler, William Bornmann, Patricia Pellicena, W. Todd Miller, Bayard Clarkson, and John Kuriyan. Structural Mechanism for STI-571 Inhibition of Abelson Tyrosine Kinase. *Science*, 289(5486):1938–1942, 2000. doi: 10.1126/

science.289.5486.1938. URL `http://www.sciencemag.org/content/289/5486/1938.abstract`.

[119] José L Avalos, Jef D Boeke, and Cynthia Wolberger. Structural basis for the mechanism and regulation of Sir2 enzymes. *Mol. Cell*, 13(5):639–48, March 2004.

[120] Julien Michel, Julian Tirado-Rives, and William L Jorgensen. Energetics of displacing water molecules from protein binding sites: consequences for ligand optimization. *J. Am. Chem. Soc.*, 131(42):15403–11, October 2009. doi: 10.1021/ja906058w.

[121] Dmitrii Beglov and Benoît Roux. An integral equation to describe the solvation of polar molecules in liquid water. *The Journal of Physical Chemistry B*, 101(39): 7821–7826, 1997.

[122] Daniel J. Sindhikara, Norio Yoshida, and Fumio Hirata. Placevent: An algorithm for prediction of explicit solvent atom distribution—Application to HIV-1 protease and F-ATP synthase. *Journal of Computational Chemistry*, 33(18):1536–1543, 2012. ISSN 1096-987X. doi: 10.1002/jcc.22984. URL `http://dx.doi.org/10.1002/jcc.22984`.

[123] Maxim Totrov and Ruben Abagyan. Flexible ligand docking to multiple receptor conformations: a practical alternative. *Curr. Opin. Struct. Biol.*, 18(2):178–84, April 2008. doi: 10.1016/j.sbi.2008.01.004.

[124] David Weininger et al. SMARTS - A Language for Describing Molecular Patterns. *Daylight Chemical Information Systems, Inc*, PO Box 7737, Laguna Niguel, CA 92677.

[125] John J. Irwin and Brian K. Shoichet. ZINC - A Free Database of Commercially Available Compounds for Virtual Screening. *Journal of Chemical Information and Modeling*, 45(1):177–182, 2005. URL `http://dblp.uni-trier.de/db/journals/jcisd/jcisd45.html#IrwinS05;http://dx.doi.org/10.1021/ci049714;http://www.bibsonomy.org/bibtex/25d1da6e4c1da975cd44aaab785ad5c25/dblp`.

[126] Nidhi Ahuja, Bjoern Schwer, Stefania Carobbio, David Waltregny, Brian J North, Vincenzo Castronovo, Pierre Maechler, and Eric Verdin. Regulation of insulin secretion by SIRT4, a mitochondrial ADP-ribosyltransferase. *J. Biol. Chem.*, 282 (46):33583–92, November 2007. doi: 10.1074/jbc.M705488200.

[127] Gaëlle Laurent, Natalie J German, Asish K Saha, Vincent C J de Boer, Michael Davies, Timothy R Koves, Noah Dephoure, Frank Fischer, Gina Boanca, Bhavapriya Vaitheesvaran, Scott B Lovitch, Arlene H Sharpe, Irwin J Kurland, Clemens Steegborn, Steven P Gygi, Deborah M Muoio, Neil B Ruderman, and Marcia C Haigis. SIRT4 coordinates the balance between lipid synthesis and

catabolism by repressing malonyl CoA decarboxylase. *Mol. Cell*, 50(5):686–98, June 2013. doi: 10.1016/j.molcel.2013.05.012.

[128] Linh Ho, Allen Sam Titus, Kushal Kr Banerjee, Suji George, Wei Lin, Shaunak Deota, Asish K Saha, Ken Nakamura, Philipp Gut, Eric Verdin, and Ullas Kolthur-Seetharam. SIRT4 regulates ATP homeostasis and mediates a retrograde signaling via AMPK. *Aging (Albany NY)*, 5(11):835–49, November 2013.

[129] Seung Min Jeong, Cuiying Xiao, Lydia W S Finley, Tyler Lahusen, Amanda L Souza, Kerry Pierce, Ying-Hua Li, Xiaoxu Wang, Gaëlle Laurent, Natalie J German, Xiaoling Xu, Cuiling Li, Rui-Hong Wang, Jaewon Lee, Alfredo Csibi, Richard Cerione, John Blenis, Clary B Clish, Alec Kimmelman, Chu-Xia Deng, and Marcia C Haigis. SIRT4 has tumor-suppressive activity and regulates the cellular metabolic response to DNA damage by inhibiting mitochondrial glutamine metabolism. *Cancer Cell*, 23(4):450–63, April 2013. doi: 10.1016/j.ccr.2013.02.024.

[130] Torsten Schwede, Jürgen Kopp, Nicolas Guex, and Manuel C Peitsch. SWISS-MODEL: An automated protein homology-modeling server. *Nucleic Acids Res.*, 31(13):3381–5, July 2003.

[131] Yang Zhang. I-TASSER server for protein 3D structure prediction. *BMC Bioinformatics*, 9:40, 2008. doi: 10.1186/1471-2105-9-40.

[132] S F Altschul, W Gish, W Miller, E W Myers, and D J Lipman. Basic local alignment search tool. *J. Mol. Biol.*, 215(3):403–10, October 1990. doi: 10.1016/S0022-2836(05)80360-2.

[133] Johannes Söding. Protein Homology Detection by HMM–HMM Comparison. *Bioinformatics*, 21(7):951–960, April 2005. ISSN 1367-4803. doi: 10.1093/bioinformatics/bti125. URL http://dx.doi.org/10.1093/bioinformatics/bti125.

[134] Valerio Mariani, Florian Kiefer, Tobias Schmidt, Juergen Haas, and Torsten Schwede. Assessment of template based protein structure predictions in CASP9. *Proteins*, 79 Suppl 10:37–58, 2011. doi: 10.1002/prot.23177.

[135] R A Frye. Phylogenetic classification of prokaryotic and eukaryotic Sir2-like proteins. *Biochem. Biophys. Res. Commun.*, 273(2):793–8, July 2000. doi: 10.1006/bbrc.2000.3000.

[136] A Sali and T L Blundell. Comparative protein modelling by satisfaction of spatial restraints. *J. Mol. Biol.*, 234(3):779–815, December 1993. doi: 10.1006/jmbi.1993.1626.

[137] Ian W. Davis, Laura Weston Murray, Jane S. Richardson, and David C. Richardson. MOLPROBITY: structure validation and all-atom contact analysis

for nucleic acids and their complexes. *Nucleic Acids Research*, 32(Web-Server-Issue):615–619, 2004. URL `http://dblp.uni-trier.de/db/journals/nar/nar32.html#DavisMRR04;http://dx.doi.org/10.1093/nar/gkh398;http://www.bibsonomy.org/bibtex/23cf05e2027ea6bba3769df382337eb3b/dblp`.

[138] Pascal Benkert, Silvio C E Tosatto, and Dietmar Schomburg. QMEAN: A comprehensive scoring function for model quality assessment. *Proteins*, 71(1):261–77, April 2008. doi: 10.1002/prot.21715.

[139] Molecular Operating Environment (MOE 2013.08). *Chemical Computing Group Inc.*, 1010 Sherbooke St. West, Suite #910, Montreal, QC, Canada.

[140] R Development Core Team. *R: A Language and Environment for Statistical Computing*. R Foundation for Statistical Computing, Vienna, Austria, 2009. URL `http://www.R-project.org`. ISBN 3-900051-07-0.

[141] Gareth Jones, Peter Willett, and Robert C. Glen. Molecular recognition of receptor sites using a genetic algorithm with a description of desolvation. *Journal of Molecular Biology*, 245(1):43–53, 1995. ISSN 0022-2836. doi: 10.1016/S0022-2836(95)80037-9. URL `http://www.sciencedirect.com/science/article/pii/S0022283695800379`.

[142] D.A. Case, T.A. Darden, T.E. Cheatham, C.L. Simmerling, J. Wang, R.E. Duke, R. Luo, R.C. Walker, W. Zhang, K.M. Merz, B. Roberts, S. Hayik, A. Roitberg, G. Seabra, J. Swails, A.W. Goetz, I. Kolossváry, K.F. Wong, F. Paesani, J. Vanicek, R.M. Wolf, J. Liu, X. Wu, S.R. Brozell, T. Steinbrecher, H. Gohlke, Q. Cai, X. Ye, J. Wang, M.J. Hsieh, G. Cui, D.R. Roe, D.H. Mathews, M.G. Seetin, R. Salomon-Ferrer, C. Sagui, V. Babin, T. Luchko, S. Gusarov, A. Kovalenko, and P.A. Kollman. Amber12 and AmberTools13. *University of California, San Francisco*, 2012.

[143] U K Laemmli. Cleavage of structural proteins during the assembly of the head of bacteriophage T4. *Nature*, 227(5259):680–5, August 1970.

[144] Andrew M Waterhouse, James B Procter, David M A Martin, Michèle Clamp, and Geoffrey J Barton. Jalview Version 2–a multiple sequence alignment editor and analysis workbench. *Bioinformatics*, 25(9):1189–91, May 2009. doi: 10.1093/bioinformatics/btp033.

[145] Noel O'Boyle, Michael Banck, Craig James, Chris Morley, Tim Vandermeersch, and Geoffrey Hutchison. Open Babel: An open chemical toolbox. *Journal of Cheminformatics*, 3(1):33, 2011. ISSN 1758-2946. doi: 10.1186/1758-2946-3-33. URL `http://www.jcheminf.com/content/3/1/33;http://www.bibsonomy.org/bibtex/2cdae3e666b59e32307a3bb8796381622/rlanger`.

[146] Daniel R. Roe and Thomas E. Cheatham. PTRAJ and CPPTRAJ: Software for Processing and Analysis of Molecular Dynamics Trajectory Data. *Journal of*

Chemical Theory and Computation, 9(7):3084–3095, 2013. doi: 10.1021/ct400341p. URL `http://dx.doi.org/10.1021/ct400341p`.

[147] Bill R. Miller, T. Dwight McGee, Jason M. Swails, Nadine Homeyer, Holger Gohlke, and Adrian E. Roitberg. MMPBSA.py: An Efficient Program for End-State Free Energy Calculations. *Journal of Chemical Theory and Computation*, 8(9):3314–3321, 2012. doi: 10.1021/ct300418h. URL `http://dx.doi.org/10.1021/ct300418h`.

[148] Alexey Onufriev, Donald Bashford, and David A Case. Exploring protein native states and large-scale conformational changes with a modified generalized born model. *Proteins*, 55(2):383–94, May 2004. doi: 10.1002/prot.20033.

[149] Zhan Deng, Claudio Chuaqui, and Juswinder Singh. Structural interaction fingerprint (SIFt): a novel method for analyzing three-dimensional protein-ligand binding interactions. *J. Med. Chem.*, 47(2):337–44, January 2004. doi: 10.1021/jm030331x.

[150] OEChem, OpenEye Scientific Software. *OpenEye Scientific Software, Inc.*, Santa Fe, NM, USA, 2010.

[151] KarenT. Schomburg, Katrin Stierand, and Matthias Rarey. Visualisierung komplexer, molekularer Zusammenhänge. *BIOspektrum*, 19(2):146–148. ISSN 0947-0867. doi: 10.1007/s12268-013-0285-1. URL `http://dx.doi.org/10.1007/s12268-013-0285-1`.

[152] Andreas Bender, Hamse Y. Mussa, Robert C. Glen, and Stephan Reiling. Similarity Searching of Chemical Databases Using Atom Environment Descriptors (MOLPRINT 2D): Evaluation of Performance. *Journal of Chemical Information and Computer Sciences*, 44(5):1708–1718, 2004. doi: 10.1021/ci0498719. URL `http://dx.doi.org/10.1021/ci0498719`. PMID: 15446830.

[153] UniProt: a hub for protein information. *Nucleic Acids Res.*, 43(Database issue):D204–12, January 2015. doi: 10.1093/nar/gku989.

List of Figures

List of Tables

List of Abbreviations

ADP Adenosine diphosphate

ADPR ADP-ribose

ADPRT ADP-ribosyltransferase

AR Adenosine riboside

ARTT ADP-ribosylating turn-turn (loop)

CDT *Clostridium difficile* transferase

CPS1 Carbamoyl phosphate synthetase 1

CR Caloric restriction

CDT *Vibrio cholerae* toxin

DT *Corynebacterium diphtheriae* toxin

EF2 Elongation factor 2

$ENAD^+$ Etheno-NAD^+

GDH Glutamate dehydrogenase

GTP Guanosintriphosphat

HPLC High-performance liquid chromatography

IC_{50} Concentration of inhibitor that reduced the enzymatic activity by 50%

KAT Lysine acetyltransferases

KDAC Lysine deacetylases

MD Molecular dynamics

NA Nicotinic acid

NAD^+ Nicotinamide adenine dinucleotide

NAM Nicotinamide

n.d. not determined

n.i. no inhibition

NMN Nicotinamide mononucleotide

NR Nicotinamide riboside

OAADPR O-acyl-ADPR

SBVS Structure-based virtual screening

Sirt Sirtuin; Silent mating type information regulation 2 homolog

SMARTS Smiles arbitrary target specification

PARP Poly-(ADP-ribose) polymerase

PCA Principle components analysis

PDB Protein Data Bank (RCSB)

PNAD$^+$ 8-pyrrolyl-NAD$^+$

PTM Posttranslational modification

RMSD Root-mean-square deviation

APPENDIX A

Modeling Studies on *Clostridium Difficile* Binary Toxin

A.1 Hardware and Software

All Figures of proteins or protein-ligand models were produced by the molecular modeling software MOE 2012.10[139]. Marvin Sketch* was used for drawing chemical structures, substructures and reactions and plots were generated with the statistical software R[140]. In general, molecular docking was carried out using Gold 5.1[141] and Amber 12[142] was used for MD simulations. All computational tasks were carried out either on a standard personal computer or on the University cluster *thot*.

A.2 Protein Structures

PDB Code	Protein	Ligand	Resolution	PDB Code	Protein	Ligand	Resolution
2WN4	CDTa		1.85 Å	1OJZ	C3-stau	NAD$^+$	2.02 Å
2WN5	CDTa		1.90 Å	1OJQ	C3-stau		1.68 Å
2WN6	CDTa	NADP$^+$	1.96 Å	1GZF	C3-bot	NAD$^+$	1.95 Å
2WN7	CDTa	NAD$^+$	2.25 Å	1G24	C3-bot		1.70 Å
2WN8	CDTa		2.00 Å	2A5F	CT	NAD$^+$	2.02 Å
1GIQ	Iota	NADH	1.80 Å	3Q9O	Cholix-A	NAD$^+$	1.79 Å
1GIR	Iota	NADPH	2.10 Å	1TOX	DT	NAD$^+$	2.30 Å

Table A.1: Protein structures used for the modeling studies described in Section 2.

The structures listed in Table A.1 were downloaded from the PDB and prepared for the modeling studies described in Section 2. Missing atoms were added, partial charges were calculated and the structure was protonated using standard methods and default

---

* ChemAxon, http://www.chemaxon.com

settings of MOE 2012.10[139].

A.3 *In-vitro* Assays for CDT

Several *in-vitro* assays to detect CDT activity were established by Maurer et al. at University Freiburg[102]. However, most of the compounds discussed in this work were measured using a NAD^+ conversion assay as well as a radioactive assay.

NAD^+ Conversion Assay

The assay based on the measurement of a fluorescent product that is formed by a reaction of NAD^+ with acetophenone and formic acid (see Figure A.1). 1 µM NAD^+ was incubated with 1.6 µM human (or rabbit) actin and 47 nM CDT for 45 minutes at 30°C in CDT-buffer (3 mM $MgCl_2$, 10 mM NaCl and 50 mM HEPES, pH 7.4) in a total volume of 65.5 µL containing 1 µL DMSO. The test substances were dissolved in DMSO to obtain stock solutions with a concentration of 10 mM - the screening assay concentration was 152 µM. For IC_{50} determination, an appropriate range of concentrations was used. The reaction was stopped with 20 µL KOH and 20 µL acetophenone solution (20% v/v in EtOH) after an incubation time of 20 minutes on ice. 90 µL formic acid was added and the plates were heated for 5 minutes at 95°C on an Abimed Digital Dry Bath. The fluorescence intensity was measured, after cooling down on ice, in a PolarStar Optima plate reader ($\lambda Ex=340nm$ and $\lambda Em=450nm$).
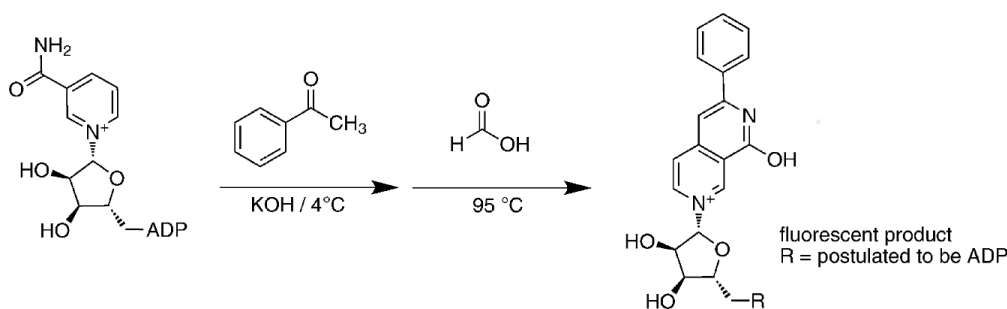
Figure A.1: Conversion of NAD^+ into a fluorescent compound upon reaction with acetophenone and formic acid.

Radioactive Assay

750 nM non-muscle human actin was incubated with 1 µM [^{32}P]NAD^+, 100 µM NAD^+ and 150 nM CDT for 10 minutes at 37°C in the presence of 65 µM $MgCl_2$ and 50 mM HEPES (pH 7.4) in a total volume of 20 µL including 1 µL of DMSO (different concentrations of test substances covering an appropriate range for IC_{50} determination). The reaction was stopped by the addition of Laemmli buffer and heating for 5 minutes at 95°C. The samples were subsequently subjected to SDS-PAGE according to

the methods of Laemmli[143]. The rate of [32P]ADP-ribosylation of actin was measured using a Phosphor-Imager.

A.4 Sequence Alignment

The protein structures of CDT, Iota, C3-stau, C3-bot, Cholera toxin, Diphteria toxin and Cholix-A were downloaded from the PDB (codes see Table A.1) and superimposed using MOE 2012.10[139]. To guide the alignment process, constraints were defined for several highly conserved residues (see Table 2.1). The final alignment shown in Figure A.2 was visualized with Jalview[144].


```
CDT       TPNELADVNDYMRGGYTAINNYLIS-NGPVNNPNPELDSKITNIENALKREPIPTNLTVYRRSGP-----------QEFGLT
Iota      TPNELADVNDYMRGGYTAINNYLIS-NGPLNNPNPELDSKVNNIENALKLTPIPSNLIVYRRSGP-----------QEFGLT
C3-bot    SKSEKEAIVSYTKSA-SEINGKLRQNKGVINGFPSNLIKQVELLDKSFNKMKTPENIMLFRGDDPAYLG------TEFQNT
C3-stau   SSKDKMAIYNYTKNS-SPINTPLRSANGDVNKLSENIQEQVRQLDSTISKSVTPDSVYVYRLLNLDYLSSITGFTREDLHML
CT        ------------------------------------------------------DKLYRADSRPPDEIKQSGGLMPRGQS
DT        ---MLVRGYVVSRKLFASILIGALLGIGAPPSAHAGADDVVDSSKSF-----VMENFSSYHGTK----------------
Cholix-A  ----------------GSHMAVITPQGVTNWTYQELEATHQALTRE------GYVFVGYHGTN----------------
```
                    α3-Helix   **Arom-H/R**

```
CDT       LTSPEYDFNKLENIDAFKSKWEGQALSYPNFISTSIGSVNMSAFAK----------------RKIVLRITIPKGSPGAYL
Iota      LTSPEYDFNKIENIDAFKEKWEGKVITYPNFISTSIGSVNMSAFAK----------------RKIILRINIPKDSPGAYL
C3-bot    LLNSNGTINKTA-FEKAKAKFLNKDRLEYGYISTSL--MNVSQFAG----------------RPIITKFKVAKGSKAGYI
C3-stau   QQTNNGQYNEAL-VSKLNNLMNSRIYRENGYSSTQL--VSGAALAG----------------RPIELKLELPKGTKAAYI
CT        EYFDRGTQMNINLYDHARGTQTGFVRHDDGYVSTSISLRSAHLVGQ-----------------TILSGHSTYYIYVIATAP
DT        ---PGYVDSIQKGIQKPKSGTQGNYDDDWKGFYSTDNKYDAAGYSVDNENPLSGKAGGVVKVTYPGLTKVLALKVDNAETIK
Cholix-A  HVAAQTIVNRIAPVPRGNNTENEE---KWGGLYVATHAEVAHGYARIKEGTGEYGLPTRAERDARGVMLRVYIPRASLERFY
```
                             STS   **PN-Loop**

```
CDT       SA----------------------------------IPGYAGEYEVLLNHGSKFKINKIDSYKDGTIT-KLIVDATLIP
Iota      SA----------------------------------IPGYAGEYEVLLNHGSKFKINKVDSYKDGTVT-KLILDATLIN
C3-bot    DP----------------------------------ISAFAGQLEMLLPRHSTYHIDDMRLSSDGK---QIIITATMMG
C3-stau   DSK--------------------------------ELTAYPGQQEVLLPRGTEYAVGSVKLSDNKR---KIIITAVVFK
CT        NMF---------------------------------NVNDVLGAYSPHPDDQDVSALGGIPYSQIYGWY-RVHFGVLDEQ
DT        KELGLSLTEPLMEQVGTEEFIKRFGDGASRVVLSLPFAEGSSSVFEYINNWEQAKALSVELEINFETRGKRGQDAMYEYM
Cholix-A  RTNT------PLENAEEHITQVIGHSLPLRNEAFTGPESAGGEDETVIGWDMAIHAVAIPSTIPGNAYEELAIDEEAVA
```
                                    Q/E-x-E

Figure A.2: Sequence alignment of selected ADPRTs. Highly conserved residues are colored in dark blue and weakly conserved residues in light blue.

A.5 Conformational Analysis of NAD+

The crystal structures of Sirt1 (4I5I), Sirt3 (4BV3), Sirt5 (3RIY), ADPR-cylcase (3I9K), Liver Alcohol Deydrogenase (4NFH), NAD+ Kinase (1Z0Z) and several ADPRTs listed in Table A.1 were downloaded from the PDB. The co-crystallized NAD+ molecules were extracted and all conformations were aligned by a quaternion fit as implemented in Open Babel 2.2[145]. The RMSD values to the reference conformation (NAD+ as bound to CDTa) was calculated using the *rms_analysis* tool as distributed with Gold[141]. A hierarchical clustering of all conformation using the complete linkage method was carried out with the same program.

A.6 Conformational Analysis of CDTa

A.6.1 Molecular Dynamics Simulations

Conventional MD simulation were carried out for the unbound structure of CDTa (2WN5, *MD-apo*) as well as the NAD^+ bound complex (2WN7, *MD-holo*). Both structures were prepared as described in Section A.2. Atom types and AM1-BCC charges for NAD^+ were calculated using the *antechamber* program from AmberTools 13 and both systems were parameterized using *tleap* and the parameters of the ff12SB and GAFF force field[142]. TIP3P waters as well as adequate counterions were added in a 10 Å octahedron periodic box.

Figure A.3: Cα-RMSD values of each snapshot produced by the *MD-apo* and *MD-holo* simulation of CDTa.

Each system was relaxed by an energy minimisation and heated up to 300K using the *pmemd* program from Amber 12[142]. After 200 ps, the thermodynamic properties of both systems were analyzed to check their equilibration states. The equilibrated systems were used as input for a 70 nanoseconds simulations at constant temperature (300 K) and constant pressure using the SHAKE algorithm and isotropic position scaling (Berendsen algorithm). A time step of 2 fs was used and the cutoff for vdW interactions was set to 9 Å. Electrostatic interactions were treated by the Particle Mesh ewald method and all coordinates were written to the trajectories every 10 ps. The stability of both simulations was proofed by the calculation of RMSD values for each superimposed snapshot in respect to the initial coordinates. As can be seen from Figure A.3, both systems were stable after a short equilibration phase.

A.6.2 B-Factor Analysis

B-factors obtained from crystallographic refinement were extracted from the original PDB files of all CDTa structures listed in Table A.1. An average B-factor profile was

calculated from all individual profiles and normalized to zero mean and unit variance*. Average models were calculated for both MD simulations (*MD-apo* and *MD-holo*) using the *cpptraj* program of AmberTool 13[146]. B-factores were estimated from the positional fluctuation of each Cα atom around the corresponding average position. Each B-factor profile was normalized and mapped to the normalized B-factors determined by X-ray crystallography.

A.6.3 Conformational Clustering

The trajectory of *MD-apo* simulation of CDTa was clustered using the *ptraj* program distributed with AmberTools 13[146]. All sampled conformations were aligned to an average model by a root-mean-square fit of the corresponding backbone atoms. A hierarchical clustering was carried out using the average-linkage method - the number of final clusters was set to three. For each individual cluster, the cluster centroid was extracted from the trajectory and was chosen as representative conformation for further analysis.

A.7 Detection of Conserved Water Molecules

All available structures of CDTa were superimposed with selected structures of Iota toxin, C3-bot and C3-stau (PDB codes see Table A.1). A region of 8 Å around the superimposed NAD^+ molecules were visually analyzed for conserved waters. A water was defined as conserved, if a related water exist in at least one structure of each toxin not more than 1.5 Å away from the origin location. In total, four waters were found to be conserved inside the NAD^+ pockets of CDT, Iota toxin, C3-bot and C3-stau. The B-factors of each conserved water were extracted from the origin PDB files of CDTa and normalized to zero mean unit variance. The normalized B-factors were averaged over all apo and holo structures separately.

The interaction potential of hydrophilic (*OH2*) and hydrophobic (*DRY*) groups was calculated by the GRID algorithm as implemented in MOE 2012.10[100]. The calculation was carried out for a region defined by a distance cutoff of 8 Å from each NAD^+ atom. Default energy levels were used for both GRID probes (*OH2*: -5.5 kcal/mol; *DRY*: -2.5 kcal/mol) and the obtained interaction potentials were visualized by drawing the potential maps using MOE.

---

* For details, see work of Parthasarathy et al. [96]

A.8 Docking Protocols

A.8.1 Docking of NAD$^+$ Analogs

The structures of etheno-NAD$^+$ (eNAD$^+$) and 8-pyrrolyl-NAD$^+$ (pNAD$^+$) were downloaded from Pubchem (https://pubchem.ncbi.nlm.nih.gov/) and prepared for docking by adding hydrogens and partial charges using default settings of MOE 2012.10[139]. Both compounds were docked to all cofactor bound structures of CDTa (PDB codes see Table A.1). An ensemble docking of both compounds was carried out using the docking program Gold 5.1[141]. Each cofactor was (fully flexible) docked to all cofactor bound structures of CDTa (PDB codes see Table A.1). The binding pocket was defined by the native conformation of NAD$^+$ as co-crystallized in one of CDTa structures.

To guide the conformational search, a scaffold and hydrogen bond constraint based on the nicotinamide mononucleotide moeity of native bound NAD$^+$ was applied. Goldscore was used as fitness function and the genetic algorithm was configured for a maximum search efficiency. ENAD$^+$ and pNAD$^+$ were docked 20 times to both CDTa structures and all solutions were visually analyzed for a common binding mode. The most promising poses which satisfied the desired constraints were further analyzed by a MD simulation run.

Both ligands were parameterized by calculating AM1-BCC charges using the *antechamber* program of AmberTools 13[142]. Both protein-ligand systems were configured with *tleap* using the ff12SB and GAFF force field. TIP3P waters as well as counterions were added in a 10 Å octahedron periodic box. Each system was relaxed by a min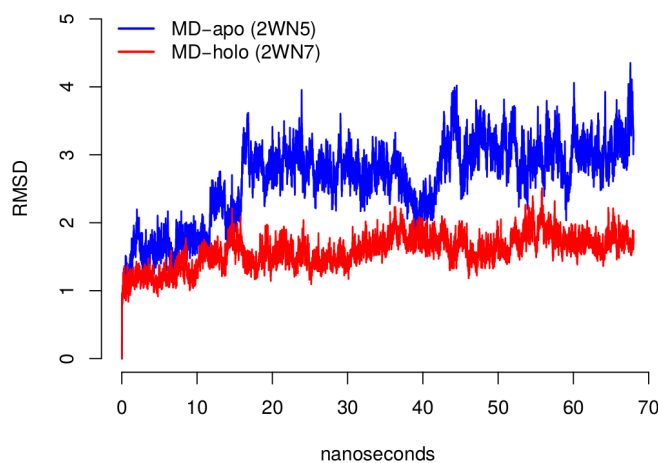imisation, heated up to 300K and equilibrated by a short simulation using the *pmemd* program of Amber 12. After 200 ps, the thermodynamic properties of both systems were analyzed to check their equilibration states. The equilibrated systems were used as input for a 10 ns simulations at constant temperature (300 K) and constant pressure using the SHAKE algorithm and isotropic position scaling (Berendsen algorithm). A time step of 2 fs was used and the cutoff for vdW interactions was set to 9 Å. Electrostatic interactions were treated by the Particle Mesh ewald method and all coordinates were written to the trajectories every 10 ps. The stability of both simulations was proofed by the calculating the RMSD value of each frame in respect to the initial coordinates (see Figure A.4). The last frame of both simulations was minimized with *pmemd* and the obtained models are shown in Figure 2.10 and Figure 2.11.

Binding free energies were approximated from the MD trajectories produced by the CDT-eNAD$^+$, CDT-pNAD$^+$ and CDT-NAD$^+$ simulations. Due to its computational efficiency, the MM/GBSA* method was used to score binding affinities. 50 equally distributed frames were extracted from the last nanosecond of each trajectory, which were equilibrated and highly stable for all three complexes (see Figure A.4). These snapshots were processed by the *MMPBSA.py* script as distributed with AmberTools 13[147]. GBSA calculations were carried out using the *igb=5* mode[148] and the results

---

*   Molecular Mechanics/Generalized Born Surface Area

shown in Table 2.4 were taken from the standard output file.
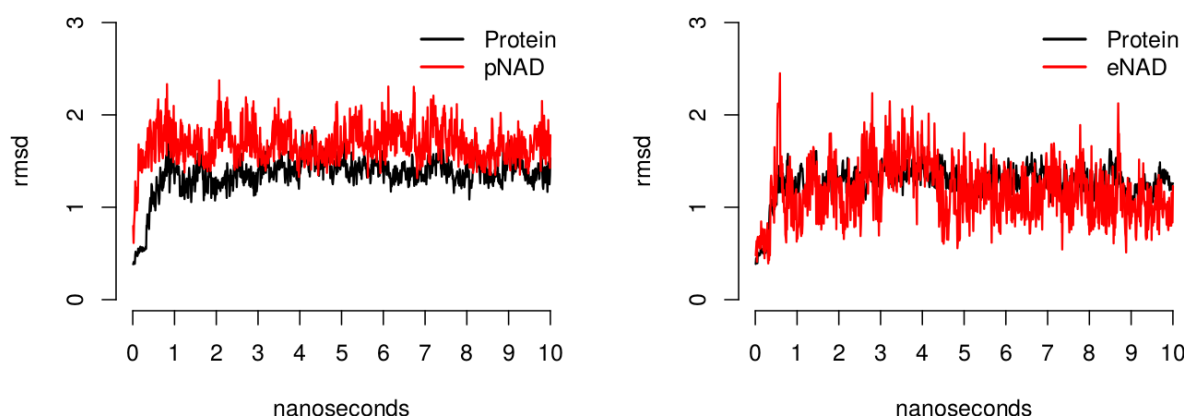
Figure A.4: RMSD values of simulated eNAD$^+$ and pNAD$^+$ binding models in respect to their initial coordinates.

A.8.2 Docking of Thiobarbiturates

ThiBe5-7 (see Figure 2.12) were build with the *Molecule Builder* as implemented in MOE 2012.10[139]. For *ThiBe5* and *Thibe7*, both isomers were generated and the potential energy of all molecules was minimized in respect to the MMFF94 force field. All prepared thiobarbiturates were docked to five different conformations of CDTa using the docking program Gold 5.1[141]. Two prepared crystal structures (2WN6 and 2WN7, see Table A.1) as well as three conformations obtained from hierarchical clustering (see Section A.6.3) were included in this ensemble of protein models.

ID	Isomer	ASP	Goldscore
ThiBe5	E	5.97	23.13
ThiBe5	Z	9.24	24.65
ThiBe6		11.82	24.42
ThiBe7	E	7.99	22.96
ThiBe7	Z	10.43	25.24

Table A.2: Docking scores for Thiobarbiturates and CDTa. The Goldscores and ASP scores were normalized by dividing the raw score by the number of heavy atoms to the power of 1/3.

Goldscore was used as fitness function for docking and ASP was used for rescoring (and optimizing) the final docking solutions. The genetic algorithm was configured for a maximum search efficiency and each thiobarbiturate was docked 20 times to all CDTa models. The top five scored solutions were visually analyzed and a common binding mode of *ThiBe5* and *ThiBe6-7* (Z-isomers) was compared with an alternative model of

ThiBe5 and *ThiBe6-7* (E-isomers). All six docking solutions were prepared for a 10 ns MD simulation using Amber 12 and an analog protocol as described in Section A.8.1. As indicated by the RMSD plots shown in Figure A.5, only the models for the Z-isomer were highly stable over the whole simulation time. Interestingly, also the docking scores obtained for the E-isomers were slightly lower than the docking scores obtained for the Z-isomer (see Table A.2).
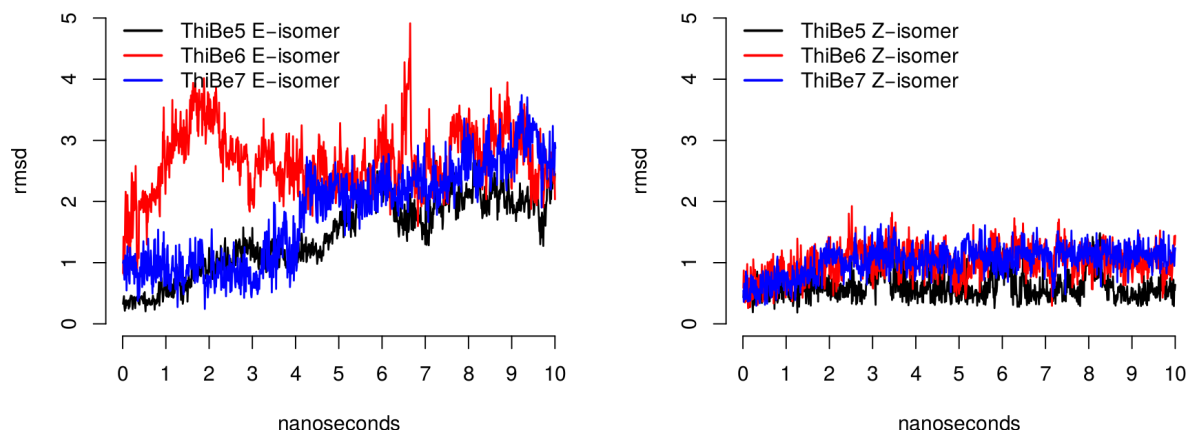
Figure A.5: RMSD plots of two simulated binding models for CDT and three thiobarbiturate. The RMSD values were measured to the corresponding initial coordinates.

The interaction potential of methyl groups was calculated by the GRID algorithm as implemented in MOE 2012.10[100]. The calculation was carried out for a region defined by a distance cutoff of 6 Å around the final pose of *ThiBe5*. Default energy levels were used and the obtained interaction potential was visualized by drawing the potential map using MOE.

A.8.3 Docking of Pyrrolidinediones

All pyrrolidinedione derivatives (*Pyro1-6*, see Figure 2.14 and Table 2.6) were build with the *Molecule Builder* as implemented in MOE 2012.10[139]. Due to two stereocenters, four cis-trans isomers were generated per compound and the conformation of all 24 molecules were optimized according to the MMFF94 force field. Each molecule was subjected to an ensemble docking using three different structures of CDTa (2WN5, 2WN6 and 2WN7, see Section A.2). Gold was configured for maximum search efficiency and Goldscore was used as scoring function. Waters *W1* and *W4* were included as toggled waters and water *W3* was defined as fixed part of the pocket structure. Water *W2* was excluded due to its proposed role in substrate and cofactor binding (see Section 2.4).
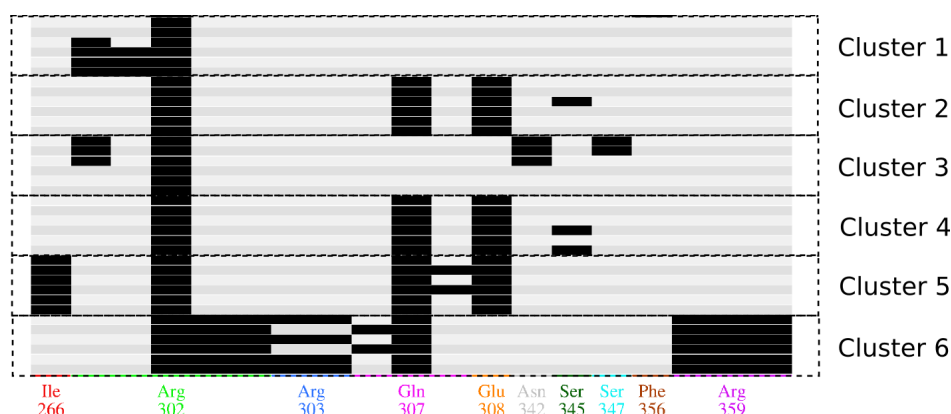
Figure A.6: Protein-ligand interaction fingerprints for overrepresented docking solutions of *Pyro1-6* and CDTa. Only clusters 1-6, which contained solutions from all six pyrrolidinediones were further analyzed.

Each isomer of *Pyro1-6* was docked 20 times to the ensemble of CDTa structures and the top five scored solutions per isomer (in total 120 solutions) were analyzed for a common mode of interaction. Protein-ligand interaction fingerprints[149] were generated by MOE using default settings. The obtained fingerprints were clustered using the Jarvis-Patrick algorithm as implemented in MOE[139]. A intra- as well as inter-cluster similarity cutoff of 85% resulted in 45 different clusters of protein-ligand interactions. However, only six clusters contained solutions from all six pyrrolidinedione based inhibitors, that is why all other clusters were neglect. The protein-ligand interactions of these six clusters are highlighted in Figure A.6 and the docking scores of the best scored solutions are summarized in Table A.3.

	Goldscore					
ID	Pose 1	Pose 2	Pose 3	Pose 4	Pose 5	Pose 6
Pyro1	21.91	21.38	21.20	20.82	19.75	21.02
Pyro2	21.67	21.30	21.39	19.78	20.04	20.11
Pyro3	19.87	19.76	20.43	20.22	19.12	19.66
Pyro4	21.13	20.81	22.14	20.01	19.68	20.41
Pyro5	20.78	19.52	20.12	19.58	20.15	20.83
Pyro6	21.51	20.64	21.16	20.72	19.80	20.76

Table A.3: Docking scores of six different pyrrolidinedione poses. The Goldscores were normalized by dividing the raw score by the number of heavy atoms to the power of 1/3.

The best scored poses of *Pyro1* and *Pyro5* were selected from each cluster (*Pose1-6*) and subjected to a 10 ns MD simulation in order to proof their stability. All simulations were carried out with Amber 12 and an analog protocol as described in Section A.8.1.

As indicated by the RMSD plots shown in Figure A.7, only *Pose6* was sufficient stable for *Pyro1* and *Pyro5* over the whole simulation time.
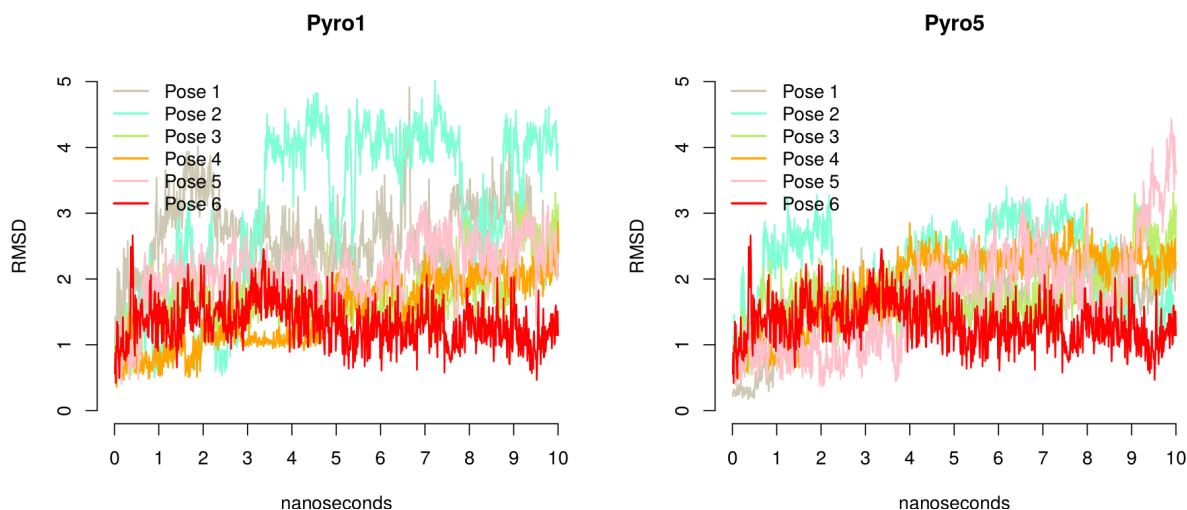
Figure A.7: RMSD plots of six simulated binding poses for CDT and *Pyro1* as well as *Pyro5*. The RMSD values were measured to the corresponding initial coordinates.

A.9 Virtual Screening Protocols

A.9.1 Nicotinamide Related Compounds

The Asinex Gold database was downloaded from the official website (http://www.asinex.com/) and imported into MOE 2012.10[139]. MACCS-key fingerprints were calculated for all molecules and the database was searched for fingerprints similar to the benzamide structure, Using a tanimoto coefficient cutoff of 55%, 571 hits were obtained and further clustered according to their pairwise MACCS-key similarity. 129 compounds obtained from clustering were manually filtered for interesting scaffolds and 58 molecules were prepared for docking experiments. Hydrogens were added, charges were calculated and the geometries were optimized according to the MMFF94 force field as implemented in MOE.

All compounds were docked to an ensemble of three prepared crystal structures of CDTa (2WN5, 2WN6 and 2WN7, see Section A.2) using the docking software Gold 5.1[141]. Hydrogen bond constraints were applied to the backbone amide of Arg303 to sample solutions similar to the native binding mode of NAD^+. Gold was configured for maximum search efficiency and each compound was docked 15 times to all three CDTa models. Goldscore was used for initial pose sampling and ASP score for local refinement. For each compound, the best scored solution was selected from both scoring function and the original scores were normalized by dividing them by the number of heavy atoms to the power of 1/3. All poses were visually analyzed and 14 diverse compounds were finally ordered from Asinex (see Figure A.8 and Table A.4). Their *in-vitro* activity was

tested in a CDT assay described in section A.3.

ID	Vendor ID	Zinc Code	Goldscore	ASP Score	CDT inhibition
VS1	BAS06191909	ZINC00146443	21.66	7.19	52% at 125 μM
VS2	BAS03375267	ZINC04724480	19.80	7.58	50% at 125 μM
VS3	BAS02232114	ZINC05829917	20.61	7.90	43% at 125 μM
VS4	BAS05347442	ZINC19939792	20.68	7.02	38% at 125 μM
VS5	BAS05206574	ZINC00791354	17.50	11.06	35% at 125 μM
VS6	BAS03592030	ZINC00051633	22.57	7.35	29% at 125 μM
VS7	BAS00162045	ZINC05483952	20.32	7.79	n.d.
VS8	BAS06979911	ZINC00253814	20.24	7.01	n.d.
VS9	SYN17914555	ZINC19376105	20.08	6.04	n.d.
VS10	BAS03240607	ZINC00376753	19.70	6.63	n.d.
VS11	ASN10140417	ZINC13564823	18.53	7.75	n.d.
VS12	BAS18380929	ZINC22930579	21.45	8.04	n.d.
VS13	BAS00918912	ZINC00265670	19.04	6.53	n.d.
VS14	BAS02913382	ZINC00101897	18.63	6.55	n.d.

Table A.4: CDT inhibition by VS1-VS14 measured in a radiolabeled NAD^+ assay. The Goldscores and ASP scores were normalized by dividing the raw score by the number of heavy atoms to the power of 1/3.

Figure A.8: CDT virtual screening hits ordered from Asinex.

A.9.2 Cholix-A Inhibitor Analogs

The structure of Cholix-A inhibited by *V30* was downloaded from the PDB (code 3NY6) and V30 was extracted from this complex using MOE 2012.10[139]. The Chembridge diversity database was downloaded from the vendor website (http://www.chembridge.com) and imported into MOE. MACCS-key fingerprints were calculated for all molecules and the database was searched for compounds which show a fingerprints similarity of at least 67%. 182 hits were prepared for docking by adding hydrogens, calculating partial charges and optimizing the geometries in respect to the MMFF94 force field as implemented in MOE.

All compounds were docked to an ensemble of three prepared crystal structures of CDTa (2WN5, 2WN6 and 2WN7, see Table A.2) using the docking program Gold 5.1[141]. Hydrogen bond constraints were applied to the backbone amide of Arg303, to sample analog solutions as compared to the native binding mode of V30 and Cholix-A. Gold was configured for maximum search efficiency and each compound was docked 20 times to all three CDTa models using the Goldscore scoring function. The final Goldscores were normalized by dividing the raw score by the number of heavy atoms to the power of 1/3. The 100 best scored compounds were visually analyzed and 10 compounds were ordered from Chembridge (see Table A.5 and Figure A.9). Their *in-vitro* activity was tested in the CDT assay described in section A.3.

The docking result of compound *VS21* was further refined by an energy minimization according to the ff12SB force field as implemented in MOE. The interaction potential of methyl groups was calculated by the GRID algorithm proximal to the methyl groups of *VS21*. Default energy levels were used and the obtained interaction potential was visualized by drawing the potential map using MOE.

ID	Vendor ID	Zinc Code	Goldscore	ASP Score	CDT inhibition
VS21	6588082	ZINC08714279	20.38	5.81	30% at 125 µM
VS22	6432956	ZINC15822445	20.31	7.40	24% at 125 µM
VS23	7661219	ZINC08572799	20.91	7.20	19% at 125 µM
VS24	7936627	ZINC16399451	20.87	7.82	19% at 125 µM
VS25	5142063	ZINC18128277	20.71	7.24	8% at 125 µM
VS26	5492396	ZINC04646431	20.62	7.85	6% at 125 µM
VS27	5489342	ZINC19202861	19.99	9.98	n.i.
VS28	5850221	ZINC02073252	19.91	6.52	n.i.
VS29	7940195	ZINC05028362	20.18	9.17	n.i.
VS30	7932248	ZINC05028288	20.21	10.43	n.d.

Table A.5: CDT inhibition by VS21-VS30 measured in the NAD$^+$ quantification assay. The Goldscores were normalized by dividing the raw score by the number of heavy atoms to the power of 1/3.
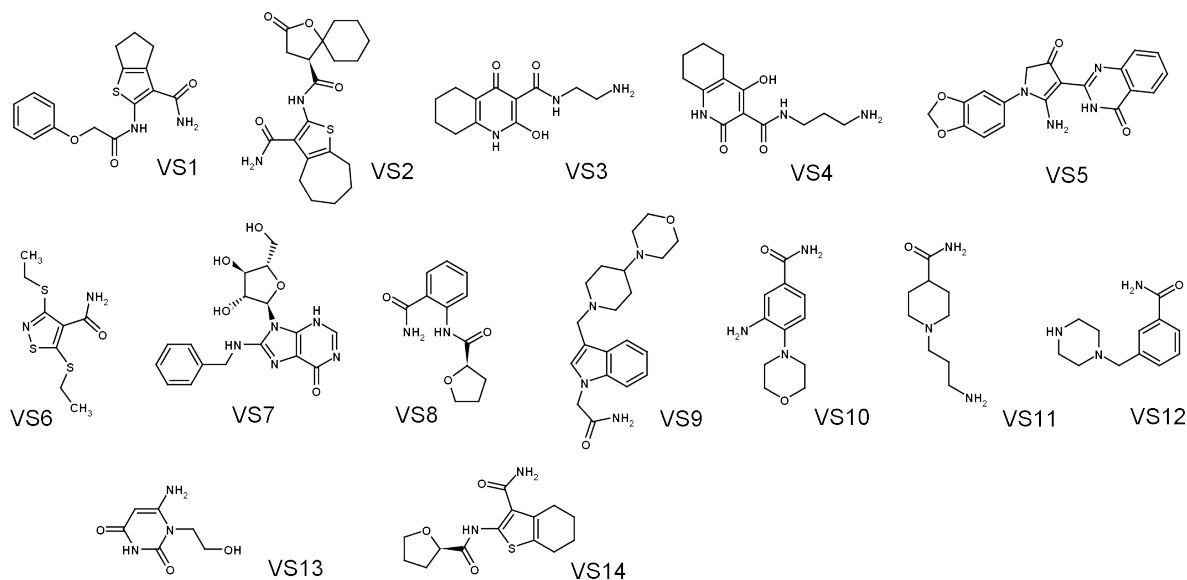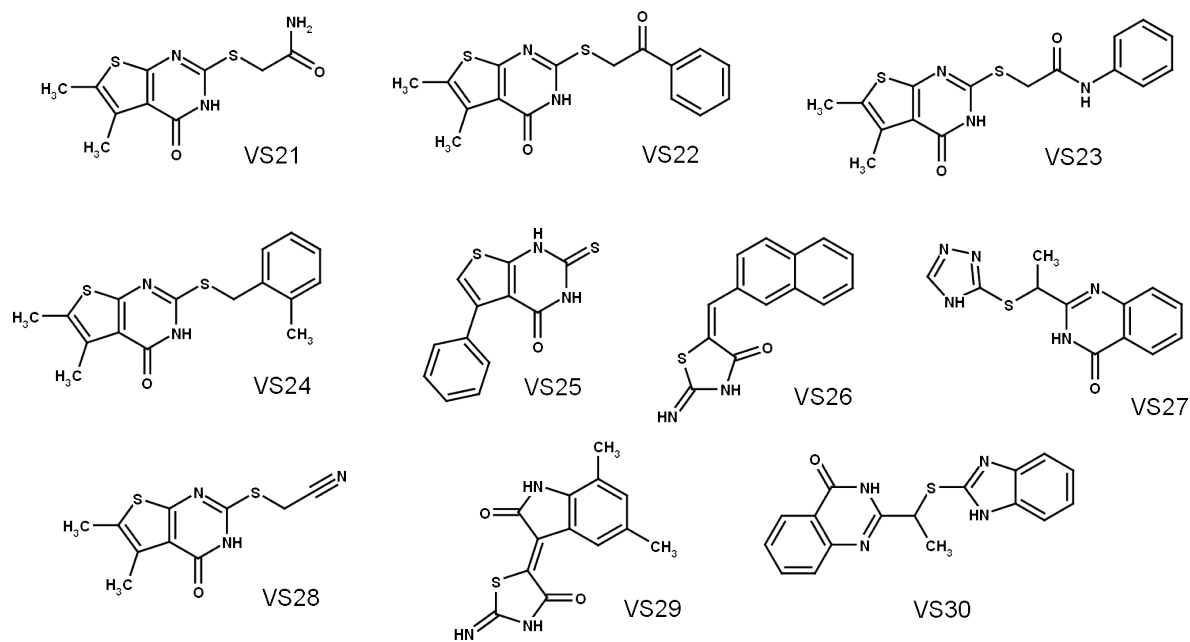
Figure A.9: Structures of virtual screening hits for CDT which were ordered from Chembridge.

APPENDIX B

Molecular Modeling Studies on Sirtuin 5

B.1 Crystal Structures

PDB Code	Protein	Bound Ligands	Resolution
2B4Y	Sirt5	ADPR; HEPES	1.9 Å
2NYR	Sirt5	Suramin	2.1 Å
3RIG	Sirt5	Thioacetylated H3K9 peptide; CHES	2.0 Å
3RIY	Sirt5	Succinylated H3K9 peptide; NAD	1.5 Å
4UTN	zSirt5	Succinylated CPS1 peptide	3.0 Å
4UTV	zSirt5	Phenyl-succinylated CPS1 peptide	2.4 Å
4UUA	zSirt5	Z-amino-succinylated CPS1 peptide	2.8 Å
2H2I	Sir2-Tm	Polypropylene glycol	1.8 Å
1YC5	Sir2-Tm	Nicotinamide; acetylated peptide	1.4 Å
4IG9	Sirt1		2.6 Å
4KXQ	Sirt1	ADPR	1.85 Å
3ZGO	Sirt2		1.63 Å
3ZGV	Sirt2	ADPR	2.27 Å
3GLS	Sirt3	Triethylene glycol	2.7 Å
3GLT	Sirt3	ADPR; Thioacetylated peptide	2.1 Å
3K35	Sirt6	ADPR	2.0 Å
3ZG6	Sirt6	ADPR; Myristoylated peptide	2.2 Å

Table B.1: Protein structures used for the modeling studies described in Section 3.

The structures listed in Table B.1 were downloaded from the PDB and prepared for the computational studies described in Section 3. Missing atoms were added, partial charges were calculated and the structure was protonated using standard methods and default settings of MOE 2012.10[139].

B.2 *In-vitro* Assays for Sirt5

B.2.1 Fluorescence-based Assay

The following fluorescence-based *in-vitro* assay was developed at University Freiburg - a more detailed description, including information on compound synthesis can be found in the work of Maurer et al.[77,102].

Z-Lys(succ)-aminomethyl coumarin derivative (*ZK(s)A*, see Figure B.1) was synthesized and used as Sirt5 substrate. It was shown that *ZK(s)A* is very stable even under high trypsin concentrations. In contrast, the desuccinylated metabolite (*ZKA*, see Figure B.1) can be easily cleaved by trypsin. The amount of released aminomethyl coumarin (AMC) can be measured due to a shift in fluorescence wavelength. 200 µM *ZK(s)A* and an enzyme concentration leading to a conversion of 5-10% in 1 hour led to a stable and strong fluorescence signal which could be measured at λEx=390nm and λEm=460nm in a microtiter plate reader. Kinetic constants were measured by end-point determination using the same assay with *ZK(s)A* concentrations ranging from 1 to 1000 µM. The K_M for *ZK(s)A* was 17.4 ± 1.8 µM and the V_{max} was 5.3 x 10^{-3} µM.
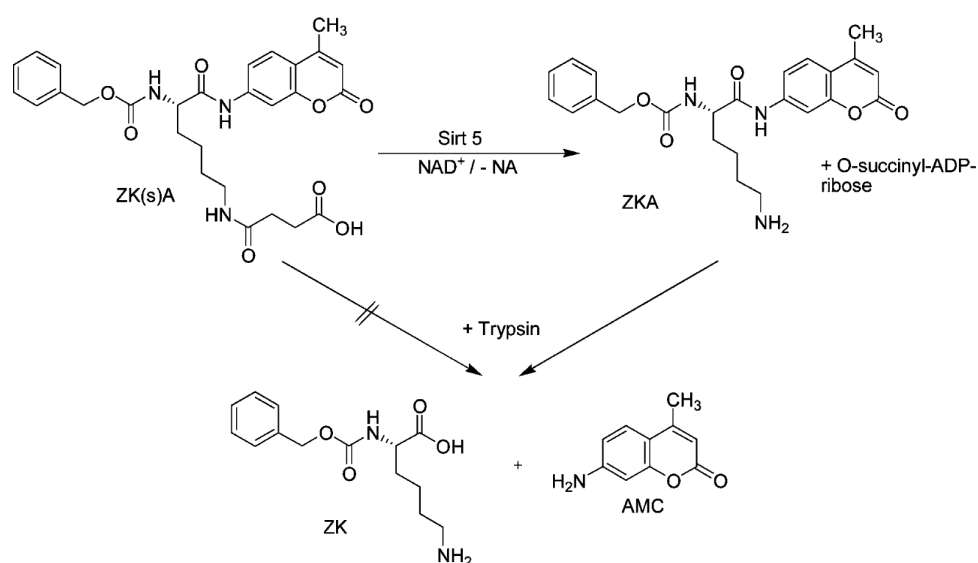
Figure B.1: Substrate and general reaction scheme for Sirt5 fluorescence-based assay.

Small molecule inhibition of Sirt5 was measured by the following protocol. Sirt5 was mixed with *ZK(s)A* (200 µM), NAD$^+$ (500 µM), the small molecule, DMSO (<2% v/v) and assay buffer (25 mM Tris-HCl, 130 mM NaCl, 3 mM KCl, 1 mM MgCl$_2$, pH 8.0 and 0.1% PEG8000) to a volume of 51µL. The mixture was incubated for 1 hour (37°C, 750rpm), then treated with 10 µL of trypsin solution (50 mM Tris-HCl, 130 mM NaCl and 6 mg/mL trypsin) and incubated for 2 minutes (37°C, 1250rpm). The fluorescence intensity was measured with a microtiter plate reader (BMG Polarstar, λEx=390nm, λEm=460nm). To ensure initial state conditions, the conversion of *ZK(s)A* was adjusted

to 5-10% substrate conversion without inhibitor. A mixture containing DMSO only was used as control, and inhibition rates for small molecules were calculated in reference to the DMSO control. All inhibition experiments were run at least twice and IC_{50} values were determined with the Graphpad Prism 4.0 software.

B.2.2 HPLC-based Assay

The following HPLC *in-vitro* assay was developed at the Institute for Biochemistry at University Halle-Wittenberg - a more detailed description, including information on compound synthesis can be found in the work of Roessler et al.[67].

A CPS1-derived peptide sequence (*Bz-Gly-Val-Leu-**Lys**-Glu-Tyr-Gly-Val-NH$_2$*), identified by high-density peptide microarray experiments, was used as scaffold for several Sirt5 substrates and inhibitors. A series of analogous peptides, acylated at the lysine side chain with the PTMs shown in Figure B.7, were synthesized.

Kinetic constants for Sirt5 mediated reactions were determined using an HPLC-based assay. Solutions containing 20 nM Tris-HCl pH 7.8, 150 mM NaCl, 5 mM $MgCl_2$, 0.5 mM NAD^+ and varying peptide concentration (2-200 µM) were used. The reaction was started by adding human Sirt5 to reach a final concentration of 0.5 µM. The reaction was stopped using TFA (1% final concentration) after 1 to 180 minutes of incubation at 37°C, depending on substrate reactivity. The cleavage rate of the different CPS1-derived peptides was analyzed using analytical reversed phase HPLC. The product and substrate peaks were quantified using absorbance at 260 nm (N-terminal benzoyl moiety). The peak areas were integrated and converted to initial velocity rates calculated from the ratio of product area to total peak area. Linear regression of conversions plotted against time yielded reaction rates in µM/min. Non-linear regression according to Michaelis-Menten-equation of the reaction rates at different peptide concentrations yielded K_M and k_{cat} values. All measurements were done twice and controls without NAD^+ yielded no conversion of the substrates under identical conditions. The analysis of kinetic constants for NAD^+ was performed equally (100 µM succinylated peptide, 0.5 µM Sirt5 and 10-2000 µM NAD^+).

K_i values of CPS1-derived inhibitors were determined, by recording K_M and k_{cat} values for the succinylated peptide in the presence of varying inhibitor concentrations (50 to 250 µM). Linear regression of appearent K_M values against the corresponding inhibitor concentration yielded the inhibitor constant K_i. All calculations were carried out with the program SigmaPlot (Systat Software, San Jose, USA).

B.3 Conformational Sampling

All simulations described in Section 3.3.1 based on the crystal structure of Sirt5 in complex with NAD^+ and succinylated H9K3 peptide (PDB: 3RIY, see Section B.1). The zinc ion was (manually) parameterized with a charge of +2, an atomic mass of 65.4 amu, a vdW radius of 1.10 Åand a well depth of 0.0125. AM1-BCC charges were calculated for the succinylated lysine and NAD^+, using the *antechamber* program of

AmberTools 13[142]. The parameterized succinylated lysine was manually connected with the other peptide residues using the *xleap* program. All remaining residues were parameterized using the default parameters of the ff12SB and GAFF force field. Two systems were constructed from all prepared residues - one contained the Sirt5 protein only, and the second system additionally included the succinylated peptide as well as NAD$^+$, both in their co-crystallized conformation. Both systems were neutralized by adding adequate counterions and explicitly solvated using TIP3P waters inside a 10 Å octahedron periodic box.

After a minimization, heating and equilibration (using the same protocol as described in Section A.6.1), both equilibrated systems were used as input for a conventional as well as accelerated MD.

Conventional MD Simulation

The unbound and substrate-bound systems of Sirt5 were subjected to a 75 ns MD simulation using the same protocol as described in Section A.6.1 (*cMD-apo* and *cMD-holo*). The stability of both simulations was proofed by the calculation of RMSD value for each superimposed snapshot in respect to the initial coordinates. As can be seen from Figure B.2 and Figure B.3, both systems were stable after a short equilibration phase.
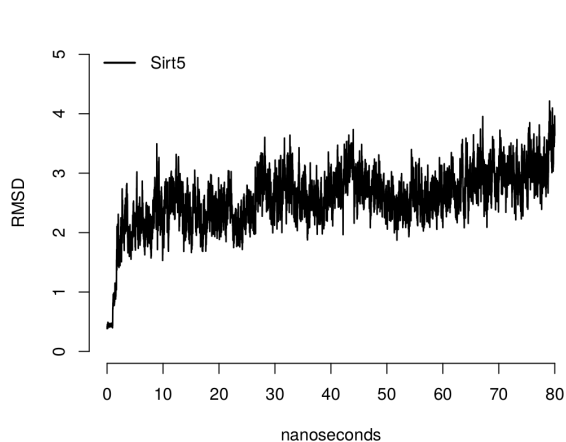
Figure B.2: Cα-RMSD values for each snapshot produced by the *cMD-apo* simulation of Sirt5.
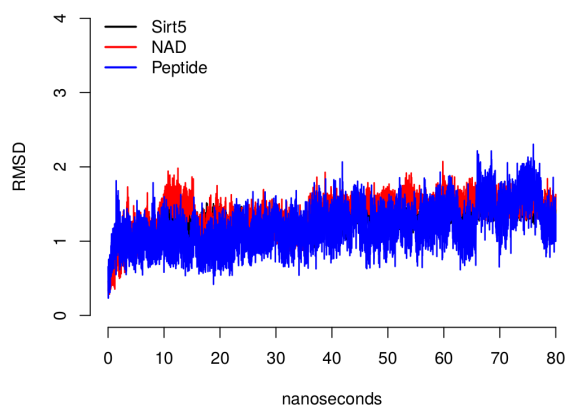
Figure B.3: Cα-RMSD values for each snapshot produced by the conventional simulation of Sirt5 (black), in complex with NAD$^+$ (red) and succinylated peptide (blue).

Accelerated MD Simulation

To set up the accelerated MD simulations of Sirt5 (*aMD-apo*) and Sirt5 in complex with succinylated peptide (*aMD-holo*), the average total potential energy threshold (EthreshP), the inverse strength boost factor for the total potential energy (alphaP), the average dihedral energy threshold (EthreshD) and the inverse strength boost factor

for the dihedral energy (alphaD) need to be calculated. As suggested in the study of Pierce et al.[114], these parameters were calculated by

$$
\begin{aligned}
\text{alphaP} &= 0.16 * \text{numAtoms} = 9262 \ (8932) \\
\text{EthreshP} &= \overline{\text{E}_\text{p}} + \text{alphaP} = -131550 \ (-126463) \\
\text{EthreshD} &= \overline{\text{E}_\text{d}} + (4 * \text{numRes}) = 5394 \ (5580) \\
\text{alphaD} &= 1/5 * 4 * \text{numRes} = 191 \ (197)
\end{aligned}
$$

whereby *numAtoms* is the total number of atoms in the system, *numRes* is the number of protein residues, $\overline{\text{E}_\text{p}}$ is the average total potential energy during equilibration and $\overline{\text{E}_\text{d}}$ the average dihedral energy during equilibration. Note, the results in the brackets are the results for the Sirt5 complex including NAD^+ and succinylated peptide.

The calculated boost parameters were used as input for both 75 ns accelerated MD simulations (*aMD-apo* and *aMD-holo*) - all other parameters were set to the same values as used for the conventional simulation. RMSD values in respect to the equilibration result were calculated for each snapshot extracted from the whole trajectory. The stability of both aMD simulations was proofed by the calculation of RMSD value for each superimposed snapshot in respect to the initial coordinates. As can be seen from Figure B.4 and Figure B.5, both systems were stable after an equilibration phase.
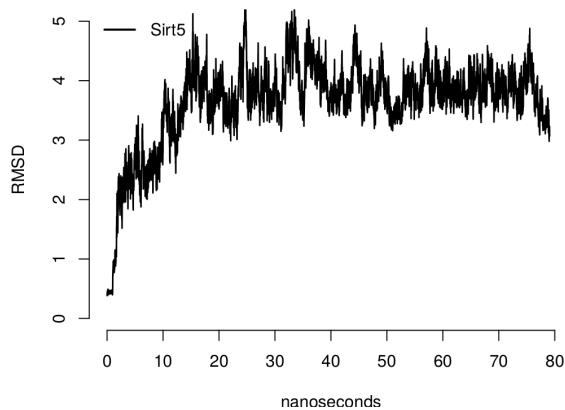
Figure B.4: Cα-RMSD values for each snapshot produced by the *aMD-apo* simulation of Sirt5.
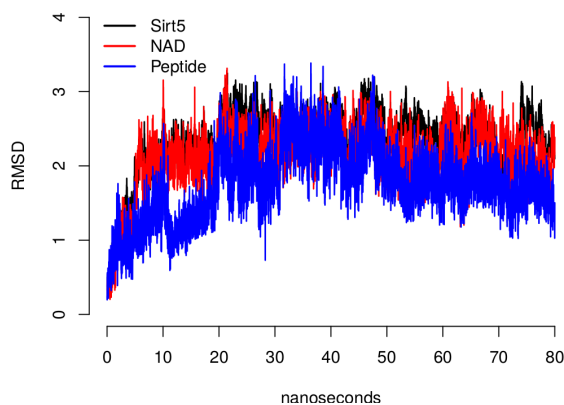
Figure B.5: Cα-RMSD values for each snapshot produced by the accelerated simulation of Sirt5 (black), in complex with NAD^+ (red) and succinylated peptide (blue).

B.3.1 B-Factor Calculations

B-factors obtained from crystallographic refinement were extracted from the original PDB files of all Sirt5 structures listed in Table B.1. An average B-factor profile was

calculated from all individual profiles and normalized to zero mean and unit variance*. Average models were calculated for both accelerated MD simulations (*aMD-apo* and *aMD-holo*) using the *cpptraj* program of AmberTool13[146]. B-factores were estimated from the positional fluctuation of each Cαatom around the corresponding average position. Each B-factor profile was normalized and mapped to the normalized B-factors determined by X-ray crystallography.

B.3.2 Principal Components Analysis (PCA)

A principal components analysis was carried out for all conformation sampled during the *aMD-apo* and *aMD-holo* simulations of Sirt5. Using *cpptraj* (AmberTool13), all non-protein residues (water, NAD$^+$ and peptide) were removed and each trajectories were aligned to the corresponding average conformation. The covariance matrices were built from the coordinates of the superimposed conformations and their eigenvectors and eigenvalues were calculated. It was found that the first two eigenvectors describe about 48% of the total variance of the motions observed during the *aMD-apo* simulation. All conformations sampled during the four simulations of Sirt5 (*aMD-apo*, *aMD-holo*), *cMD-apo*, *cMD-holo*) as well as all X-ray structures listed in Table B.1 were projected on the first two eigenvectors of *aMD-apo*. The PCA plots shown in Figure 3.5 and Figure 3.6 were generated using R[140].

B.3.3 Cluster Analysis

The trajectory of the *aMD-apo* simulation of Sirt5 was clustered using the *ptraj* program distributed with AmberTools13[146]. All sampled conformations were aligned to the average model by a root-mean-square fit of their corresponding backbone atoms. A hierarchical clustering was carried out using the average-linkage method - the number of final clusters was set to three. For each individual cluster, the cluster centroid was extracted from the trajectory and was chosen as representative conformation for further analysis.

B.3.4 Structural Comparison of Apo Structures

The homology detection server *HHPred*[133] was used to search for Sirt5 homologous proteins inside the PDB. *HHPred* was configured by using three iterations of *HHBlits* for local sequence alignments and scoring secondary structures. The top four homologs (with apo structures available) were Sir2-Tm (29% sequence identity), Sirt1 (27% identity), Sirt3 (27% identity) and Sirt2 (23% identity).

---

* For details, see work of Parthasarathy et al. [96]

	1	2	3	4	5	6	7
1: 2H2I	0.00	2.22	2.14	2.34	1.95	1.99	2.52
2: 4IG9	2.22	0.00	1.53	1.17	2.13	2.26	2.43
3: 3ZG0	2.14	1.53	0.00	1.51	2.10	2.24	2.25
4: 3GLS	2.34	1.17	1.51	0.00	2.21	2.34	2.66
5: 2B4Y	1.95	2.13	2.10	2.21	0.00	0.99	1.85
6: C2	1.99	2.26	2.24	2.34	0.99	0.00	1.92
7: C3	2.52	2.43	2.25	2.66	1.85	1.92	0.00

Figure B.6: RMSD matrix of superimposed Sirt5 apo models *C2-C3* and apo structures of other Sirtuins.

The corresponding structures (see Table B.1), as well as Sirt5 in complex with ADPR and HEPES (PDB: 2B4Y) were superimposed to two *in-silico* conformations obtained from MD trajectory clustering (*C2* and *C3*, see Section B.3.3). As can be seen from the RMSD matrix shown in Figure B.6, *C2* shows the highest conformational overlap with the apo structure of Sir2-Tm (PDB: 2H2I).

B.3.5 Interdomain Angle Between RFD and ZBD

The interdomain angle between the Rossmann fold domain and the Zinc-binding domain of Sirt5 was defined by the geometric centers of the following three atom masks:

1) Cα atoms of residues 235-240, which form α-13 helix as part of the Rossmann fold domain

2) Cα atoms of residues 227-229, which are part of the intersection between the Rossmann fold domain and the Zinc-binding domain

3) Cα atoms of residues 87-91, which form the α-6 helix as part of the Zinc-binding domain

The angle was measured for each frame of the *aMD-apo* as well as the *aMD-holo* trajectory using the program *cpptraj* from AmberTools 13[146]. Reference angles were determined for the apo structure of Sir2-Tm (PDB: 2H2I) and the substrate bound conformation of Sir2-Tm (PDB: 1YC5) after determining the corresponding residues by a superpositioning with MOE[139].

B.3.6 Conformations of Arg105

The torsion angles of Arg105 ($\phi, \psi, \chi_1, \chi_2, \chi_3, \chi_4, \chi_5$) were measured for two reference structures of Sirt5 (PDB: 3RIG and 3RIY, see Table B.1) as well as each conformation

extracted from the *cMD-apo* and *cMD-holo* trajectories. The program *cpptraj* from AmberTools13[146] was used for all calculations. The scatter plots shown in Figure 3.11 were generated with the statistical software R[140].

B.4 Solvent Analysis

B.4.1 Detection of Conserved Crystal Waters

All structures of human Sirtuins listed in Table B.1 were downloaded from the PDB and superimposed using MOE[139]. All solvent molecules inside the Sirtuin binding cleft (as defined by a maximum distance of 6 Å around all co-crystallized cofactors or peptides) were visually analyzed for conservation. A water was defined as conserved, if related waters exist in at least three structures not more than 1.5 Å away from the origin location. A water was defined as highly conserved, if an identical water was found in at least one crystal structure of each included Sirtuin type. The B-factors shown in Table 3.2 were extracted from the original PDB file of the Sirt5 Michaelis-Menten complex (PDB: 3RIY).

B.4.2 3D-RISM Analysis

3D-RISM calculations were carried out for Sirt5 in complex with NAD^+ and succinylated peptide (PDB: 3RIY, see Table B.1) as well as an unbound conformation of Sirt5 (*C2*, see Section B.3.3). All solvent molecules determined by crystallisation were removed and both systems were prepared for 3D-RISM calculations using the *tleap* program from AmberTools 13 and an anolog protocol as described in section B.3.

The 1D susceptibility function (1D-RISM) was calculated using the solvent mixture of SPC water, sodium and cholorine with concentrations of 55.5M, 0.005M and 0.005M. Default parameters as implemented in Amber 12[142] were used for all calculations. Single point 3D-RISM calculations on both Sirt5 systems were carried out using the *3drism.snglpnt* program as distributed with Amber. The 1D-RISM output was included as input and the KH-closure was used for convergency reason - all other parameters were set to their default values.

Explicit water locations were calculated using *Placevent*[122] and the water oxygen distribution function as input. The predicted waters were superimposed with the seven conserved waters found by X-ray studies and their pairwise distance was measured using MOE[139]. The binding affinity of each water was approximated by the 3D-RISM distribution function $g(r)$ and the formula

$$\Delta G_{\mathrm{pred}} = -k_B T \ln g(r)$$

B.5 Binding Models of CPS1-based Peptides

B.5.1 CPS1-based Peptides

All CPS1 derived peptides based on the sequence *Benzoyl-Gly-Val-Leu-Lys(X)- Glu-Tyr-Gly-Val-amide.* The molecular structure was extracted from the crystal structure of zSirt5 in complex with *CP3* (PDB: 4UTN). Each PTM shown in Figure B.7 was attached on the lysine side chain and the complete peptides were charged and protonated using default methods and parameters as implemented in MOE[139]. The geometry of the (attached) lysine modification was optimized according to the ff12SB force field.
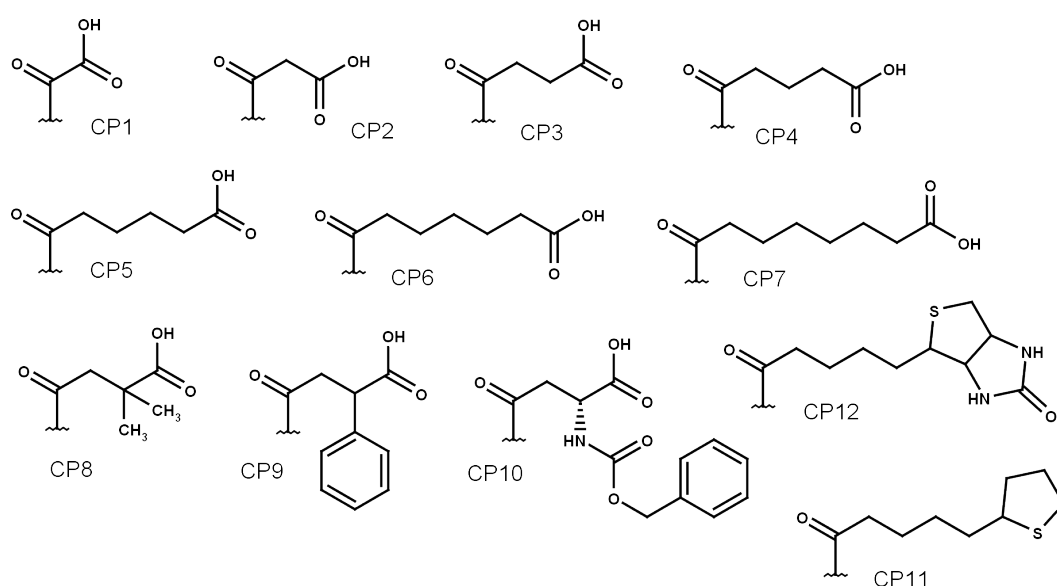
Figure B.7: Lysine side chain modifications of CPS1-based peptide derivatives.

B.5.2 Docking of CPS1-based Peptides

All docking experiments of CPS1 derived peptides based on the crystal structure of zSirt5 in complex with *CP3* (PDB: 4UTN, see Table B.1). The structure was superimposed with two structures of human Sirt5, which show two alternative conformations of Arg105 (PDB: 3RIY and 3RIG). The PTM of *CP3* was removed in order to use the unmodified lysine residue as scaffold constraint for docking.
The dockings studies were carried out using the Gold 5.1 docking program[141]. The superimposed conformation of *CP3* was used to define the binding cavity, as well as to guide the conformational search process by applying a substructure constraint to the corresponding coordinates. Goldscore was as fitness function and each CPS1-based peptide derivative was docked 20 times to both Sirt5 structures using maximum search efficiency. All results were visually analyzed and docking solutions with the highest overlap to the superimposed position of *CP3* were optimized by an energy minimization

using the Amber12SB force field as implemented in MOE[139]. Conserved waters* as well as NAD$^+$ was superimposed†, in order to proof the compatibility with the generated models.

B.5.3 Modeling of CPS1-based Peptidic Inhibitors

Based on structures of zSirt5 in complex with *CP9* and *CP10* (PDB: 4UTV and 4UUA, see Table B.1), a number of CPS1-based peptide derivatives were generated using the molecular builder of MOE[139]. All peptides shown in Figure B.8 were subjected to a molecular docking using Gold 5.1[141] and analog settings as described in Section B.5.2. All results were visually analyzed and selected solutions, with interactions inside the Sirt5 C-pocket, were further refined by an energy minimization using the Amber12SB force field as implemented in MOE[139].
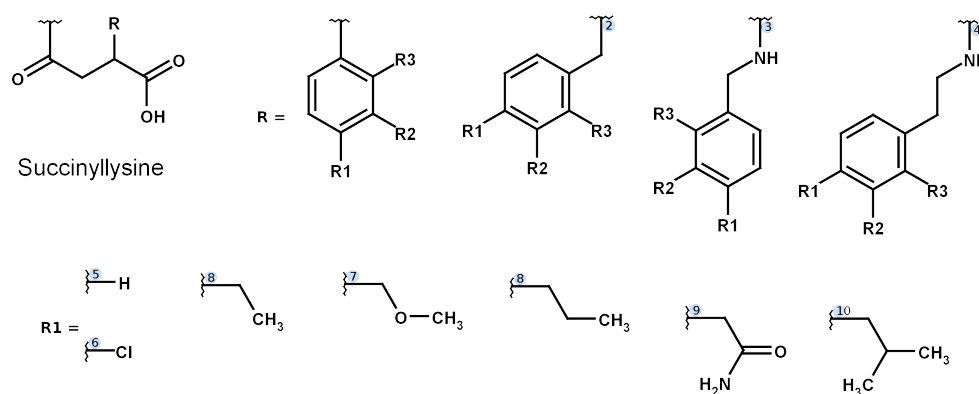
Figure B.8: Structure of succinyllysine modifications suggested for CPS1-based peptide derivatives.

B.6 Binding Models of Thiobarbiturates

B.6.1 Substructure Search for Thiobarbitures

Virtual compound libraries were downloaded from the webpages of Chembridge‡, Princeton§ and Asinex¶. All libraries were screened for compounds containing a (thio)barbiturate-furylidene substructure using the program *filter*[150] and the SMARTS pattern shown in Figure B.9. In total, 169 hits were obtained and 13 diverse compounds were cherry picked and ordered from their corresponding vendor (see Table B.2).

---

*   See Section 3.4.1
†   Only for binding models of the substrates *CP1-CP8*
‡   Chembridge core library, *http://www.chembridge.com*
§   Princeton express library, *http://www.princetonbio.com*
¶   Asinex Gold library, *http://www.asinex.com*

[#8,#16]~[#6]~3~[#7]~[#6](~[#8])~[#6](~[#6]~[#6]~2~[#6]~[#6]~[#6]~[#8]~2)~[#6](~[#8])~[#7]~3
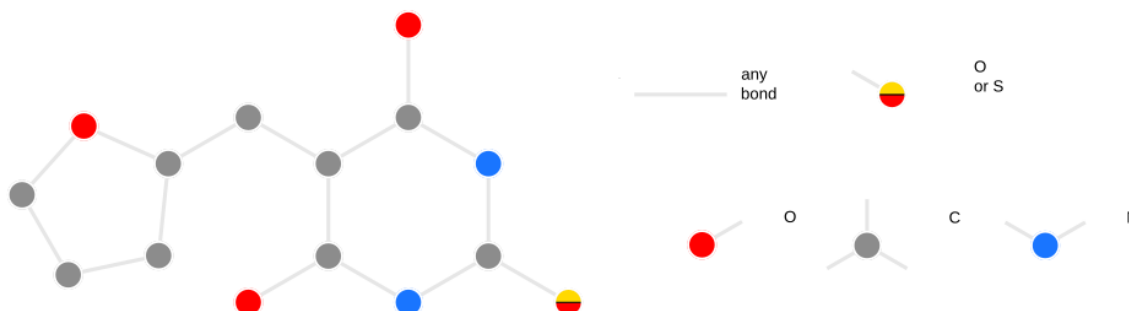
Figure B.9: SMARTS pattern used for thiobarbiturate substructure search. The picture was created with the SmartsViewer web application[151]

ID	Vendor	Vendor Code	ID	Vendor	Vendor Code
ThiFu1	Chembridge	6968082	ThiFu9	Princeton	OSSK392265
ThiFu2	Chembridge	6060663	ThiFu10	Chembridge	7051181
ThiFu3	Chembridge	5966223	ThiFu11	Chembridge	5981836
ThiFu4	Chembridge	6889109	ThiFu12	Asinex	BAS00282848
ThiFu6	Asinex	BAS00886232	ThiFu14	Princeton	OSSK336940
ThiFu7	Chembridge	5971692	ThiFu15	Chembridge	5805828
ThiFu8	Chembridge	6076157			

Table B.2: Thiobarbitures and barbiturates purchased from SMARTS based virtual screening hits.

B.6.2 Dataset of Thiobarbiturates

The complete dataset of (thio)barbiturates, which were tested on Sirt5, is listed in Table B.3. The molecular structures were either obtained from the corresponding vendor catalogs (Chembridge, Princeton and Asinex) or generated with the molecule builder of MOE 2012.10[139]. The programs *flipper* and *pkatyper* from OpenEye[150] were used to enumerate all E/Z isomers and relevant protonation states. All conformations were optimized by an energy minimization using the MMFF94 force field as implemented in MOE.

						IC_{50} (μM)			
ID	*X*	*R_1*	*R_2*	*R_3*		*Sirt5*	*Sirt1*	*Sirt2*	*Sirt3*
Scaffold 1	**(S1)**								
ThiFu1	S	H	CH_2-CH=CH_2	2,3-Dichlorphenyl		2.3	5.3	9.7	
ThiFu2	S	H	H	Phenylsulfanyl		2.8	3.8	3.5	14.6
ThiFu3	O	H	CH_2-CH=CH_2	2,5-Dichlorphenyl		2.9			
ThiFu4	S	H	CH=CH_2	4-Brom-3-chlorphenyl		3.1			
ThiFu5	S	H	H	2,3-Dichlorphenyl		3.3			
ThiFu6	O	H	4-Methylphenyl	3,4-Dichlorphenyl		4.1			
ThiFu7	O	H	CH_3	3,4-Dichlorphenyl		4.3			
ThiFu8	S	H	H	4-Methylphenylsulfanyl		4.6			
ThiFu9	S	H	CH_3	4-Chlorphenyl		5.2			
ThiFu10	O	H	Benzyl	2-Chlorphenyl		13.1			
ThiFu11	S	H	CH_2-CH=CH_2	4-Fluorphenyl		13.4			
ThiFu12	S	H	H	3-Chlor-4-methylphenyl		15.9			
ThiFu13	S	H	H	4-Methoxyphenyl		29.3			
Scaffold 2	**(S2)**								
ThiBe1	S	H	H	4-Brombenzyloxy		6.2	9.9	3.4	30.3
ThiBe2	S	H	H	1-Naphtylmethoxy		7.6			
ThiBe3	S	H	Benzyloxy	H		8.7			
ThiBe4	S	H	Methoxy	2-Chlorbenzyloxy		12.4			
ThiBe5	S	Ethyl	H	Benzyloxy		12.9			
ThiBe6	S	H	H	Benzyloxy		14.9	10.5	9.8	29.3
ThiBe7	S	Methyl	H	Benzyloxy		17.8			
ThiBe8	S	H	H	Phenyl		20.8	50.5	8.7	
ThiBe9	O	H	Methoxy	2-Chlorbenzyloxy		27.0			
ThiBe10	O	H	H	Benzyloxy		29.7			
ThiBe11	S	H	H	tert-Butyl		34.2	9.2	10.9	121.0
ThiBe12	S	H	H	Isopropyl		39.4	12.4	14.7	
ThiBe13	S	Allyl	-H	Benzyloxy		67.2			
Scaffold 3	**(S3)**								
ThiIn1	S	H	Benzyl			16.2			
ThiIn2	S	Methyl	H			27.0			
ThiIn3	S	H	H			46.5	5.9	20.3	
ThiIn4	S	Ethyl	H			55.9			
ThiIn5	S	Allyl	H			65.9			
Other scaffolds									
ThiSo1	S			see figure B.10		16.2	6.0	11.7	29.3
ThiSo2	S			see figure B.10		27.0			
ThiSo3	O			see figure B.10		46.5			
ThiSo4	S			see figure B.10		55.9			

Table B.3: Dataset of Sirt5 inhibitors containing a barbiturate or thiobarbiturate moiety.
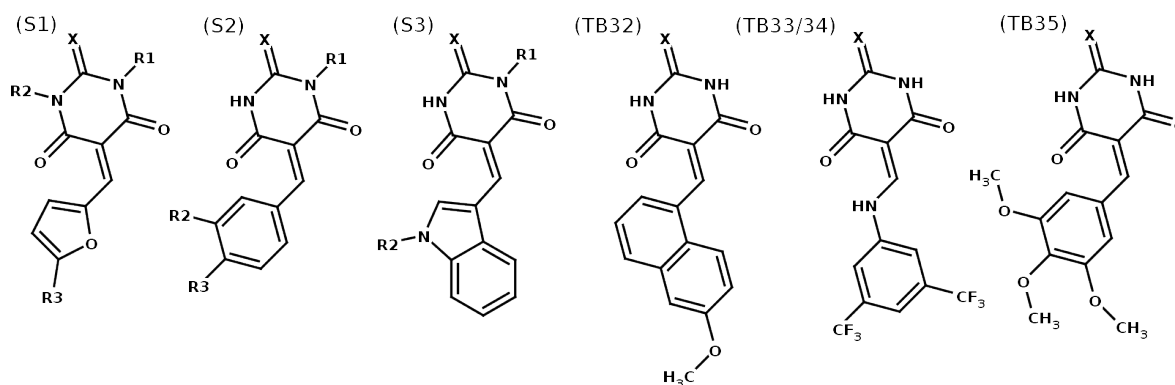
Figure B.10: Scaffold of (thio)barbiturate inhibitors of Sirt5.

B.6.3 Docking of Thiobarbiturates

The structure of *ThiFu2* was prepared for molecular docking by calculating partial charges, adding hydrogens and minimizing the potential energy using the MMFF94 force field as implemented in MOE 2012.10[139]. Gold 5.1 was used to dock *ThiFu2* to four different conformations of Sirt5[141]. Three distinct crystal structures (PDB: 3RIY, 2NYR and 2B4Y, see Section B.1) as well as one conformation obtained from the MD studies (*C2*, see Section B.3.4) were included in the docking ensemble.

The pocket was defined by the nicotinamide-ribose moiety of NAD^+, as bound to the Michaelis-Menten complex of Sirt5 (PDB: 3RIY). The genetic algorithm of Gold was configured for a maximum search efficiency and Goldscore was used as objective function. *ThiFu2* was docked 20 times to all Sirt5 models and all solutions were visually analyzed for reasonable binding modes. Five distinct binding modes were further analyzed by MD simulation, carried out by an analog procedure as described in section A.8.1. As can be seen in Figure B.11, only one model (Pose 5) was highly stable during a 15 nanosecond simulation time.

The last snapshot of Pose 5 was refined by an energy minimization using *pmemd* and the final complex was superimposed with the Michaelis-Menten structure of Sirt5, in order to compare the binding mode of *ThiFu2* and natively bound NAD^+ (see Figure 3.20).

The remaining 33 (thio)barbiturates of the dataset (see Table B.6.2) were prepared for molecular docking using the same protocol as described for *ThiFu2*. The final conformation of Sirt5, extracted from the refined model of *ThiFu2*, was used as protein structure for the subsequent docking experiment. All compounds were docked with Gold 5.1 and hydrogen bond contraints were applied to the protein residues found to be involved in binding of *ThiFu2* (Pro68, Ile142 and Asp143). Each compound was docked 15 times and the top five scored solutions were visually analyzed. For 21 (thio)barbiturates, a comparable pose as suggested for *ThiFu2* was found within the top five scored solutions (see Table B.4).
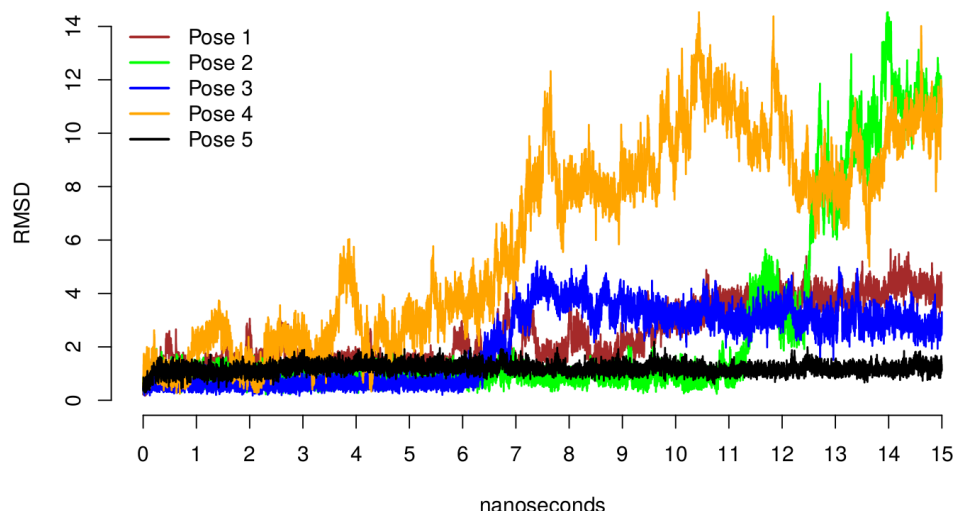
Figure B.11: RMSD values of thiobarbiturate scaffold during a 15ns MD simulation. Five poses (models) were analyzed and only Pose 5 was stable for the whole simulation time.

ID	Score	ID	Score	ID	Score
ThiBe1	60.38	*ThiBe10*	46.54	*ThiFu13*	59.99
ThiBe2	58.67	*ThiBe11*	44.18	*ThiIn1*	51.71
ThiBe3	59.16	*ThiBe12*	53.87	*ThiIn3*	47.96
ThiBe4	66.11	*ThiFu2*	55.98	*ThiSo1*	47.11
ThiBe6	59.45	*ThiFu5*	53.60	*ThiSo2*	47.77
ThiBe8	53.86	*ThiFu8*	73.12	*ThiSo3*	47.85
ThiBe9	53.72	*ThiFu12*	59.57	*ThiSo4*	43.72

Table B.4: Docking scores (Goldscores) of non-alkylated thiobarbiturates and Sirt5.

B.6.4 Docking of *ThiFu2* and Sirt1-3

ThiFu2 was docked to apo and holo structure of Sirt1-3 (PDB codes see Table B.1). All structures were superimposed with the final binding model of *ThiFu2* and Sirt5 and the search space for docking was defined by the coordinates of *ThiFu2*. Gold 5.1 was configured for a maximum search efficiency and Goldscore was used as objective function. *ThiFu2* was docked 20 times to each structure of Sirt1-3 and all solutions were visually analyzed and compared with the binding mode found for Sirt5. Consistently, this binding mode was found for each Sirtuin among the top scored solutions (see Table B.5) Selected solutions were refined by energy minimizations using the Amber12SB force field as implemented in MOE 2012.10[139].

	Sirt1		Sirt2		Sirt3		Sirt5	
ID	Score	PDB	Score	PDB	Score	PDB	Score	PDB
ThiFu2	61.72	4IG9	57.53	3ZGO	63.16	3GLS	66.55	3RIY

Table B.5: Docking scores (Goldscore) of *ThiFu2* for Sirt1-3 and Sirt5. Constraints were applied to guide the docking process towards the final model obtained for Sirt5.

B.6.5 Docking of N-alkylated Thiobarbiturates

The structures of *ThiFu1* and *ThiFu6* were prepared by the same procedure as described for *ThiFu2* (Section B.6.3). Both compounds were docked to six different conformations of Sirt5, including four distinct crystal structures (PDB: 3RIY, 3RIG, 2NYR and 2B4Y, see Table B.1) and two conformations obtained from the MD studies (*C2* and *C3*, see Section B.3.4). All crystal structures were prepared as described in Section B.1 and the conformations obtained from the MD studies were additionally minimized using the Amber12 force field as implemented in MOE[139].
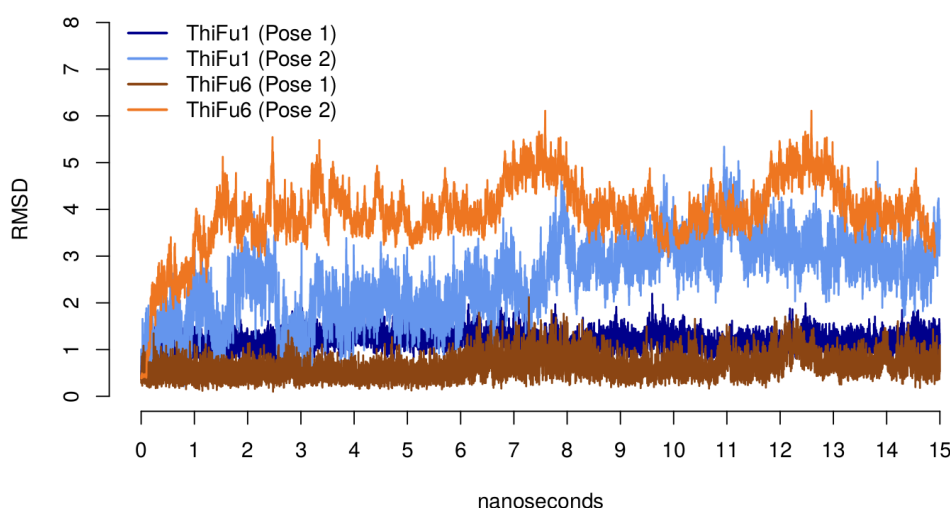
Figure B.12: RMSD value of N-alkylated (thio)barbiturate scaffold during 15 ns simulations of two binding models for *ThiFu1* and *ThiFu6*.

The pocket was defined by the superimposed docking pose of *ThiFu2* and hydrogen bond constraints were specified for Ile142 and Asp143, in order to guide the sampling towards similar interactions. The genetic algorithm of Gold 5.1[141] was configured for maximum search efficiency and Goldscore was used as objective function. Each ligand was docked 20 times to all six conformations of Sirt5 and the solutions were visually analyzed for reasonable binding modes. Two distinct binding modes* showed the desired interactions inside the C-pocket and were further analyzed by means of

---

* Pose 1 was obtained for the receptor model *C2* and Pose 2 for the Sirt5 crystal structure 2B4Y

MD simulations. All MD simulations were carried out using Amber 12[142] and analog protocols as described in section A.8.1. As can be seen in Figure B.11, only one model was sufficient stable for the whole simulation time.

B.7 Virtual Screening Protocols

B.7.1 Succinyl-lysine Similarity Screening

Vendor catalogs from Princeton*, Chembridge† and Asinex‡ were downloaded from the ZINC database[125] and converted to SMILES strings using the program *babel* from Openeye[150]. A SMARTS search for compounds containing a succinyl or glutaryl group was carried out using the Openeye program *filter* and the patterns shown in Figure 3.24. In total, 487 compounds containing a succinyl group and 291 compounds containing a glutaryl group were found.
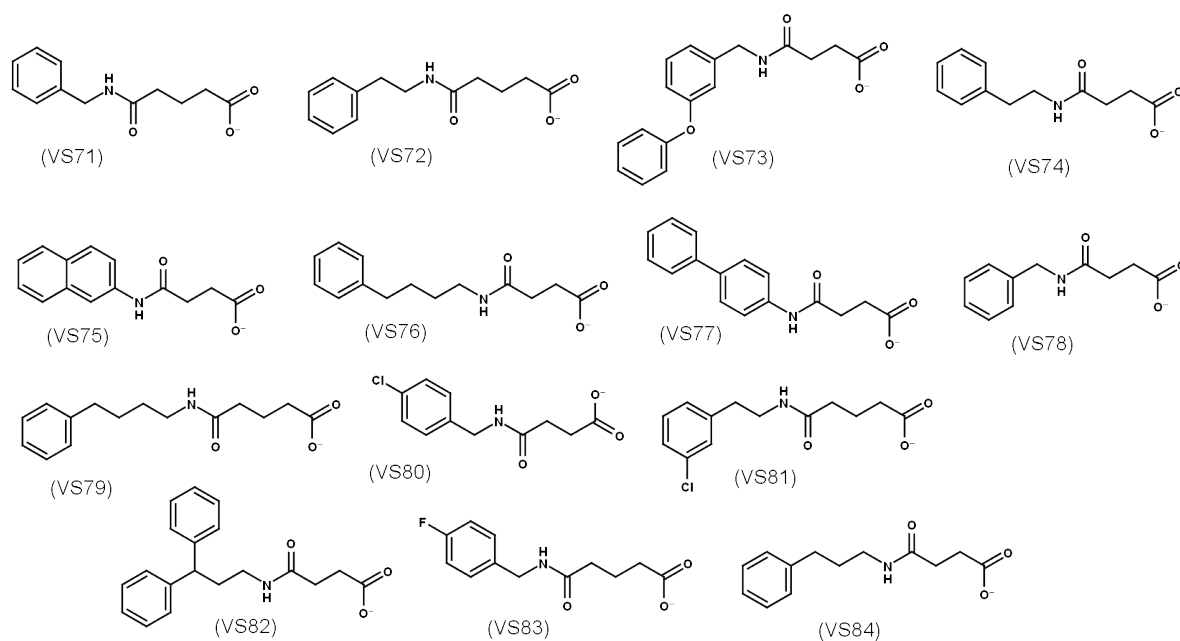
Figure B.13: Virtual screening candidates for Sirt5 inhibitors containing a succinyl or glutaryl group.

3D coordinates of all 778 hits were generated using MOE 2012.10[139] and each molecule was prepared for docking by adding partial charges, hydrogens and performing an energy minimizition according to the MMFF94 force field. Two different structures of Sirt5

---

*   *http://www.princetonbio.com*
†   *http://www.chembridge.com*
‡   *http://www.asinex.com*

were incorporated into subsequent docking runs: The first structure showed Arg105 in conformation *conf-1* (PDB: 3RIY, see Table B.1) and the second showed Arg105 in the alternative conformation *conf-2* (PDB: 3RIG).

All prepared ligand structures were docked to an ensemble of four Sirt5 models (3RIG and 3RIY, with and w/o and ADPR/NAD$^+$) using the docking program Gold 5.1[141]. The binding site was defined by the succinylated lysine residue as bound to the Michaelis-Menten complex (PDB: 3RIY). Hydrogen bond constraints were applied to the guanidine group of Arg105 to guide the docking process towards the desired salt bridge interaction. Each molecule was docked 15 times with default search efficiency and early termination, if the top three solutions were below a RMSD cutoff of 1.5 Å. Goldscore was used as objective function for the conformational search process and ASP for rescoring and pose refinement.

ID	Vendor	Vendor Code	Goldscore	ASP score
VS71	Princeton	OSSK528304	22.21	8.42
VS72	Chembridge	7283685	23.06	7.88
VS73	Asinex	BAS00546479	23.17	7.55
VS74	Chembridge	5329000	23.58	6.84
VS75	Chembridge	7268431	21.57	8.84
VS76	Princeton	OSSK642461	20.54	8.85
VS77	Princeton	OSSK344979	23.77	4.67
VS78	Chembridge	5222140	20.20	7.93
VS79	Princeton	OSSK528452	21.59	6.47
VS80	Chembridge	7234317	21.89	6.07
VS81	Asinex	BAS04395170	22.03	5.90
VS82	Chembridge	6097853	19.87	7.64
VS83	Princeton	OSSL304075	20.71	3.16
VS84	Chembridge	72350375	14.77	2.92

Table B.6: Virtual screening hits obtained from succinyl-lysine similarity screening. The docking scores were normalized by dividing the raw score by the number of heavy atoms to the power of 1/3.

The final Gold- and ASP-scores were normalized by dividing the raw score by the number of heavy atoms to the power of 1/3. All compounds were ranked according to their normalized scores and their sum-rank was calculated. The top 100 molecules according to their sum-rank were visually analyzed and about 50 solutions were refined by an energy minimization using the Amber12SB force field as implemented in MOE 2012.10[139]. 14 compounds were finally purchased from Princeton, Asinex and Chembridge (see Table B.6 and Figure B.13).

B.7.2 Carboxylic Acids and Sulfonamides Screening

Vendor catalogs of Chembridge[*], Chemdiv[†] and Enamine[‡] were extracted from the ZINC database[125] and converted to SMILES strings using the program *babel* from Openeye[150]. All three vendor catalogs were screened by a SMARTS pattern search for compounds containing either a sulfonamide[§] or a carboxylic acid group[¶]. In total, 106.817 molecules showed at least one of both features and were further filtered by the following physicochemical properties as calculated by MOE:

- Number of hydrogen bond donor/acceptor atoms lower than 10

- logP(o/w) coefficient between -1 and 6

- Number of rotatable bonds between 1 and 8

- Molecular weight between 150 and 550 dalton

- Topological surface area between 20 and 150 Å^2

61.382 compounds passed this filter and were subsequently prepared for docking experiments. Atomic charges as well as hydrogens were added and the conformation was optimized according to the MMFF94 force field as implemented in MOE 2012.10[139].

ID	Vendor	Vendor Code	Gold-Score	ASP Score	PLP Score	Chem-Score	Sirt5 Inhibition
SA1	Enamine	T5882807	21.76	12.30	24.48	10.57	IC$_{50}$: 68µM
SA2	Enamine	T6066496	22.09	8.79	18.96	7.96	IC$_{50}$: 100µM
SA3	Enamine	T6186645	25.17	12.60	24.93	12.15	n.i.
CA1	Chembridge	96631459	23.56	11.33	24.95	8.15	19% at 80 µM
CA2	Chembridge	7938972	19.83	9.14	21.97	7.28	14% at 80 µM
CA3	Chembridge	9060464	23.79	9.66	24.99	9.73	10% at 80 µM
CA4	Enamine	T52772246	23.05	10.00	24.74	6.82	n.s.
CA5	Enamine	Z166546684	28.45	15.18	28.54	12.42	n.i.
CA6	Enamine	Z95183012	23.86	11.47	26.31	11.41	n.i.

Table B.7: Virtual screening hits showing a carboxylic acid or sulfonamide function. The docking scores were normalized by dividing the raw score by the number of heavy atoms to the power of 1/3.

---

* *http://www.chembridge.com*

† *http://www.chemdiv.com*

‡ *http://www.enamine.net*

§   [$([#16X4]([NX3])(=[OX1])(=[OX1])[#6]),$([#16X4+2]([NX3])([OX1-])([OX1-])[#6])]

¶   ([CX3](=O)[O-]

All compounds were docked to an ensemble of Sirt5 structures using the docking program Gold 5.1[141]. The ensemble consisted of the substrate-bound conformation (PDB: 3RIY) an alternative structure (PDB: 3RIG) that shows a different conformation of Arg105 (PDB: 3RIG), the Suramin bound structure (PDB: 2NYR) and a fourth structure that shows a more open conformation (PDB: 2B4Y). All structures were prepared as described in Section B.1.

Gold was configured for 150% search efficiency and all four scoring functions (GoldScore, ASP, PLP, ChemScore) were used as objective function for the docking process. The binding site was defined by the succinylated lysine as natively bound at Sirt5 (PDB: 3RIY). Hydrogen bond constraints were applied to the guanidine group of Arg105, in order to guide the docking process towards the desired salt bridge interaction. Each molecule was docked 20 times and early termination was allowed, if the top three solutions were below a RMSD cutoff of 1.5 Å.
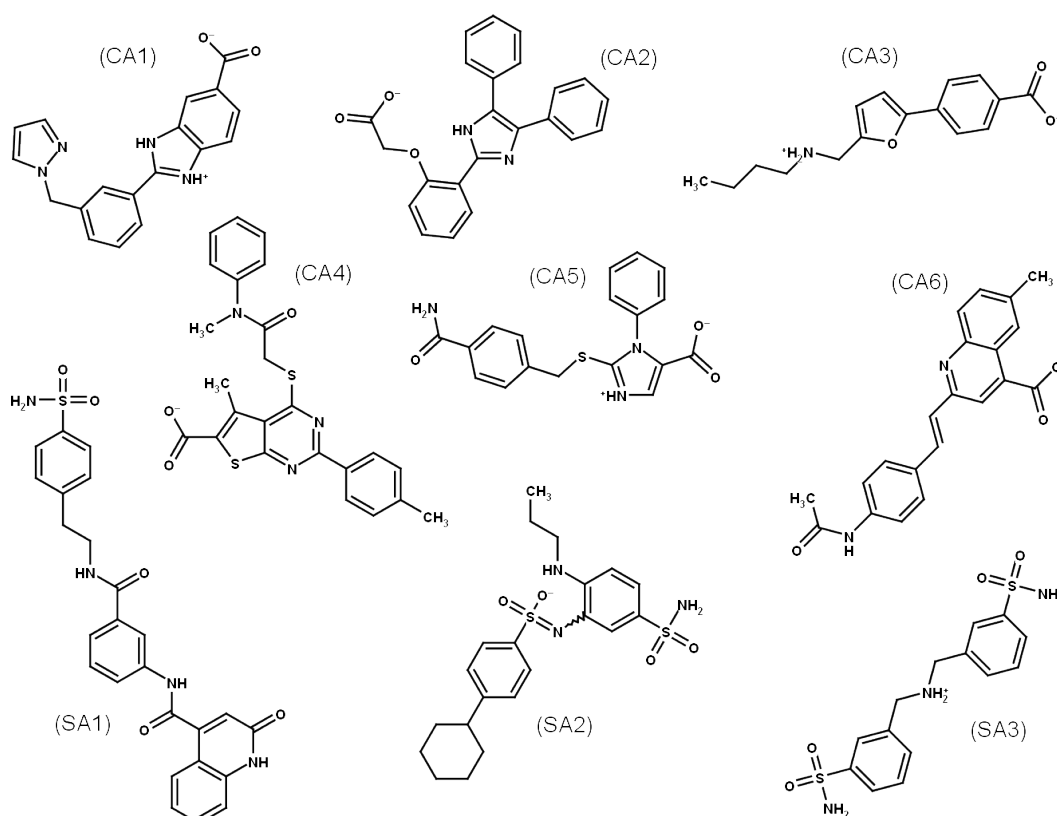
Figure B.14: Virtual screening candidates for Sirt5 inhibitors containing a carboxylic acid or sulfonamide group.

All scores were normalized by dividing the raw score by the number of heavy atoms to the power of 1/3. The compounds were ranked according to the four normalized scores (GoldScore, ASP, PLP, ChemScore) and 1.000 compounds showing the highest sum-rank were subjected to a diversity clustering using MOE. The MACCS-key Fingerprints were

calculated and the dataset was clustered using 85% intra- as well as 85% inter-cluster similarity. Compounds showing the highest sum-rank within a cluster were visually analyzed for their predicted binding mode. About 50 poses were refined by energy minimization according to the Amber12SB force field as implemented in MOE. Nine compounds were finally purchased from Chembridge and Enamine, in order to test their Sirt5 inhibition. All ordered compounds are shown in Figure B.14 and their data is listed in Table B.7.

B.7.3 Amidobenzamide Screening

The ZINC druglike database[125] was screened for molecules with a similar molecular fingerprint as the reference compound *AB1*. The Molprint2D package was used to perform the following calculations[152]. Molprint2D fingerprints were generated for all ZINC druglike molecules (1.932.058 molecules) and their Tanimoto similarity in respect to the query fingerprint was calculated. The 100 highest similar compounds were prepared for molecular docking by adding partial charges, hydrogens and optimizing their conformation according to the MMFF94 force field as implemented in MOE[139]. All compounds were docked to an ensemble of Sirt5 structures using the docking program Gold 5.1[141]. The ensemble consisted of the standard Sirt5 structure (PDB: 3RIY), the Suramin bound conformation of Sirt5 (PDB: 2NYR) and a third structure that shows a more open conformation (PDB: 2B4Y). All structures were prepared as described in Section B.1.
Gold was configured for maximum search efficiency and all four scoring functions (GoldScore, ASP, PLP, ChemScore) were used as objective function for the docking process. The binding site was defined by a sphere with a radius of 16 Å, centered nearby the catalytic His158. Each molecule was docked 20 times and early termination was allowed, if the top three solutions were below a RMSD cutoff of 1.5 Å.
The best scored pose from each scoring function was visually analyzed and promising docking solutions were refined by an energy minimization inside their corresponding model of Sirt5. 15 compounds were finally purchased, in order to test their inhibition of Sirt5. All ordered compounds are listed in Table B.8 and their structure is shown in Figure B.15.

ID	Vendor	Vendor Code	Tanimoto Similarity	Gold-Score	ASP Score	PLP Score	Chem-Score	Sirt5 Inhibition
AB1	Chembridge	7643968	1.00	25.61	13.66	26.76	13.24	IC$_{50}$: 36 µM
AB2	Chemdiv	K784-9261	0.57	25.07	13.90	24.88	10.73	IC$_{50}$: 41 µM
AB3	Enamine	7681967	0.68	27.32	13.92	25.41	12.65	IC$_{50}$: 48 µM
AB4	Chembridge	7647133	0.52	24.04	13.84	24.95	11.70	IC$_{50}$: 50 µM
AB5	Chembridge	7851912	0.48	22.81	14.07	24.11	12.74	IC$_{50}$: 75 µM
AB6	Chembridge	7972393	0.46	25.00	14.37	28.16	12.83	IC$_{50}$: 83 µM
AB7	Chembridge	7885180	0.50	23.22	13.34	25.32	12.57	IC$_{50}$: 88 µM
AB8	Chembridge	9132934	0.56	25.51	14.49	29.14	12.94	IC$_{50}$: 130 µM
AB9	Princeton	OSSK-917534	0.48	28.55	14.56	26.84	11.35	IC$_{50}$: 140 µM
AB10	Chembridge	7658321	0.68	25.56	14.52	26.02	11.59	24% at 82 µM
AB11	Chembridge	7658876	0.75	25.84	13.94	26.02	12.39	21% at 82 µM
AB12	Chembridge	9155779	0.56	22.87	14.47	25.69	12.77	n.i.
AB13	Chembridge	13338227	0.45	24.39	14.93	25.85	12.04	n.i.
AB14	Enamine	Z115060772	0.41	27.17	14.75	28.43	10.58	n.i.
AB15	Enamine	Z115060780	0.41	27.23	14.50	27.74	10.74	n.i.
AB16	Enamine	Z115060520	0.57	27.12	15.62	24.82	10.68	n.i.

Table B.8: Sirt5 inhibitor candidates resulted from amidobenzamide similarity screening. The docking scores were normalized by dividing the raw score by the number of heavy atoms to the power of 1/3. The tanimoto similarity was calculated for the Molprint2D fingerprints.
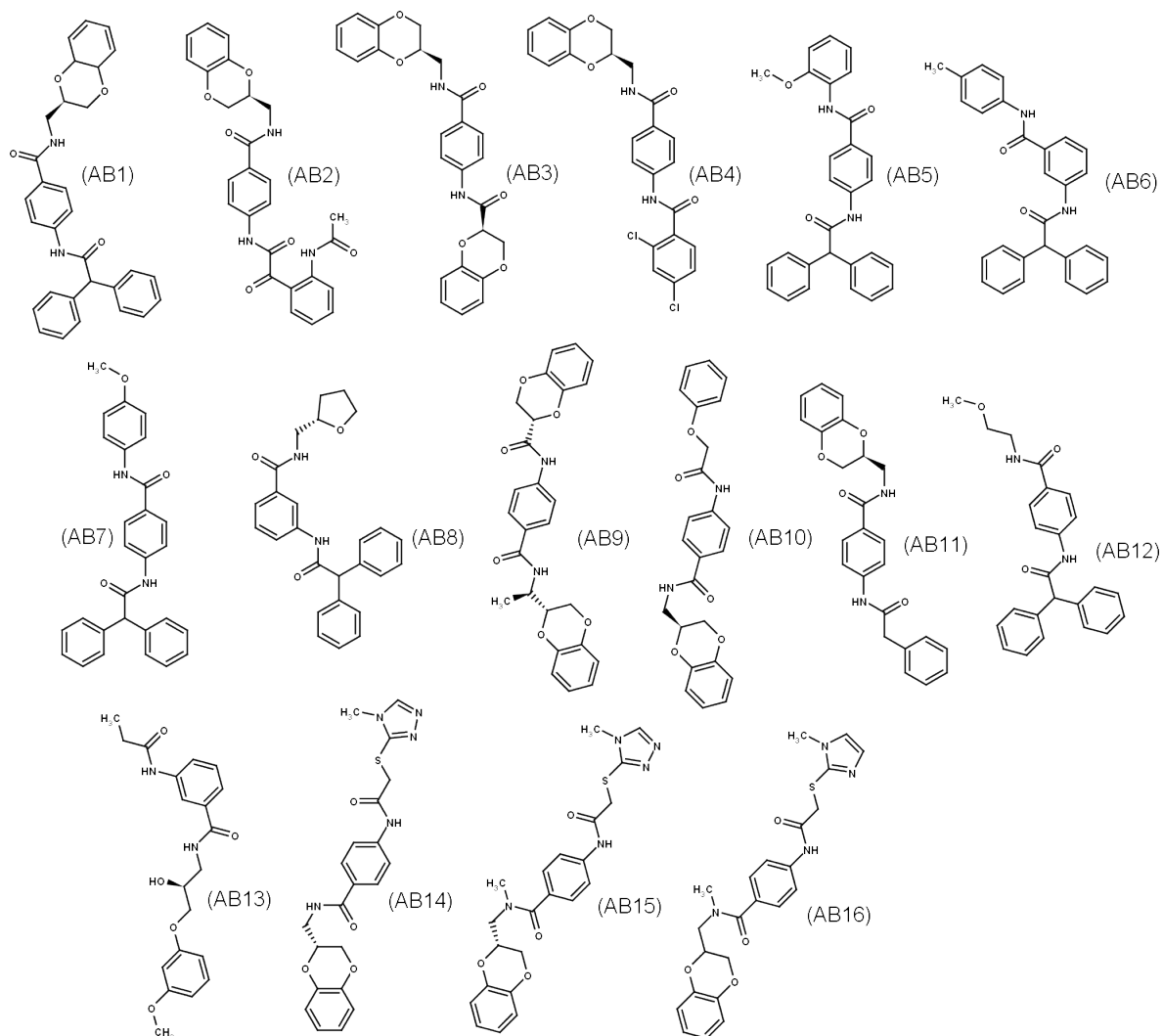
Figure B.15: Virtual screening candidates for Sirt5 inhibitors resulted from amidobenzamide screening.

APPENDIX C

Molecular Modeling Studies on Sirtuin 4

C.1 Crystal Structures

The structures listed in Table B.1 were downloaded from the PDB and prepared for the computational studies described in Section 4. Missing atoms were added, partial charges were calculated and the structure was protonated using standard methods and default settings of MOE 2012.10[139].

PDB Code	Protein	Bound Ligands	Resolution
2H59	Sir2-Tm	acetyl-ADPR, peptide	1.90 Å
4I5I	Sirt1	NAD^+ , EX-527	2.50 Å
3ZGV	Sirt2	ADPR	2.27 Å
3GLR	Sirt3	acetyl-Lys-peptide	1.80 Å
4JSR	Sirt3	ELT-11c	1.70 Å
4UTN	Sirt5	succinyl-Lys-peptide	3.00 Å
3RIY	Sirt5	NAD^+ , succinyl-Lys-peptide	1.55 Å
3ZG6	Sirt6	ADPR, myristol-Lys-peptide	2.20 Å

Table C.1: Selected crystal structures used for computational studies on Sirt4.

C.2 Homology Modeling Protocols

C.2.1 Template Detection

The sequence of Sirt4 was downloaded from Uniprot[153] and served as input for the web interfaces of *HHPred* and *I-Tasser*[131,133]. *HHPred* was configured by using three iterations of *HHBlits* for local sequence alignments and scoring secondary structures. *I-Tasser* was used with default settings and the latest snapshot of the PDB was selected for both homology searches. The standard web output was analyzed and the top five

template proteins scored from *I-Tasser* were compared with the top five template proteins scored by *HHPred* (see Table 4.1).

C.2.2 Multiple Sequence Alignment

Crystal structures of Sirt1, Sirt2, Sirt3, Sirt5 and Sirt6 were downloaded from the PDB (codes see Table C.1) and the sequences of Sirt4 (Q9Y6E7) and Sirt7 (Q9NRC8) were fetched from the Uniprot database. A sequence and structural alignment was carried out with MOE 2012.10[139] using all constraints listed in Table 4.2. The pairwise percentage identity is shown in Table C.2 and the alignment shown in Figure 4.1 was visualized with the program Jalview[144].

	Sirt1	*Sirt2*	*Sirt3*	*Sirt4*	*Sirt5*	*Sirt6*	*Sirt7*	*Sir2-Tm*
Sirt1		34.5	35.1	22.7	24.2	16.6	13.2	30.9
Sirt2	39.0		50.2	21.7	21.6	19.9	14.5	31.3
Sirt3	34.8	44.0		22.7	23.1	23.0	15.8	32.1
Sirt4	22.6	19.1	22.8		24.9	23.6	16.2	28.0
Sirt5	23.0	18.2	22.1	23.8		17.6	13.0	29.3
Sirt6	17.1	18.2	23.9	24.5	19.0		24.5	33.3
Sirt7	18.5	17.8	22.1	22.7	19.0	33.1		27.6
Sir2-Tm	26.5	23.7	27.7	24.1	26.4	27.7	17.0	

Table C.2: Pairwise percentage identity values for sequences of Sirt1-7 and Sir2-Tm obtained from the constrained alignment process. The values in each column represent the percentage of the chains residues which are paired with identical residues in the chains of each row in the final alignment[139].

C.2.3 Model Refinement and Simulation

Three sets of protein models were generated by an identical protocol using the homology software Modeller 9.11[136].

Set-I contained Sirt4 models based on the crystal structure of Sir2-TM (2H59).

Set-II contained Sirt4 models based on a Sirt5 crystal structure (3RIY).

Set-III was generated for validation purpose and consisted of Sirt5 models based on a structure of Sir2-Af (1M2G). This structure was found as best template by an identical procedure as described in section C.2.1

All template structures were downloaded from the PDB and superimposed using MOE 2012.10[139]. The co-crystallized ligands were removed, except NAD$^+$, which was used as rigid body constraint. The prepared structures, as well as the sequence alignments shown in Figure 4.1, were used as input for the subsequent modeling process.

Set	Model	Template	molpdf	DOPE	GA341
I	Sirt4	Sir2-TM	1736.9	-26441.4	1.00
II	Sirt4	Sirt5	1849.1	-26417.8	0.99
III	Sirt5	Sir2-Af	1746.9	-28399.5	1.00

Table C.3: Scores of models with best molpdf value for each set of homology models.

15 models were generated for each set of homology models, using the *automodel* parameter of Modeller and accurate MD refinement. All models were scored by the Modeller objective function (molpdf), DOPE and GA341 score (best scored models see Table C.3). The five models with the lowest molpdf score were selected from each subset and their quality was further assessed using Molprobity as well as the QMEAN scoring functions[137,138].

All models were submitted to the QMEAN server and scored using default settings. The model with the highest QMEAN Z-score was selected from each set models and uploaded to the Molprobity server. Hydrogens were added using the integrated tool *reduce* and all-atom contacts as well as geometric properties were analyzed for all selected models as well as their corresponding template structures. An overview on poor side chain rotamers, van-der-Waals clashes as well as Ramachandran outliers is shown in Table 4.3.

The Sirt4 model of *Set-II* showed a slightly better quality and was chosen fur further refinements. Unfavoured side chain conformations as well as atom-atom clashes proximal to the Sirtuin binding cleft were optimized using MOE 2012.10[139]. The modelled complex of Sirt4 and NAD^+ was simulated for 15 ns using Amber12[142] and an analog protocol as described in Section A.8.1. The stability of the simulation was proofed by the RMSD value of each snapshot in respect to the initial coordinates (see Figure C.1).
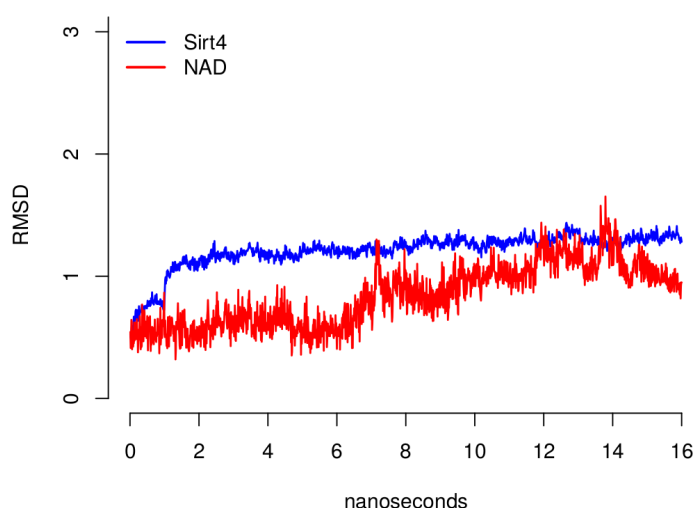

Figure C.1: RMSD of Sirt4 model and NAD^+ during a 15ns MD simulation. The RMSD values were calculated in respect to the initial coordinates.

C.2.4 Structural Comparison of Sirt4 Model and Template Structures

The Sirt4 protein model was superimposed with both template structures (PDB: 3RIY and 2H59) using MOE 2012.10[139]. The coordinates of productive bound NAD$^+$ were obtained from the rigid body constraint as defined for the homology modeling procedure (see Section C.2.3). The succinylated H3K9 peptide, as bound to Sirt5 (PDB: 3RIY), was used as template for an acetylated H3K9 peptide - the PTM of the corresponding lysine was manually modified.

C.2.5 Solvent Analysis

3D-RISM calculations were carried for the Sirt4-NAD$^+$ homology model, using Amber 12 and the same protocol as described in Section B.4.2. Water molecules were mapped into the highest likely water locations using the *Placevent* algorithm[122]. The solvated model of Sirt4 was superimposed to the solvated structure of Sirt5 and the position of the predicted waters were visually compared to the seven conserved waters described in Section 3.4. A water was defined as "confirmed", if a conserved water exist within a maximum radius of 1Å. The binding energies of six common waters were approximated by the radial distribution function obtained from 3D-RISM calculations using the same formula as described in Section B.4.2.

C.3 Docking of CPS1-based Peptides

The modelled complex of Sirt4 and NAD$^+$ was superimposed with a structure of zSirt5 in complex with *CP3* (PDB: 4UTN). The succinyl group of *CP3* was removed and the conformation was refined inside the substrate binding pocket of Sirt4. An energy minimizations of all peptide atoms as well as proximal Sirt4 residues was carried out using the Amber12 force field as implemented in MOE 2012.10[139]. The PTMs of *CP2*, *CP3*, *CP4*, *CP11* and *CP12* (see Section B.5.1) were added to the (unmodified) peptide lysine residue and all conformations were refined by a second energy minimization.
All five derivatives were subsequently docked to the Sirt4-NAD$^+$ model using Gold 5.1[141]. The binding pocket as well as a scaffold constraint was defined by the unmodified peptide residues as described above. Each derivative was docked 20 times using maximum search efficiency and Goldscore as objective function. All results which satisfied the desired scaffold constraint, were selected for a pose refinement by an energy minimization using the Amber12 force field as implemented in MOE. Only one (unique) solution was obtained for each peptide (see Figures 4.6, 4.7, 4.8 and 4.9).

C.4 Virtual Screening Protocol

The Princeton database (Express Stock 2012) was downloaded from the vendor website[*] and filtered for druglike molecules. A number of molecule descriptors were calculated using MOE 2012.10[139] and the following selection was done:

- $1 \leq$ hydrogen bond acceptors ≤ 10

- $0 \leq$ hydrogen bond donors ≤ 10

- $1 \leq$ rotatable bonds ≤ 10

- $-3 \leq$ logP (o/w) ≤ 8

- $15 \leq$ topological surface area ≤ 160

- $150 \leq$ molecular weight ≤ 600

About 470.000 molecules satisfied these criteria and were prepared for docking by adding partial charges and hydrogens and optimizing their conformation according to the MMFF94 force field. All compounds, the homology model of Sirt4 and water *W3* (see Section C.2.5) was used as input for a molecular docking with Gold 5.1[141]. Hydrogen bond constraints were applied to the backbone atoms of Val232, Asp236, Val145 and the side chain of Asp146. The binding pocket was defined by the superimposed inhibitor ELT-11c, as bound to a crystal structure of Sirt3 (PDB: 4JSR). Each molecule of the prefiltered Princeton database was docked 15 times to the here developed homology model if Sirt4. Gold was configured for a search efficiency of 100% and Goldscore was used as objective function. Early termination was allowed if the top three solutions were below a RMSD cutoff of 1.5Å.

The best Goldscores obtained for each molecule were normalized by dividing the raw score by the number of heavy atoms to the power of 1/3. The 10.000 best scored molecules were clustered according to their pairwise MACCS-key fingerprint similarity and poses of 200 cluster representatives were visually analyzed using MOE. About 80 poses were refined by energy minimization inside the binding pocket of Sirt4 and 43 compounds were finally purchased from Princeton in order to test their *in-vitro* activity. All ordered compounds are listed in Table C.4 and their structure is shown in Figure C.2.

---

[*] *http://www.princetonbio.com*

ID	Vendor Code	Goldscore	ID	Vendor Code	Goldscore
VS41	OSSL309945	25.59	VS63	OSSK706267	20.97
VS42	OSSL280987	25.07	VS64	OSSK280440	20.90
VS43	OSSK980849	24.70	VS65	OSSK671324	20.82
VS44	OSSK595686	24.15	VS66	OSSK393678	20.81
VS45	OSSK671780	23.97	VS67	OSSK713772	20.72
VS46	OSSL294309	23.46	VS68	OSSK444680	20.57
VS47	OSSK363499	23.40	VS69	OSSL117189	20.51
VS48	OSSK261563	23.35	VS70	OSSK360152	19.95
VS49	OSSK480394	23.07	VS71	OSSK715319	19.67
VS50	OSSK921921	22.59	VS72	OSSK539021	19.64
VS51	OSSL125753	22.52	VS73	OSSK776970	19.51
VS52	OSSL318655	22.41	VS74	OSSL105797	19.04
VS53	OSSK979070	22.32	VS75	OSSK285614	19.04
VS54	OSSL259882	22.18	VS76	OSSK342532	18.86
VS55	OSSL266012	21.95	VS77	OSSL117187	18.38
VS56	OSSK766798	21.93	VS78	OSSK571792	18.33
VS57	OSSK921836	21.91	VS79	OSSK804907	18.08
VS58	OSSK530294	21.80	VS80	OSSK537984	17.99
VS59	OSSK310299	21.71	VS81	OSSK766725	17.81
VS60	OSSK444962	21.49	VS82	OSSK544893	16.68
VS61	OSSK538452	21.24	VS83	OSSK337337	16.22
VS62	OSSK359892	21.18			

Table C.4: Virtual screening hits for Sirt4, which were ordered from Princeton. The Goldscores were normalized by dividing the raw score by the number of heavy atoms to the power of 1/3.
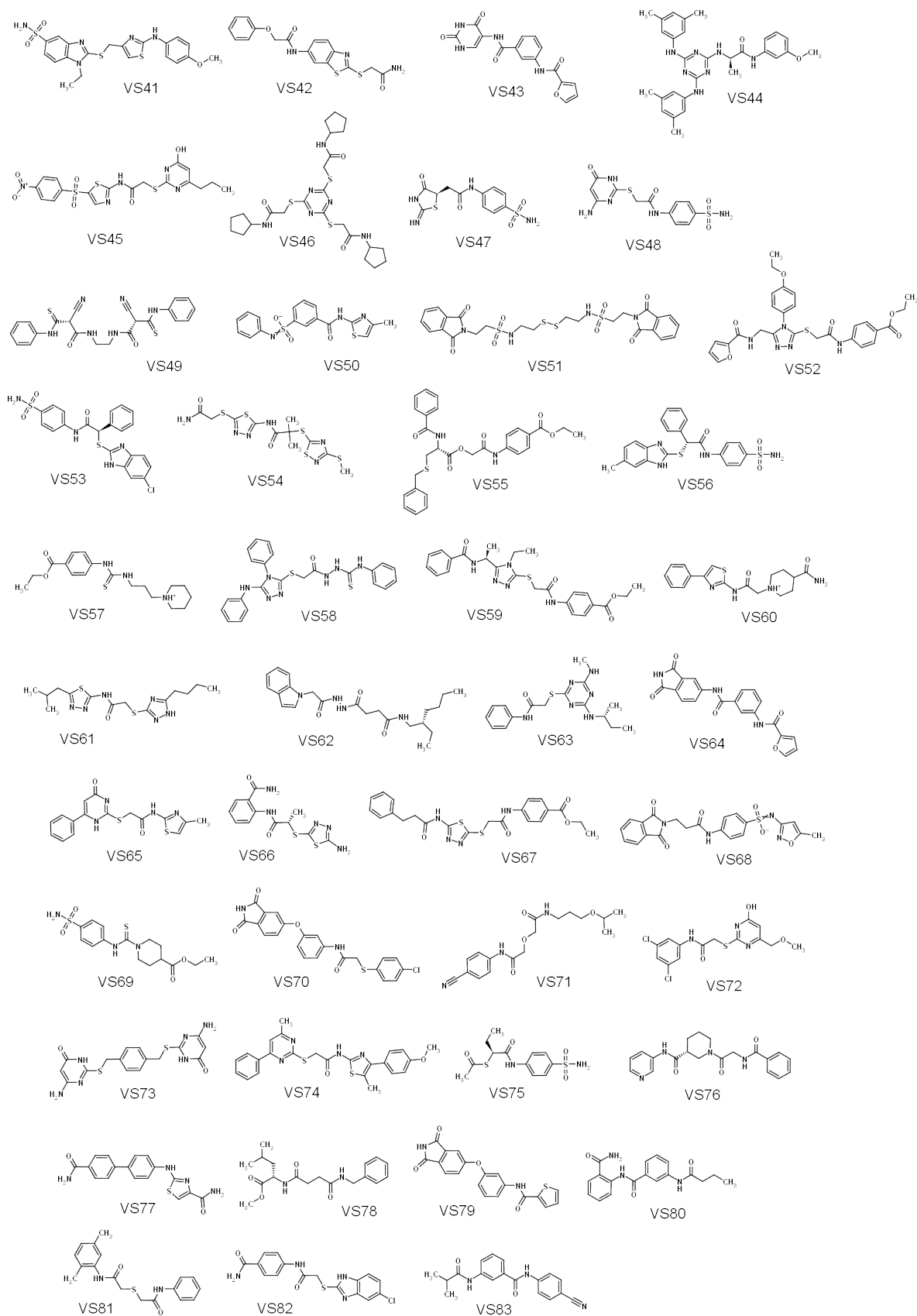
Figure C.2: Virtual screening hits for Sirt4, which were ordered from Princeton.

Curriculum Vitae

Personal Data

Name:	Michael Scharfe
Academic degree:	Bioinformatician (Diplom)
Gender:	male
Date of birth:	10th August 1981 in Halle (Saale)
Address:	Steghalden 14, 79539 Lörrach

Education

2010 - 2013	Ph.D. student
	Institute of Pharmacy, Martin-Luther-University Halle-Wittenberg
2002 - 2009	Diploma student in bioinformatics
	Institute of Computer Science, Martin-Luther-University Halle-Wittenberg
2001	Abitur, Johann-Gottfried Herder Gymnasium, Halle (Saale)

Research and Work Experience

2014 - present	Bioinformatics and data management
	Clinical Trial Unit, University Hospital Basel (CH)
2009-2013	Research associate
	Institute of Pharmacy, Martin-Luther-University Halle-Wittenberg
2008-2010	Research assistant
	Institute of Computer Science, Martin-Luther-University Halle-Wittenberg
2007-2010	Research assistant
	Leibniz Institute of Plant Genetics and Crop Plant Research, Gatersleben
2006-2008	Research assistant
	Institute of Psychology, Martin-Luther-University Halle-Wittenberg

Halle (Saale), den August 8, 2015   Michael Scharfe

List of Publications

(I) C. Roessler, T. Nowak, M. Pannek, M. Gertz, G. T.T. Nguyen, M. Scharfe, W. Sippl, C. Steegborn, M. Schutkowski: Chemical probing of the human Sirtuin 5 active site reveals its acyl specificity and peptide-based inhibitors. *Angew Chem Int Ed Engl. 2014 Aug 11. doi:10.1002/anie.201402679.*

(II) I. Slynko, M. Scharfe, T. Rumpf, M. Jung, W. Sippl: Combined approach for PRK1 virtual screening: from ensemble docking to rescoring using MM-PB(GB)SA binding free energy calculation and QSAR model development *J. Chem. Inf. Mod. 54 (1), 138-150, 2014.*

(III) F. Ntie-Kang, P. A. Onguene, M. Scharfe, L. C. Owono Owono, E. Megnassan, L. Meva Mbaze, W. Sippl and S. M. N. Efange: ConMedNP: a natural product library from Central African medicinal plants for drug discovery *RSC Adv., 2014, 4 (1), 409-419.*

(IV) F. Ntie-Kang, D. Zofou, S. B Babiaka, R. Meudom, M. Scharfe, L. L Lifongo, J. A Mbah, L. Meva Mbaze, W. Sippl, S. M. N. Efange: AfroDb: A Select Highly Potent and Diverse Natural Product Library from African Medicinal Plants *PlosOne, 2013:8(10):e78085*

(V) F. Ntie-Kang, J.A. Mbah, L.M. Mbaze, L.L. Lifongo, M. Scharfe, J.N. Hanna, F. Cho-Ngwa, P.A. Onguene, L.C. Owono, E. Megnassan, W. Sippl, S. M. Efange: CamMedNP: Building the Cameroonian 3D structural natural products database for virtual screening. *BMC Complement Altern Med. 2013 Apr 16;13:88.*

(VI) B. Maurer, T. Rumpf, M. Scharfe, J. Schemies, M. L. Schmitt, D. Stolfa, W. He, E. Verdin, W. Sippl, and M. Jung: Inhibitors of the NAD dependent protein desuccinylase and demalonylase Sirt5. *ACS Med. Chemistry Letters 3, 1050-1053, 2012*

(VII) U. Uciechowska, J. Schemies, M. Scharfe, M. Lawson, K. Wichapong, M. Jung, W. Sippl. Binding free energy calculations and biological testing of novel thiobarbiturates as inhibitors of the human NAD+ dependent histone deacetylase Sirt2 *Med. Chem. Comm. 3, 167-73, 2012*

List of Poster Presentations

(I) M. Scharfe, M. Pippel, B. Maurer, M. Jung, G. Wolber, W. Sippl: Structure-based virtual screening for Sirtuin-5 inhibitors. *Summer School of Drug Design, University of Vienna, 15.-20.09.2013, Vienna, Austria*

(II) M. Scharfe, M. Pippel, B. Maurer, M. Jung, G. Wolber, W. Sippl: Structure-based virtual screening for Sirtuin-5 inhibitors. *6th Joint Sheffield Conference on Cheminformatics, University of Sheffield, 22.-24.07.2013, Sheffield, UK*

(III) M. Scharfe, M. Pippel, R. Meier, W. Sippl: ParaDockS: Targeted Scoring Functions and Pharmacophore-basedConstraints for Molecular Docking. *International Workshop: New Approaches in Drug Design and Discovery, 19.-22.03.2012, Rauischholzhausen, Germany*

(IV) M. Scharfe, M. Pippel, R. Meier, W. Sippl: ParaDockS: Targeted Scoring Functions and Pharmacophore-based Constraints for Molecular Docking. *7th German Conference on Cheminformatics, 06.-08.11.2011, Goslar, Germany.*

(V) M. Scharfe, B. Maurer, K. Aktories, M. Jung, W. Sippl: Target-biased virtual screening for bacterial toxins. *25th Molecular Modeling Workshop, 04.-06.04.2011, Erlangen, Germany*

(VI) M. Scharfe, B. Maurer, K. Aktories, M. Jung, W. Sippl: Docking and virtual screening of novel inhibitors for mono-ADP-ribosylating toxins. *6th German Conference on Cheminformatics, 07.-09.11.2010, Goslar, Germany.*

(VII) M. Scharfe, B. Maurer, K. Aktories, M. Jung, W. Sippl: Docking and virtual screening of novel inhibitors for mono-ADP-ribosylating toxins. *5th Summer School Medicinal Chemistry, 13.-15. 09.2010, Regensburg, Germany.*

Erklärung der Selbstständigkeit

Hiermit erkläre ich, dass ich die vorliegende Arbeit selbständig und ohne fremde Hilfe verfasst habe. Ich habe keine anderen als die von mir angegebenen Quellen und Hilfsmittel benutzt. Die den benutzten Werken anderer Autoren wörtlich oder inhaltlich entnommenen Stellen sind als solche kenntlich gemacht. Ich versichere, dass ich mich bisher noch nicht um einen Doktorgrad beworben habe.

Halle (Saale), den August 8, 2015   Michael Scharfe